AN ABSTRACT OF THE THESIS OF

Qian Ye for the degree of Doctor of Philosophy in Atmospheric Sciences presented on August 20, 1993 .

Title: The Spatial-Scale Dependence of the Observed Anisotropy of Reflected and Emitted Radiation

Abstract Approved Redacted for Privacy

James A. Coakley, Jr.

The Earth Radiation Budget Experiment (ERBE) uses Angular Dependence Models (ADMs) to convert satellite observed radiances to radiative fluxes at the top of the atmosphere. Owing to errors in scene identification and to the relationship between the spatial scales of cloud systems and the spatial resolution of the ERBE scanner, the anisotropy of the radiation fields determined from ERBE observations was suspected of exhibiting a field of view size dependence. In order to remove effects due to the spatial scale of cloud fields, ERBE scanner observations from the Earth Radiation Budget Satellite (ERBS) were averaged to construct observations having a constant size field of view for all scan angles. Comparing the anisotropy for constant size fields of view with that obtained using unaltered full-resolution scanner observations, it was found that there were significant and systematic differences of the order of 5 – 10% for all scene types.

The frequencies of occurrence for clear, partly cloudy, mostly cloudy and overcast cloud categories identified by the ERBE scene identification algorithm were calculated for the constant size field of view observations. It was found that the ERBE scene identification method failed to correctly identify scene types. A bispectral threshold method was developed for scene identification. In the determination of the thresholds, the ERBE scene identification method was assumed to be correct for nadir observations. The thresholds were then determined so that the population of scene types remained constant from nadir to limb for the constant size field of view observations. ADMs were developed using the threshold scene identification method. Results showed that the spatial-scale dependence of the ADMs was significantly reduced. The threshold ADMs satisfied the principle of reciprocity more closely than did the ERBE ADMs for all cloud categories. Using the threshold scene identification, the view zenith angle dependence of the global average albedo and the longwave flux were significantly reduced compared with those obtained using the ERBE scene identification. The estimated global average albedo increases from 0.282 for the ERBE algorithm to 0.299 for the threshold algorithm. There was no significant change for the value of the estimated longwave flux.

The Spatial-Scale Dependence of the Observed Anisotropy of Reflected and Emitted Radiation

by

Qian Ye

A THESIS

submitted to

Oregon State University

in partial fulfillment of
the requirements for the
degree of

Doctor of Philosophy

Completed August 20, 1993

Commencement June, 1994

APPROVED:

Redacted for Privacy

Professor of Atmospheric Sciences in charge of major

Redacted for Privacy

Dean of College of Oceanic and Atmospheric Sciences

Redacted for Privacy

Dean of Graduate School

Date thesis is presented August 20, 1993

Typed by Qian Ye

ACKNOWLEDGMENTS

I am deeply indebted to my major professor, Dr. James A. Coakley, Jr., for his invaluable guidance and support over the course of my graduate study at OSU. He led me into the satellite remote sensing field and owing to his expert instruction, I have gradually come to understand the advanced theories of radiative transfer and cloud physics. He helped develop the topic for this thesis and gave much of his time and guidance throughout its production of the thesis. Without his dedication, encouragement and assistance, this research could never have been completed.

I would like to thank Professor Steven Esbensen for his interest, comments and suggestion during the writing of the thesis.

I would also like to thank the help and support from the other members of my doctoral committee, Dr. Jeffrey Barnes, Dr. Ted Strub and Dr. Mike Unsworth.

Thanks go to those faculty members and students of the College of Oceanic and Atmospheric Sciences at OSU for their help in various ways. Special thanks go to Professor Allan Murphy for the financial support during my first two years' study at OSU, to Phil Barbour for helping me read the thesis and reviewing my presentation, to Fu-Lung Chang for providing the plot routines, to Xijian Lin for providing the routines of the adding-doubling method, and to Gung Luo and Jielun Sun for their helpful comments.

Finally, I would like to thank my wife, Yuren Wei, for her love, patience and understanding during my graduate study at OSU. Thanks to my parents for their love, support and giving me their help whenever I needed.

This work was supported by NASA ERBE NAS1–18992.

TABLE OF CONTENTS

LIST OF FIGURES

LIST OF TABLES

THE SPATIAL-SCALE DEPENDENCE OF THE OBSERVED ANISOTROPY OF REFLECTED AND EMITTED RADIATION

1. INTRODUCTION

1.1 Background

The latitudinal distribution of incoming solar radiation and outgoing earth-emitted radiation drives the earth's atmospheric and oceanic circulation (Lorenz, 1967). Knowledge of the earth radiation budget is essential to understand climate and climate change (Barkstrom, 1984). Satellites orbiting at an altitude of several hundred kilometers above the earth's atmosphere have provided simultaneous measurements of the incoming solar radiation, the reflected solar radiation and the earth-emitted thermal radiation at the top of the atmosphere. Since the 1970's, knowledge of the energy budget and transports in the climate system has been greatly enhanced through these observations. Satellite observations have been applied to studies of climate (House et al., 1986; Hartmann et al., 1986), the validation of climate models (Raschke and Kondratyev, 1983; Stephens et al., 1981), the parameterization of radiation and cloud feedbacks (Cess et al., 1982; Raschke and Kondratyev, 1983; Cess et al., 1992), the determination of cloud properties (Coakley and Baldwin, 1984; Taylor and Stowe, 1984; Rossow, 1989; Hartmann et al., 1992), and the documentation of climate change (Carlson et al., 1981; Rossow et al., 1989).

The radiative flux at the top of the atmosphere (TOA), ***F***, gives the flow of energy between the earth and space. ***F*** is defined as the rate of the radiant energy propagating through a plane whose normal is in the radial direction from the earth's center. Two fundamentally different sensors aboard satellites have been employed to obtain TOA fluxes: wide field-of-view nonscanning instruments and narrow field-of-view scanning instruments (Fig. 1.1). The nonscanning wide field of view sensor measures the radiative flux at the satellite. By assuming that the area within the field of view is homogeneous, the measured fluxes can be converted to TOA fluxes through multiplying by the factor $(R/R_e)^2$, where R is the radius of the satellite's orbit and R_e is the radius to the top of the atmosphere. Because their spatial resolution is usually greater than (5400 km)^2 (Stephens et al., 1981), however, such measurements are not suitable for regional climate studies. For these types of studies measurements having higher spatial resolution are needed.

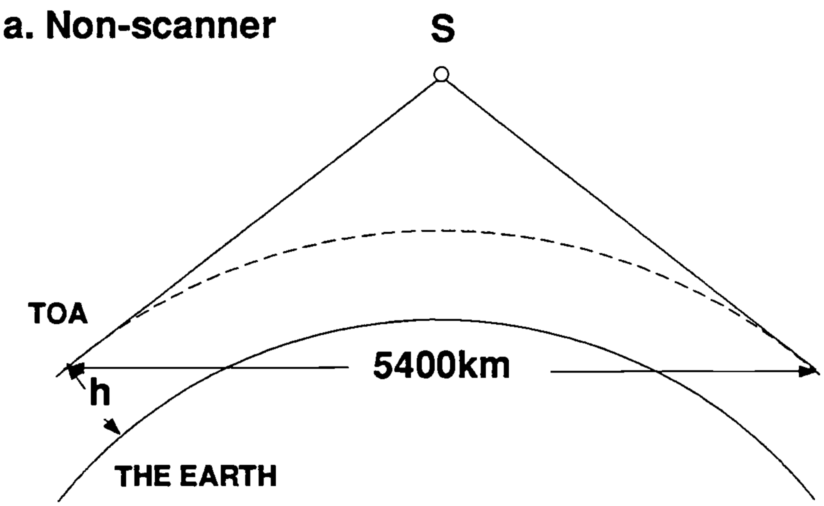
a. Non-scanner

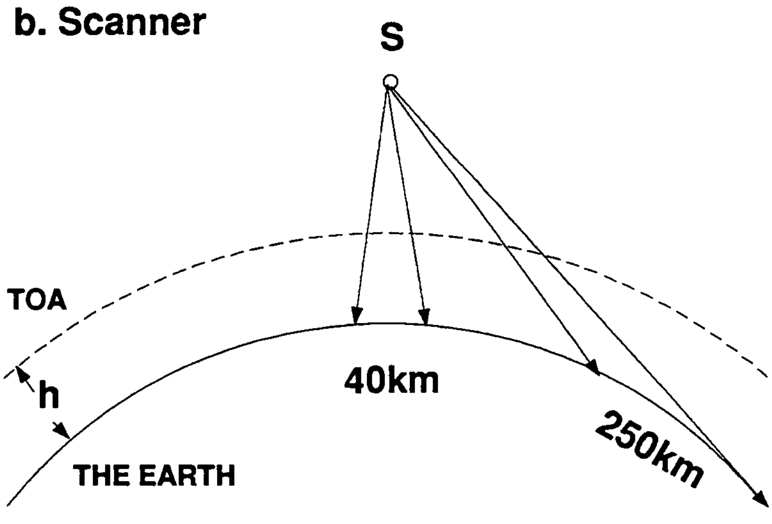
b. Scanner

Figure 1.1 Field of view for (a) nonscanner; (b) scanner.

Scanners make measurements at much higher spatial resolution. For example, the Nimbus-7 ERB scanners had a spatial resolution of about (90 km)^2 at nadir. This resolution was increased to about (40 km)^2 for the scanners aboard the Earth Radiation Budget Satellite (ERBS). Nevertheless, scanning radiometers only measure radiances which are the power per unit area per unit solid angle radiated at a particular angle to the normal direction of the TOA. Some means are needed to derive TOA fluxes from scanner radiances.

The radiance, ***I***, is defined as the radiative energy per unit time transported across a unit area in directions confined to a differential solid angle about the direction of propagation. As illustrated in Fig. 1.2, ***F***, the upward flux can be calculated by integrating the normal component of the radiance ***I*** over the entire hemispherical solid angle (Chandrasekhar, 1960):

$$\pi F(\mu_0) = \int_0^{2\pi} d\phi \int_0^1 d\mu \mu I(\mu_0, \mu, \phi) \tag{1.1}$$

where μ_0 is the cosine of the solar zenith angle θ_0, μ is the cosine of the view zenith angle θ, ϕ is the relative azimuth angle.

If satellites could measure radiances in all directions simultaneously for a given region, then the fluxes could be obtained directly from (1.1). In reality, however, satellites measure reflected and emitted radiances only at a few viewing angles for a particular geographic location at the time of observation. If the radiances were reflected or emitted isotropically, i.e., the radiances were independent of direction, then only one measurement would be needed and conversion to TOA fluxes would be straightforward. Surfaces which reflect radiation isotropically are called Lambertian surfaces. Unfortunately, there are no pure Lambertian surfaces on earth. Almost all natural surfaces reflect and emit radiation anisotropically. For reflected radiation, the fraction of the incident radiation reflected depends on the directions of both the incident and the reflected radiation. The degree of anisotropy depends on the physical properties of the reflecting or emitting surfaces. Fig. 1.3 shows a sketch of the angular distribution of reflected radiation. In the figure, most

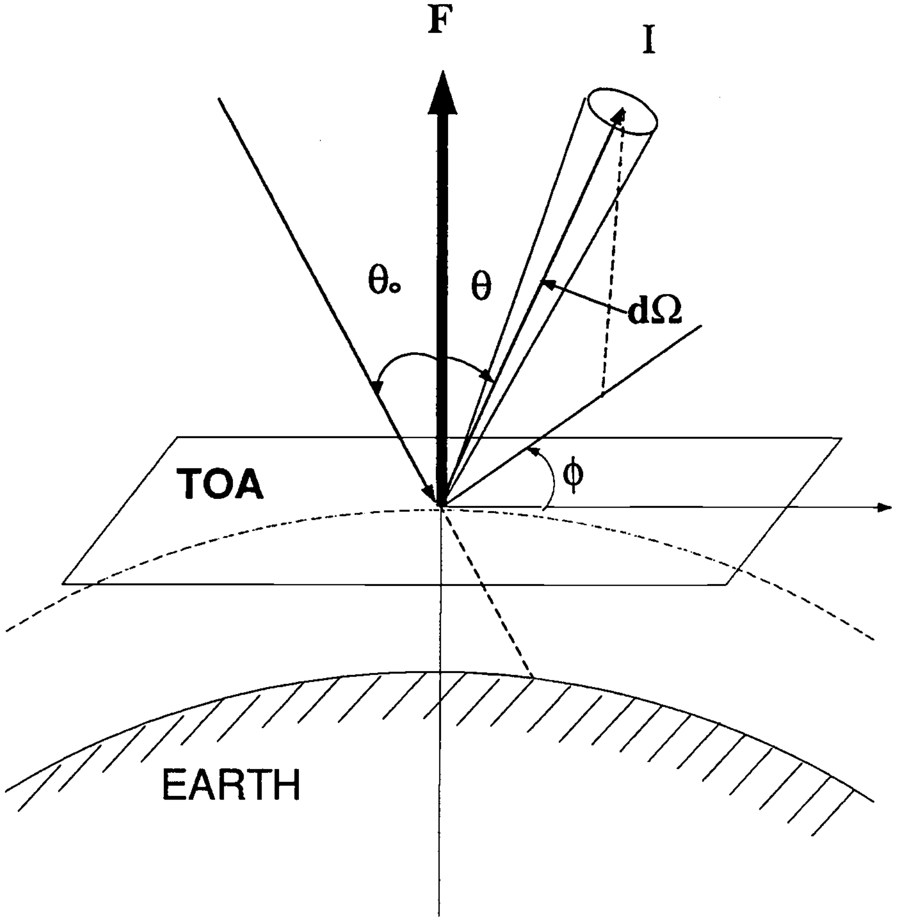

Figure 1.2 Radiative fluxes at the top of the atmosphere.

of the radiative energy is reflected in the forward and backward directions. Many authors have warned that a lack of knowledge of ADMs could lead to large errors in estimates of the earth's radiation budget components (Fritz et al., 1964; Coulson et al., 1966; Brennan and Bandeen, 1969; Eaton and Dirmhirn, 1979; Stowe et al., 1980; Davis and Cox, 1982). For example, Davis and Cox (1982) examined the angular dependence of the radiance fields reflected by 30 regional scale atmospheric scenes and concluded that neglecting the angular variation of the reflected radiances would lead to significant errors (10 – 100%) in the inferred fluxes at the top of the atmosphere. Baldwin and Coakley (1991) concluded that errors of up to 4% could be obtained for a typical 2.5° latitude-longitude, monthly mean if incorrect angular dependence models were applied in the conversion of observed radiances to radiative fluxes. For thermal radiation, large zenith angle dependences were also observed (Kondratyev, 1969; Naber and Weinman, 1984).

No theory describes the angular dependence of radiation fields for all surfaces. Numerical models have been used to simulate the angular distribution of the radiation for a limited number of surface types (Pinty and Verstraete, 1992). For more than forty years, a great deal of effort has been devoted to constructing empirical angular dependence models. These models are based on measurements collected by balloon, by aircraft, by satellite and in the laboratory. In the following section, a historical review is given of the angular dependence studies and the evolution of angular dependence models (ADMs).

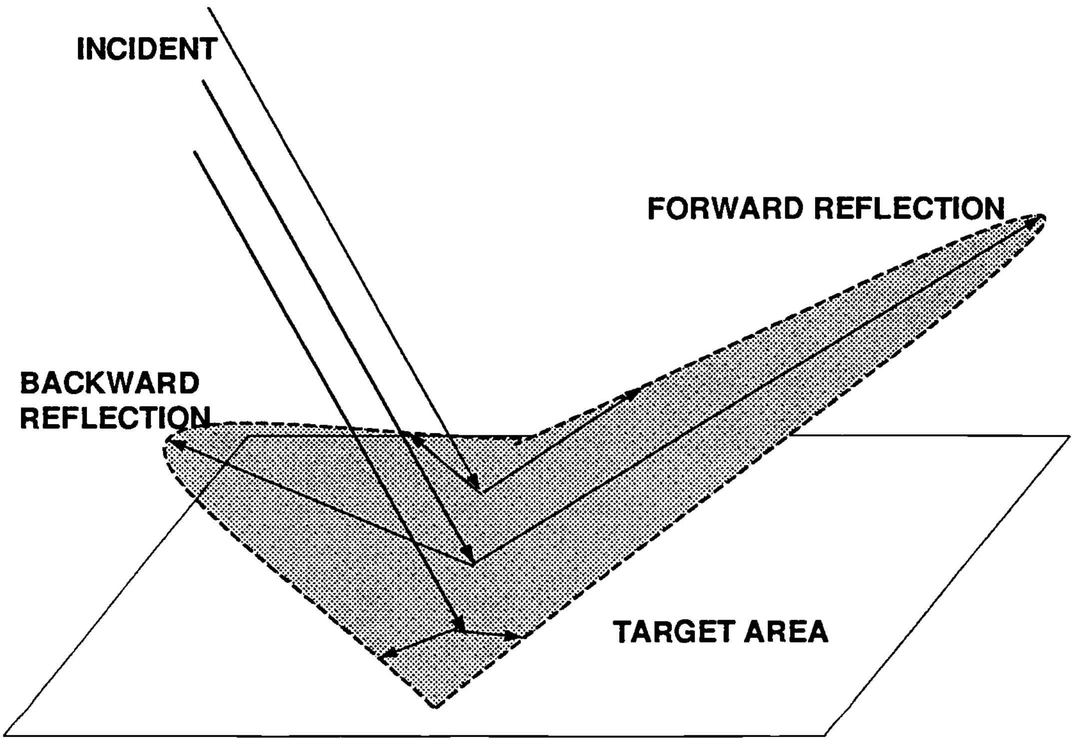

Figure 1.3 Angular distribution of reflected radiation.

1.2 Review Of Models For The Angular Distribution Of Radiation

The earth's surface consists of a variety constituents. Since these constituents have different degrees of heterogeneity, one should expect to observe distinct characteristics for the angular distribution of reflected and emitted radiation. In addition, the atmosphere is radiatively active so that the reflection and transmission of solar radiation and the emission of thermal radiation acquire strong angular dependences through interaction with the radiatively active components of the atmosphere. The angular dependence of the radiation depends on both the physical properties of the surface and the amount and composition of the atmosphere overlying the surface.

Bidirectional reflectivity functions (BDRFs) have been used to describe the angular distribution of reflected radiation. The BDRF is defined as the ratio of the reflected radiance at one particular angle to the reflected radiative flux. The BDRF is given by

$$BDRF(\mu_0,\mu,\phi) = \frac{\pi I(\mu_0,\mu,\phi)}{\pi F(\mu_0)} \quad . \tag{1.2}$$

The BDRF is often referred to as an angular dependence model (ADM).

Because it is fundamental in determining the surface energy balance and in specifying the lower boundary condition for remote sensing, the anisotropy of radiation reflected by the surface has been studied extensively in the fields of forestry, agriculture and environmental monitoring. Coulson et al. (1965) discussed studies of the effects of the angular variation of the reflectivity of snow and other natural land surfaces that have been conducted since the 1950's (for example, Ashburn and Weldon, 1956; Coulson, 1956). Coulson et al. (1965) described the dependence of reflectivities of several types of natural surfaces based on laboratory measurements in the shortwave domain. Their results showed that the intensity of the reflected radiation was generally anisotropic and depended on both the viewing geometry and physical characteristics of the surface.

Using an airborne radiometer, Kriebel (1978) measured the angular distribution of reflected radiation for both plowed fields and vegetated surfaces. He found that the reflection patterns were mainly determined by the geometric structure and shadow patterns of the surfaces.

Eaton and Dirmhirn (1979) measured angular patterns of reflected solar radiation for some of the most frequently encountered natural surfaces in the middle latitudes using the Nimbus Medium Resolution Radiometer located 3 m above the ground. They confirmed the effect of vertical structure on the angular distribution found by Kriebel (1978) and pointed out that, for mostly level surfaces, the reflection was strongest in the forward directions while reflection peaks in the backward direction mainly occurred over surfaces with extensive vertical structures.

Anisotropy has also been found in the angular distribution of longwave radiation fields. Becker et al. (1985) investigated the angular distribution of the radiation over various bare soils in the thermal infrared band (8 – 14 μm) by means of both theory and observations. They concluded that there were large variations in the angular distribution which depended strongly on both wavelength and the roughness and composition of the surface material.

The angular dependence of surface reflectivity is also a factor in the earth's radiation budget. For example, employing a plane-parallel atmospheric model with Rayleigh scattering, Coulson et al. (1966) examined the effects of the physical properties of a surface on the estimated planetary albedo. They found that there were significant changes in both intensity and degree of polarization at the top of the model atmosphere with changes in surface albedo. The effects of surface reflection would be more pronounced for optically thin atmospheres. Using the same approach, Fitch (1981) calculated the characteristics of the radiation emerging from an aerosol-ladened atmosphere overlying three different surfaces. The calculations indicated that the reflected and emitted radiances at the top of the atmosphere were significantly different for a realistic surface compared to those obtained for a Lambertian surface. Measurements of angular dependence patterns for many natural surfaces are underway (Meerkoetter, 1990).

In the atmosphere, clouds have strong interactions with radiation at both solar and thermal wavelengths. Clouds influence not only the fraction of solar radiation reflected or thermal radiation emitted but also the angular distribution of the reflected and emitted radiation. As will be discussed later, the angular distribution of the radiation fields is very sensitive to both the cloud physical and geometric characteristics. Unfortunately, clouds have high spatial and temporal variability. This variability makes the determination of cloud properties one of the most challenging problems in remote sensing. Constructing

ADMs from satellite observations is, therefore, much more complicated than doing so just above the surface. As noted below, any improvement in the determination of cloud properties could lead to significant improvements in the specification ADMs for the TOA fluxes.

Arking (1964) developed global average angular patterns for reflected radiances from TIROS IV observations. Using the observed angular distribution as correction factors in an analysis of TIROS VII observations, Arking and Levine (1967) obtained a value of 0.206 for an annual average albedo of the "quasi-globe" in which the polar regions beyond 60^0 and small areas of southern American and Siberia were excluded.

Ruff et al. (1968) used simple thresholds to identify the TIROS radiometer fields of view that were overcast by clouds. The spatial resolution of the TIROS radiometer was about $(70 \text{ km})^2$ at nadir. The reflection pattern associated with clouds were determined based on the TIROS IV visible channel (0.55 – 0.75 μm) observations. The anisotropic nature of radiation reflected by clouds was clearly shown in the very high values of the radiances reflected in the forward direction (the direction away from the sun).

In an attempt to verify the results obtained using satellite measurements, Brennan and Bandeen (1969) used an aircraft-borne medium resolution radiometer to measure the solar radiation reflected by clouds in wavebands, 0.2 – 0.4 μm and 0.55 – 0.85 μm. They concluded that the reflectivities for most of the earth's surfaces were strongly anisotropic and that the degree of anisotropy depended on surface type.

Raschke et al. (1970) made the first attempt to determine the earth's radiation budget allowing for the anisotropy of radiation. Their work considered radiation emanating from five scene types, i.e., clear-ocean, clear-land, cloudy-ocean, cloudy-land and snow.

Nimbus-7 ERB instruments were specifically designed to collect a large data base which covered the entire earth for an extended period of time. Using Nimbus-7 ERB observations, Taylor and Stowe (1984) constructed a set of angular reflectance models for eight uniform surface types: ocean, land, snow, ice and overcast clouds at four different altitudes. Cloud cover was determined based on analysis of data from the Nimbus-7

Temperature-Humidity Infrared Radiometer (THIR) combined with surface temperature maps. The Nimbus-7 ERB ADMs were used in the operational processing of converting broadband scanner data to broadband fluxes at the top of the atmosphere.

Further studies showed that cloud properties such as cloud cover (Coakley and Davies, 1986; Coakley and Kobayashi, 1989), cloud vertical extent (McKee and Cox, 1974; Davies, 1984; Kobayashi, 1993), cloud shape (Welch and Wielicki, 1986) and cloud particle size (Reynolds et al., 1978), have strong influences on the anisotropy of reflected and emitted radiation, and in turn, on the accuracy of the radiation budget components derived from satellite-based measurements. The Earth Radiation Budget Experiment (ERBE) developed a new set of ADMs for four levels of cloud fraction, namely clear (0% - 5% cloud cover), partly cloudy (5% - 50% cloud cover), mostly cloudy (50% - 95% cloud cover) and overcast (95% - 100% cloud cover). These cloud categories were combined with five surface types: ocean, land, desert, snow and coast (Suttles et al., 1988, 1989). The ERBE ADMs were derived from Nimbus-7 Earth Radiation Budget (ERB) scanner measurements. These ADMs represent the most comprehensive set of angular models currently being applied to obtain the earth's radiation budget. Wielicki and Green (1989) demonstrated that by applying the ERBE ADMs rather than relying on Lambertian assumptions, errors in the estimated flux could be reduced by more than a factor of 10 for particular scene types and viewing geometries.

1.3 Motivation

There are two key steps in the ERBE inversion algorithm for converting observed radiances to radiative fluxes: identifying the scene type and applying an appropriate angular dependence model for the particular scene. As was pointed out by Davies (1988) and later by Suttles et al. (1992), if the inversion process succeeds, then the estimated global average albedo and longwave flux obtained by averaging observations at a particular view zenith angle for the entire globe for a sufficiently long period of time

($\sim$ 3 months) should be independent of the view zenith angle used.

Validation studies of the inversion algorithm have been based on the evaluation of the estimated global average longwave fluxes and albedos (for example, Vemury et al., 1984; Smith and Manalo, 1988; Manalo et al., 1990, and Suttles et al., 1992). All of the validation studies, however, reported that the global average albedos and longwave fluxes derived from the ERBE inversion algorithm depended significantly on satellite view zenith angle. Fig. 1.4 shows an example of the global average albedo and emitted longwave flux. These results were based on Earth Radiation Budget Satellite (ERBS) scanning radiometer observations over oceans for September, October and November, 1986. The ERBS observations were identified by the ERBE maximum likelihood estimation (MLE) scene identification described by Wielicki and Green (1989). The reflected and emitted fluxes were converted from the ERBS observations using the ERBE ADMs described by Suttles et al. (1988, 1989). The resultant fluxes were averaged globally. The figure shows results for the spherical albedo. The spherical albedo is the average of the planetary albedo α weighted by the cosine of the solar zenith angle. It is given by

$$\alpha_s = \frac{\int_0^1 \alpha(\theta_0)\mu_0 d\mu_0}{\int_0^1 \mu_0 d\mu_0} . \tag{1.3}$$

The derived spherical albedo increases by about 8% from 0.268 at nadir to 0.291 at the limb. The longwave flux decreases by about 14.2% from 245.6 $\mathrm{Wm^{-2}}$ at nadir to 212.9 $\mathrm{Wm^{-2}}$ at the limb. Compared with the natural variability of the observations, the view zenith angle dependence is significant for both the derived albedos and longwave fluxes.

This view zenith angle dependence is probably caused by the scanner inversion algorithm. For example, in their analysis of Nimbus-7 ERB data, Vemury et al. (1984) found that there was an overestimation of the flux at large view zenith angle. They claimed that the error in the flux estimates was caused by the identification scheme used in the Nimbus-7 ERB which identified cloud scenes more frequently at large satellite zenith angle.

Suttles et al. (1992) applied the ERBE MLE scene identification method and the "New-Cloud ERB" (NCLE) algorithm described by Stowe et al. (1988) to Nimbus-7 ERB data. For both the estimated global average albedo and the longwave fluxes, the view zenith angle dependence was obvious. Since the NCLE method uses the higher

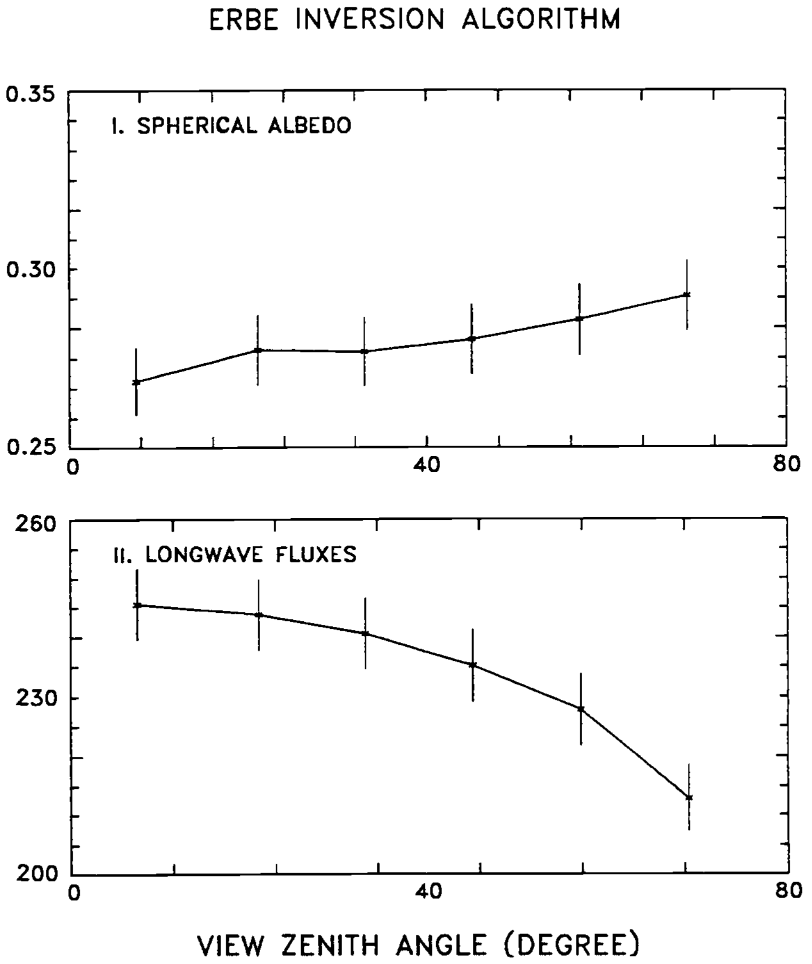

Figure 1.4 Satellite view zenith angle dependence of albedos (%) (upper diagram) and longwave fluxes (Wm^{-2}) (lower diagram). The results were derived using the ERBE inversion algorithm applied to ERBS scanner measurements over oceans for September, October and November, 1986. The vertical bars represent one standard deviation of the mean on each side of the curves.

spatial and spectral resolution Nimbus-7 Temperature and Humidity Infrared Radiometer (THIR) and Total Ozone Mapping Spectrometer (TOMS) data, it should provide better scene identification than that obtained with the ERBE MLE. Suttles et al. found that both scene identification methods gave similar fractional cloud cover which was nearly constant for view zenith angles less than 70°. Since the Nimbus-7 ERB scanner had an almost constant size field of view for view zenith angles less than 70° (Jacobowitz et al., 1984), they then claimed that the ERBE MLE scene identification did not depend on view zenith angle. Furthermore, they concluded that the ERBE angular dependence models were the primary cause of the view zenith angle dependence of the derived albedo and longwave fluxes. It should be pointed out that Suttles et al.'s conclusion was based on the MLE estimates of the fractional cloud cover. Recently, one of the authors, Wielicki, calculated the frequencies of occurrence for clear, partly cloudy, mostly cloudy and overcast scenes based on the Nimbus-7 ERB data (Wielicki, personal communication, 1993). His results revealed that the frequencies of occurrence for clear/overcast scenes decreased/increased with increasing view zenith angle. The frequencies of occurrence for partly and mostly cloudy scenes were almost constant from nadir to limb. Because the constant size field of view should have produced constant population of scene type, these results indicate that the ERBE MLE has zenith angle dependent scene identification errors and it incorrectly identifies cloud scenes for the Nimbus-7 ERB observations. Wielicki acknowledged that the view zenith dependence of the estimated global albedo and longwave flux was also due to the incorrect ERBE scene identification.

All previous studies suggested that, with perfect angular models, scene identification and satellite measurements one would obtain accurate fluxes. Because correct scene identification is required at both the development and application stages of the angular models, a lot of work has focused on the development and the validation of techniques for scene identification (Jacobowitz et al., 1984; Smith et al., 1986; Vemury, 1987; Gupta et al., 1988; Wielicki and Green, 1989; Suttles et al., 1992). Because of the large variation of cloud optical properties over relatively small spatial and temporal scales, obtaining correct scene identification based on coarse spatial resolution observations is impossible (Wielicki and Parker, 1992). The ERBE MLE uses coarse spatial resolution bispectral radiance pairs for scene identification. Consequently, ERBE observations are undoubtedly subject to scene identification errors.

The ERBE scene identification errors, however, are thought to vary systematically with view zenith angle. Systematic errors arise as follows. The scanner field of view size increases from nadir to limb. If clouds were uniformly distributed in space, then cloud scene types identified using scanner measurements would not be influenced by changes in field of view size with view zenith angle. Clouds, however, tend to cluster. Large regions (250 km)^2, about the size of the field of view at the limb for the ERBE scanner, are rarely cloud-free or overcast. They often have broken clouds. Small regions (40 km)^2, about the size of the scanner field of view at nadir, are either cloud-free or overcast approximately 15 – 20% of the time (Chang and Coakley, 1993). Consequently, most cloud-free or overcast observations from the scanning radiometer occur for the nadir views. Few appear at the limb. High resolution observations reveal that broken clouds constitute the majority of cloud scenes at spatial scales as small as 4 km. Because of the frequent occurrence of broken clouds, scenes near nadir that are identified as being cloud-free are often extracted from the midst of a broken cloudy system as illustrated in Fig. 1.5. These scenes have a high probability of being cloud contaminated. By comparison, scenes near the limb that are cloud-free, provided they are indeed cloud-free, are likely to be extracted from vast regions that are also cloud-free and consequently subject to less cloud contamination. Of course, the complimentary situation occurs for overcast scenes being contaminated by clear skies. As a result, the suspicion arises that the clustering of clouds and the inability to correctly identify scene types coupled with the growth of the scanner field of view size with satellite view zenith angle leads to a varying degree of cloud (or clear sky) contamination from nadir to limb. Because the anisotropy of reflected and emitted radiation is extremely sensitive to the degree of cloud cover, this varying degree of cloud (or clear sky) contamination affects the anisotropy of the observed radiances. Cloud-free regions with less cloud contamination should reflect and emit radiation that is more anisotropic than that which is contaminated.

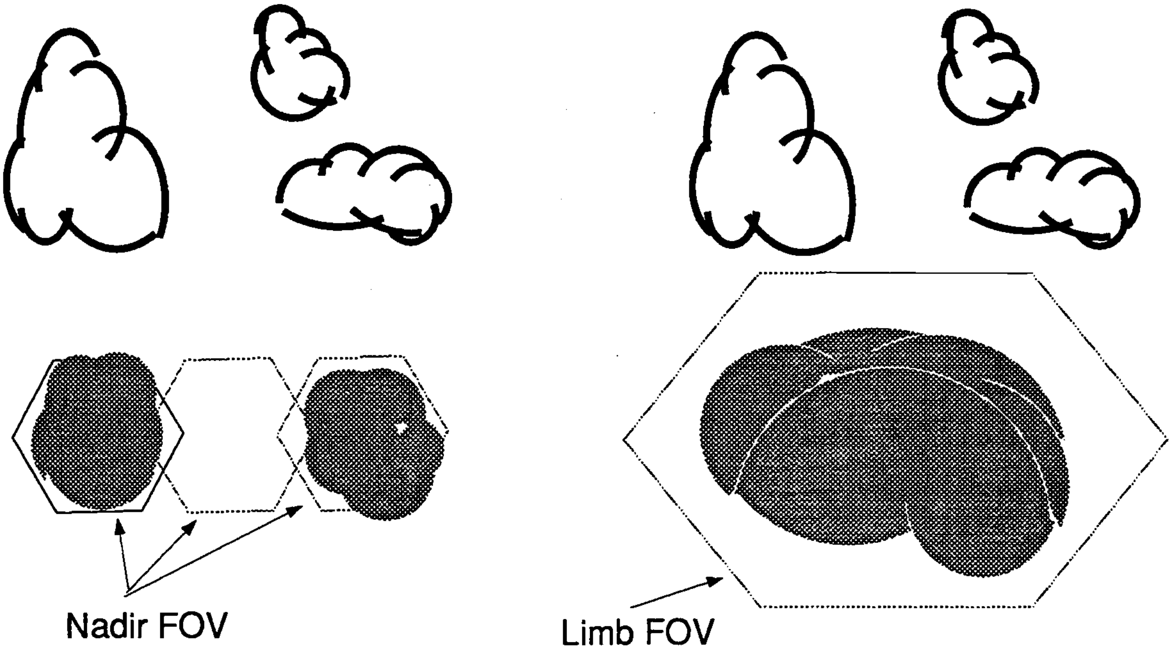

Figure 1.5 Cloud clustering and field of view size.

In the next chapter, a physical explanation is given for the angular distribution of radiation. Chandrasekhar's results for the angular distribution of isotropic and Rayleigh scattering will be presented. For a cloudy atmosphere bidirectional reflectivities will be obtained by solving the radiative transfer equation using the adding-doubling method (Coakley et al., 1983). Subsequently, in chapter 3, the ERBE inversion algorithm will be described along with a method for constructing ADMs.

For observations with constant size fields of view (CFOV), the degree of cloud contamination should be constant from nadir to limb. Hence, in chapter 4, a sensitivity test on the spatial-scale dependence of the ADMs will be conducted by comparing the anisotropy derived from the constant size field of view observations with that obtained from full resolution observations (FFOV). A procedure to construct constant size field of view observations is given in that chapter.

Because the CFOV observations indicate that view zenith angle dependent errors in scene identification were made by the ERBE MLE method, a threshold scene identification method is developed in chapter 5 in an attempt to obtain scene identification that is consistent for all view zenith angles. In the determination of the thresholds, the

ERBE MLE method is assumed to correctly identify scenes for nadir observations. The thresholds are determined so that the population of scene types remains constant from nadir to limb for the constant size field of view observations. ADMs are then constructed using the threshold scene identification method. The spatial-scale dependence of the observed anisotropy is again examined based on the threshold scene identification. The performance of the threshold ADMs is evaluated in chapter 6 in terms of the Helmholtz principle of reciprocity (Suttles et al., 1988), and the view zenith angle dependence of the global average albedo and emitted longwave flux. Summary and conclusions are given in chapter 7.

2. THE PHYSICS OF ANISOTROPIC REFLECTION AND EMISSION

2.1 Introduction

Almost all surfaces reflect and emit radiation anisotropically. The anisotropic characteristic of the radiances emanating from the earth-atmosphere system is the result of the interaction between electromagnetic waves and the constituents of the system: such as atmospheric molecules, aerosols, clouds, oceans, land surfaces, etc. The degree of anisotropy depends on the geometric dimensions and microphysical optical properties of the media (Cox, 1965; Brennan and Bandeen, 1969; Eaton and Dirmhirn, 1979; Davis and Cox, 1982). Since there is no theory for the radiative properties of realistic surfaces, a plane-parallel radiative transfer model will be used in this chapter to provide a qualitative explanation for the anisotropy of observed radiances.

There are three basic physical processes governing the transfer of radiation: absorption, emission, and scattering. When radiation propagates in a particular direction through a radiatively active medium, such as the atmosphere, the incident radiation is diminished by absorption which transforms radiative energy into other energy forms and by scattering which redistributes the incident radiation in all directions. Radiation is enhanced by emission and by scattering into the direction of propagation. For a plane-parallel absorbing and scattering atmosphere, the equation of radiative transfer for monochromatic radiation is given by

$$\begin{aligned}\mu\frac{dI_\nu(\tau,\mu,\phi)}{d\tau} = I_\nu(\tau,\mu,\phi) - \frac{1}{4\pi}\int_0^{2\pi} d\phi' \int_{-1}^{1} P(\mu,\mu',\phi')I_\nu(\tau,\mu',\phi')d\mu' \\ - \frac{1}{4\pi}\pi F_0 P(\mu_0,\mu,\phi)e^{-\frac{\tau}{\mu_0}}\end{aligned} \tag{2.1}$$

where μ is the cosine of the view zenith angle; ϕ is the relative azimuthal angle between the incident sunlight and the direction of propagation; τ is the optical depth which is taken to be zero at the top of the atmosphere; $P(\mu, \mu', \phi')$ is the phase function; πF_0 is the incident solar radiative flux at the top of the atmosphere, and $I_\nu(\tau, \mu, \phi)$ the radiance for monochromatic radiation for a wavenumber ν with units of watts per unit wave number per unit surface area per unit solid angle ($\mathrm{Wm^{-2}sr^{-1}cm}$).

Scattering processes redistribute the incident radiation in all directions and thus play a crucial role in determining the angular distribution of radiation fields as is shown in Fig. 2.1. Another factor which influences the angular distribution is the viewing geometry dependence of the optical path. This viewing geometry dependence is represented by the term $d\tau/\mu$ in (2.1). The degree of attenuation by the medium varies with viewing angle, and the resultant radiation is expected to be anisotropic.

Two fundamental scattering processes in the atmosphere are Rayleigh scattering and Mie scattering. They are distinguished based on the ratio of the radius of the scatterer to the wavelength of the incident radiation. Rayleigh scattering occurs when radiation interacts with atmospheric molecules. Molecules have radii that are much smaller than the wavelength of visible sunlight. Mie scattering, on the other hand, occurs when particle diameters are comparable to or larger than the wavelength of incident radiation. Cloud droplets and dust particles are Mie scatterers.

For surfaces, geometry is a crucial factor in determining the angular dependence of the emitted and reflected radiation. There are two extremes: specular reflectors (flat surfaces) which reflect into an angle equal to the angle of incidence, and Lambertian reflectors (rough surfaces) which reflect uniformly in all directions. Most earth surfaces are neither perfectly specular nor perfectly Lambertian (Eaton and Dirmhirn, 1979; Becker et al., 1985).

2.2 Anisotropy Of Scattering

Electromagnetic waves traversing a heterogeneous medium are scattered. In the atmosphere, the heterogeneities are caused by particles such as molecules, cloud droplets and aerosols. In optically dense media, such as oceans, scattering is caused by hydrosols and by small scale density fluctuations. The angular distribution of scattered radiation is described by the phase function P(Θ), where Θ is the scattering angle as shown in Fig. 2.1. The fraction of radiation scattered into solid angle $d\Omega$ (= $\sin\Theta d\Theta d\phi$) is given by $p(\Theta)\frac{d\Omega}{4\pi}$. The fraction of radiation lost at each scattering is given by (Chandrasekhar, 1960):

$$\frac{1}{4\pi}\int_{4\pi} p(\Theta)d\Omega = \tilde{\omega} \tag{2.2}$$

where $\tilde{\omega}$ is the single scattering albedo. It is the ratio of the scattered radiation to the incident radiation. In the case of conservative scattering, there is no absorption, $\tilde{\omega} = 1$.

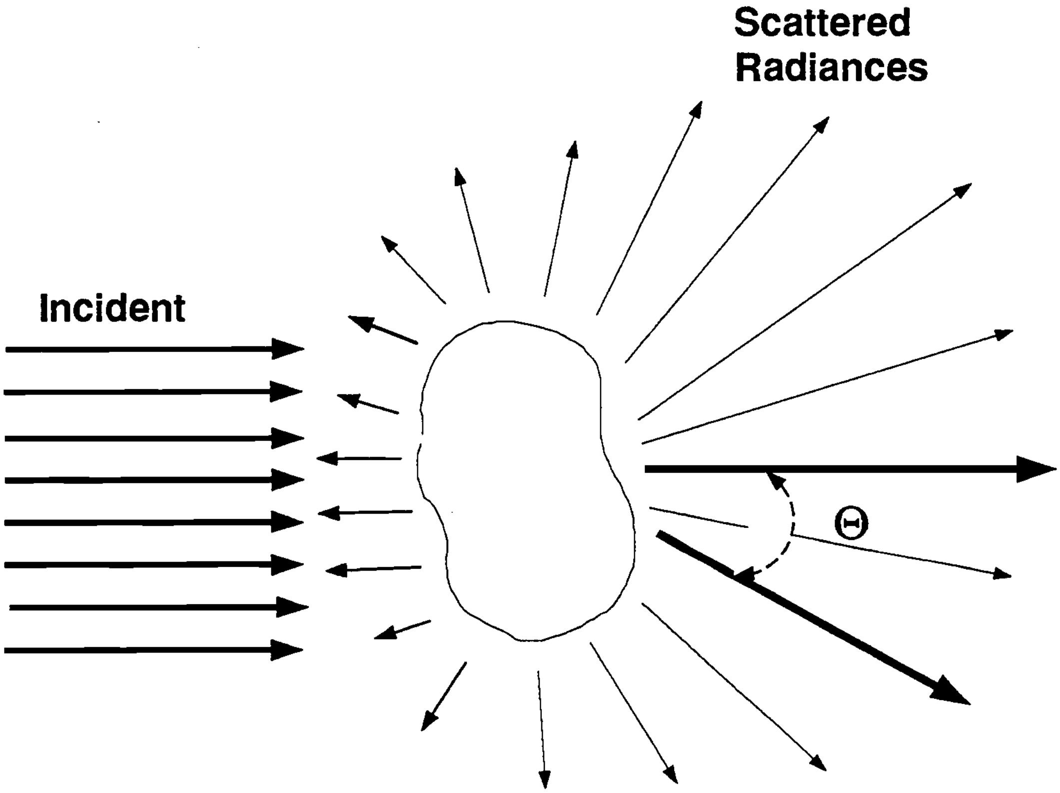

Figure 2.1 Scattering.

For a single particle with arbitrary size and shape, the intensity of scattered radiation is expected to vary with scattering direction. The physical reason for this variation has been conceptually illustrated by Bohren and Huffman (1983) as follows: Consider the particle which is made of many small parts (Fig. 2.2). In the electric field of the incident wave, a dipole moment will be induced in each part, and it will scatter secondary radiation with its intrinsic pattern. At a point P, the radiation scattered by the particle is obtained by superposing the scattered wavelets of all the dipoles. In different scattering directions, the phase relation between wavelets changes causing the intensities of scattered radiation to vary.

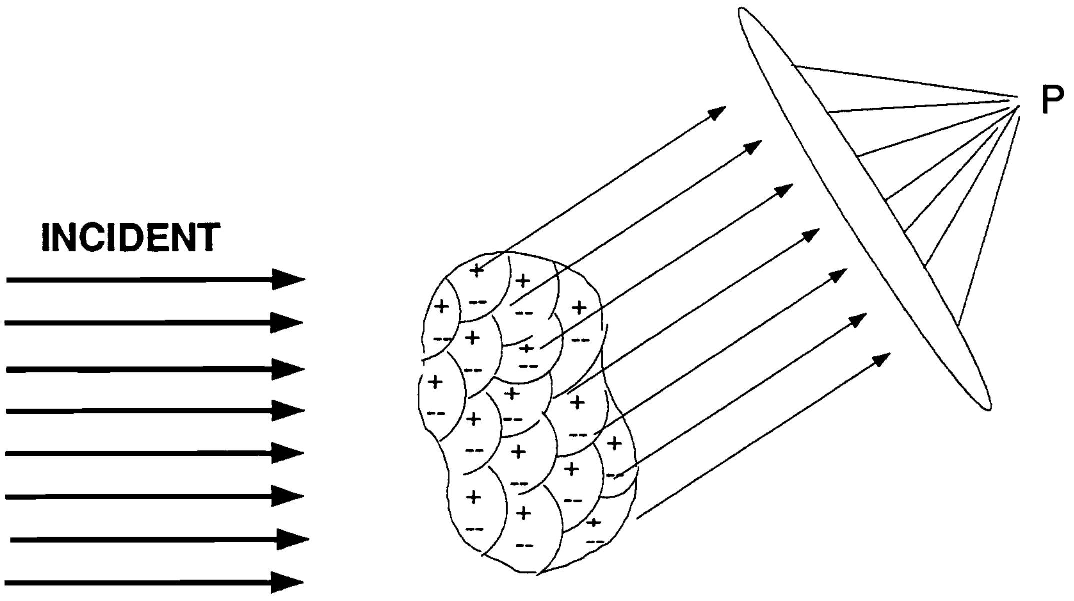

Figure 2.2 Conceptual illustration of scattering by a single particle.

Rayleigh scattering occurs for small particles. For a small homogeneous, isotropic spherical particle whose radius is much smaller than the wavelength of the incident radiation, the phase function for unpolarized light can be obtained by analytically solving the Maxwell electromagnetic wave equation. It is given by

$$P(\Theta) = \frac{3}{4}(1 + \cos^2 \Theta) \ . \tag{2.3}$$

Fig. 2.3 shows the angular distribution of the Rayleigh phase function. For unpolarized incident light, there are maxima in the forward (0°) and backward (180°) directions, and minima in the side directions (90° and 270°). It should be pointed out that the diagram only shows the light scattered in the principle plane which is the plane that includes both the directions of incident and scattered waves. A three-dimensional scattering pattern is obtained by rotating the diagram in Fig. 2.3 around the axis of 0° and 180°.

Rayleigh scattering exhibits the angular distribution of scattered radiation for molecular scattering. For scatterers having dimensions comparable to or larger than the wavelength of the radiation, as is often the case in the atmosphere at visible and infrared wavelengths, the maxima in the forward and backward directions and minima in both side directions remain. Fig. 2.4 shows the angular distribution of scattering by water droplets having radii of 0.5 μm, 1.0 μm, and 6.0 μm illuminated by visible light at a wavelength of 0.63 μm. The scattered radiances were calculated using Mie theory.

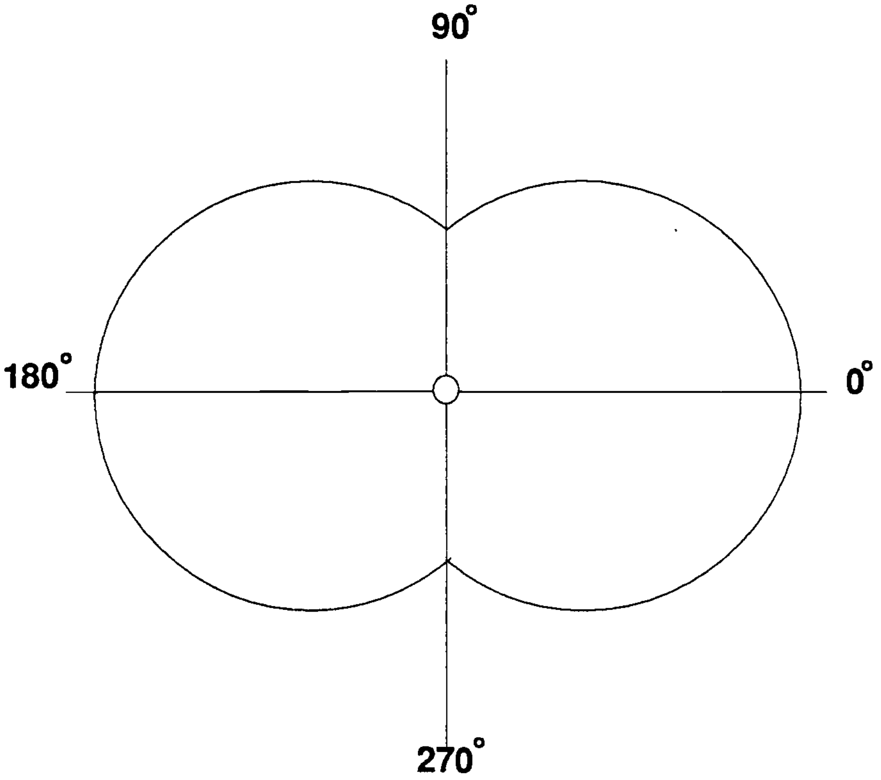

Figure 2.3 Rayleigh phase function for unpolarized light.

The figure shows the ratios of scattered radiances at scattering angles from 0° to 180° to the scattered radiance at scattering angle 0°. The ratio is plotted on a logarithmic scale. For a water droplet with a radius of 0.5 μm, the intensity of scattered radiation in the forward direction, i.e., scattering angle at 0°, is more than 100 times greater than that in the backward direction, i.e., scattering angle at 180°. There are minima at about 30° and 120°. With increasing droplet size, the directional asymmetry grows. For a 6.0 μm water droplet, which is typical of cloud droplets, the ratio of the scattered radiance at 0° to that at 180° is approximately four orders of magnitude. In this case, a relatively large portion of radiation is scattered through small scattering angles.

In the atmosphere, scattering usually involves a huge number of scatterers with a wide range of sizes ranging from atmospheric molecules to cloud droplets and ice crystals. Each particle is not only illuminated by the incident radiation but it is also exposed to radiation scattered by the other particles. Fig. 2.5 illustrates this situation. A particle at position S scatters the incident light just once, i.e. single scattering, in all directions. Meanwhile, a portion of the scattered light from particle S could be scattered again by nearby particles (particle T and U in this case) in all directions. This may be called secondary scattering. Likewise, a third-order, forth-order, ..., nth-order scattering could take place subsequently until the light escapes the medium at the top or the bottom. This process is called multiple scattering. For multiple scattering, the physical aspects of single particles on the anisotropy are greatly reduced. Different degrees of attenuation with viewing angle which are caused by the variation of optical pathlengths with view angle become a major source of the angular dependence of the radiation.

2.3 Angular Dependence Of Radiation That Has Suffered Multiple Scattering

2.3.1 Solutions For Isotropic And Rayleigh Scattering

Solutions to the radiative transfer equation are given for: 1) an atmosphere containing

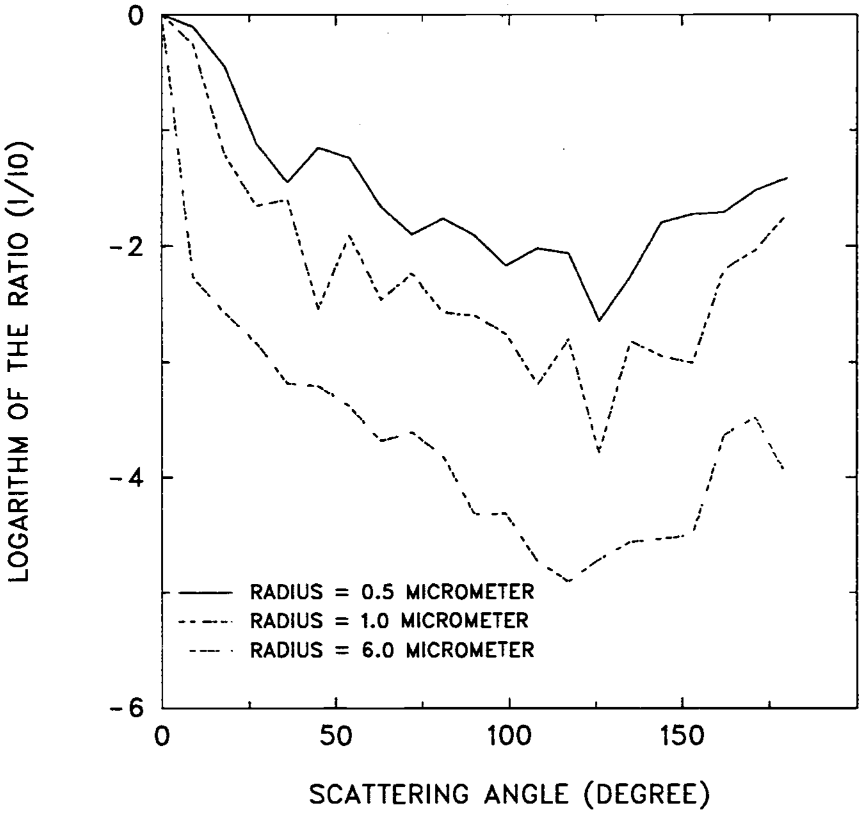

Figure 2.4 Scattered radiances as a function of scattering angle for water droplets with radii of 0.5 μm, 1.0 μm, 6.0 μm. The figure shows ratios of scattered radiances at scattering angles from 0° to 180° to the scattered radiance at scattering angle 0°.

isotropic scatterers, and 2) an atmosphere containing Rayleigh scatterers (Chandrasekhar, 1960).

The equation of radiative transfer (2.1) for isotropic scattering is given by

$$\mu\frac{dI(\tau,\mu,\phi)}{d\tau} = I(\tau,\mu,\phi) - \frac{\tilde{\omega}}{4\pi}\int_{0}^{2\pi} d\phi' \int_{-1}^{1} I(\tau,\mu',\phi')d\mu' - \frac{\tilde{\omega}}{4\pi}\pi F_0 e^{-\frac{\tau}{\mu_0}} . \tag{2.4}$$

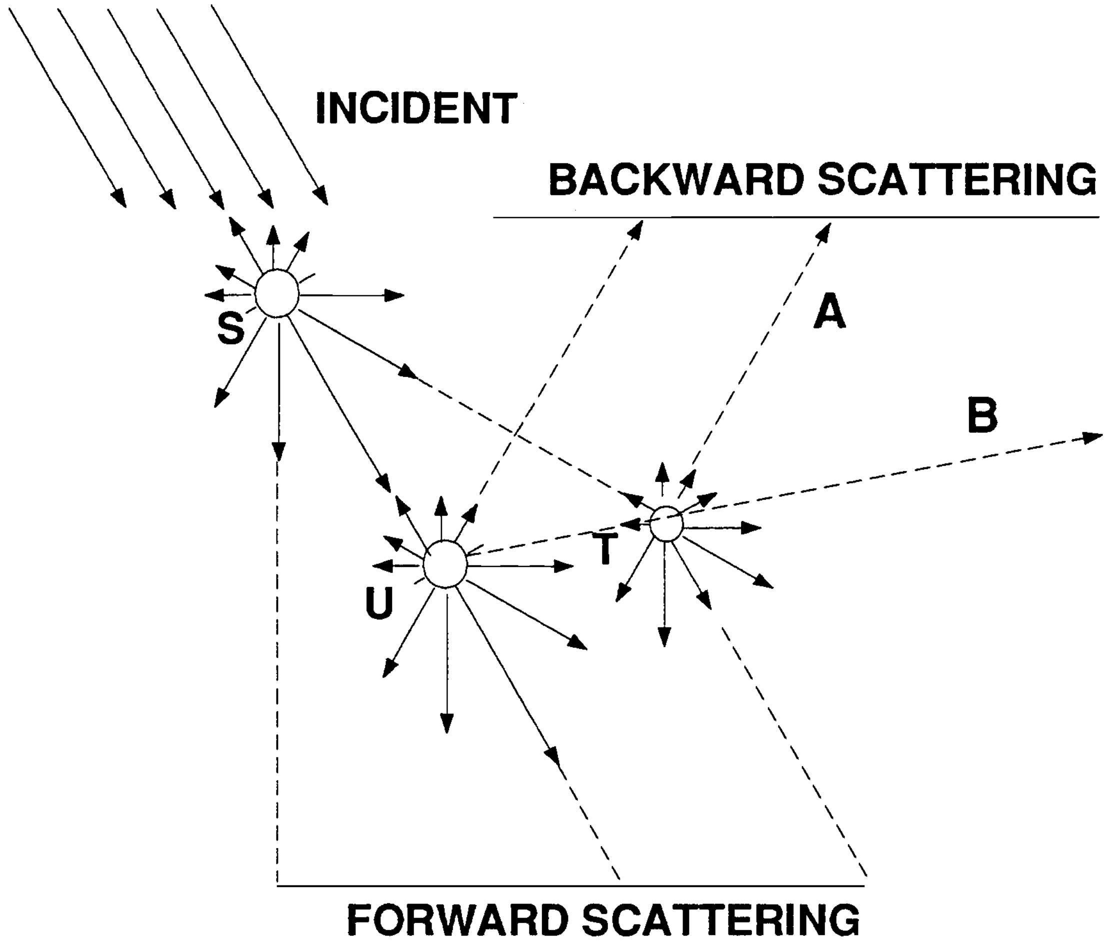

Figure 2.5 Multiple scattering.

The boundary conditions for diffusely scattered radiation are taken to be given by

$$\begin{aligned} I(0, -\mu, \phi) &= 0 \\ I(\tau_1, \mu, \phi) &= 0 \end{aligned} \tag{2.5}$$

where τ_1 is the optical depth of the atmosphere.

Reflected radiances at the top of the atmosphere, $I(0, \mu, \phi)$, are plotted in Fig. 2.6 for a semi-infinite atmosphere, i.e., $\tau_1 = \infty$. Radiances reflected by a Lambertian surface can be expressed in the form $I(0, \mu_0, \mu, \phi) = \alpha\mu_0 F_0$ (Chandrasekhar, 1960), where $\mu_0 F_0$ is the incident flux and α is the albedo. The figure illustrates the diffusely reflected radiances in units of $\mu_0 F_0$ for both single scattering and multiple scattering. Two cases with $\tilde{\omega} = 1.0$ (without absorption) and $\tilde{\omega} = 0.8$ (with absorption) are shown for solar zenith angle at 36.9° (μ_0 = 0.8). The patterns of the angular distribution of the diffuse reflection are different for singly and multiply scattered radiation. For conservative scattering, $\tilde{\omega} = 1$, the pattern changes from limb-brightening for single scattering to limb-darkening for multiple scattering. The darkening at large view zenith angles probably results from the large number of scatterers along the optical path for a given depth in the atmosphere. Photons have a small chance of passing by all scatterers before escaping to space. For single scattering, limb-brightening occurs because each scatterer scatters incident light only once in the direction of the viewer, and there are more scatterers at large view zenith angles for a given depth in the atmosphere that reflect radiation towards the viewer. Although there are no isotropic scatterers in the earth's atmosphere, the anisotropy observed for reflected sunlight shows tendencies that are similar to those shown in Fig. 2.6 with increasing cloudiness as will be discussed in chapter 3. For clear sky over oceans, where single scattering dominates, limb-brightening is observed. With increasing cloudiness, the degree of limb-brightening is reduced. Limb-darkening is observed for overcast scenes.

When absorption is added, the magnitude of the reflected radiances is reduced for single scattering, and it is reduced much more significantly for multiple scattering. Absorption diminishes radiation by transforming radiative energy to other forms of energy. Since absorption occurs with each scattering, a relatively large decrease in reflected radiation occurs for multiple scattering. It is interesting that when absorption takes place, the angular dependence of the reflected radiances changes. For single scattering, the degree of limb-brightening is reduced slightly. For multiple scattering, limb-brightening is obtained as opposed to the limb-darkening obtained in the conservative case. Limb-brightening arises because when absorption occurs, contributions to the reflected radiation by the high orders of scattering become negligible.

Fig. 2.7 presents Chandrasekhar's results for reflected radiances as a function of view zenith angle for ten different azimuthal angles with the solar zenith angle at 36.9°. In the figure, radiances are also in units of $\mu_0 F_0$. Calculations are made for Rayleigh scattering (solid lines) and isotropic scattering (dashed lines). In each diagram, there are three sets of curves. The top set of curves gives the reflected radiances for multiple scattering. The bottom set of curves gives the radiances for single scattering. The middle set of curves gives the differences between the top and bottom sets of curves. These curves represent the effect of the higher orders of scattering. Clearly, there are significant differences in the patterns of reflected radiances between multiple scattering and single scattering. Differences between Rayleigh and isotropic phase functions are negligible for the patterns of the contributions from orders of scattering higher than the first one. For Mie scattering, the asymmetric factor is not equal to that of isotropic scattering (g = 0.). Therefore, significant differences between Mie and isotropic scattering are expected for the higher orders of scattering.

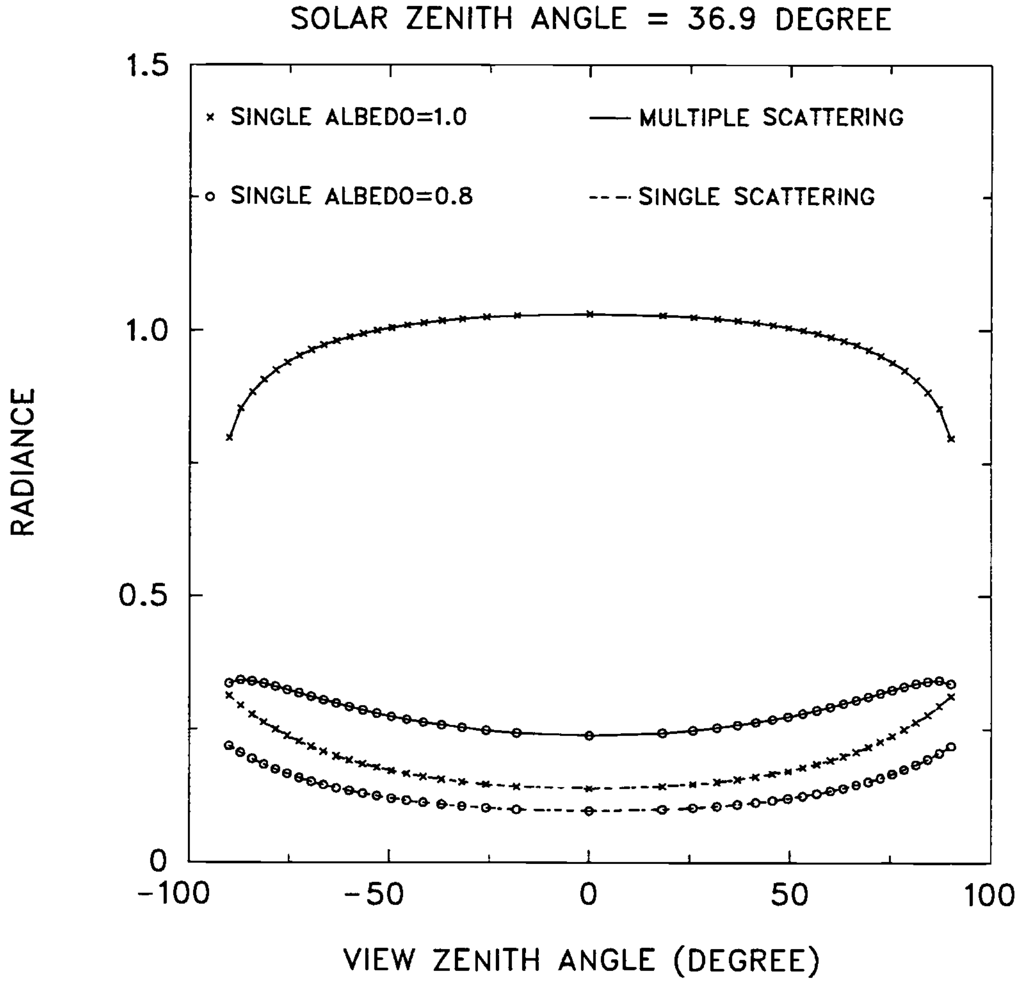

Figure 2.6 View zenith angle dependence of the reflected radiation for isotropic scattering at the top of a semi-infinite atmosphere, $\tau_1 = \infty$. In the figure, the radiances are plotted in units of $\mu_0 F_0$, where $\mu_0 F_0$ is the incident flux. Cases with $\tilde{\omega} = 1.0$ (conservative scattering) and $\tilde{\omega} = 0.8$ (with absorption) are illustrated for a solar zenith angle at 36.9° ($\mu_0 = 0.8$).

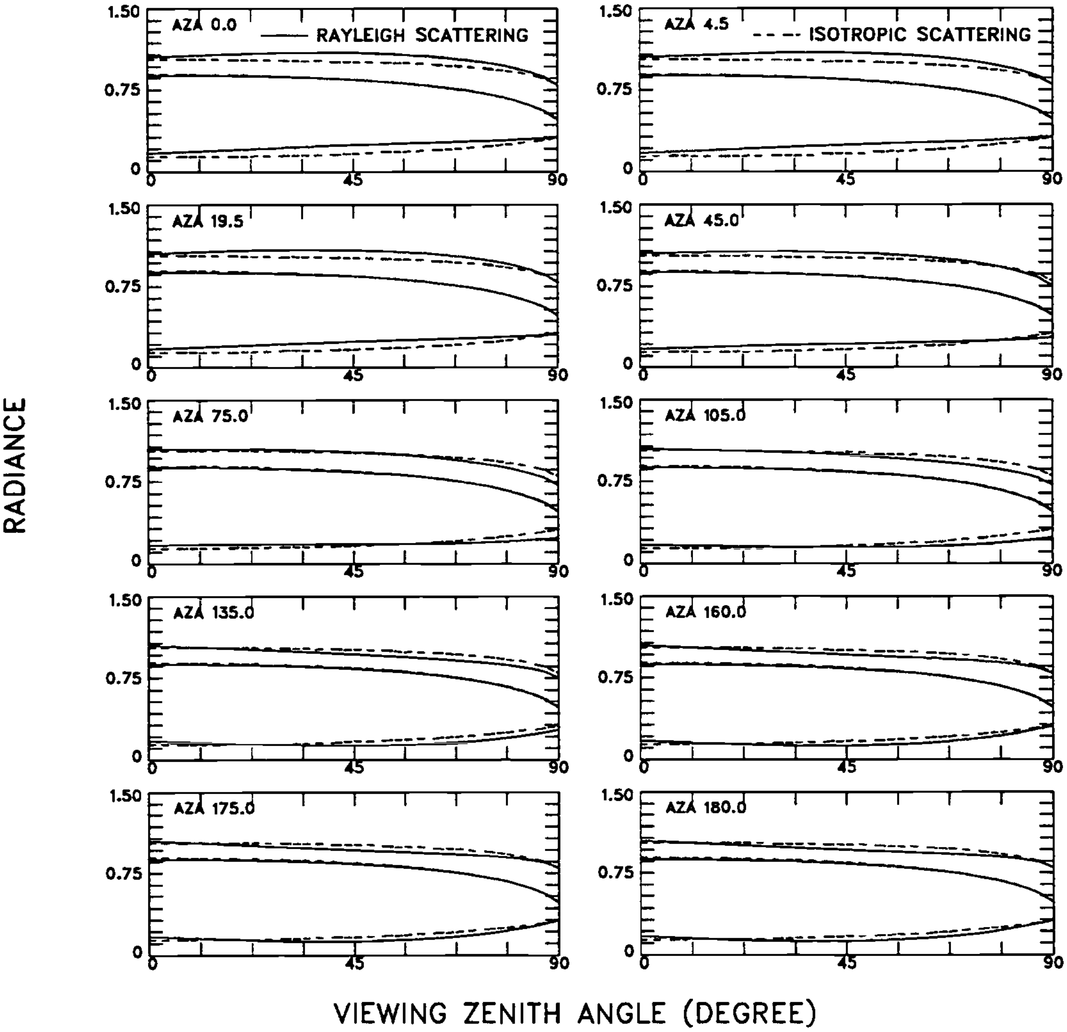

Figure 2.7 Reflected radiances for a semi-infinite atmosphere, $\tau_1 = \infty$. The radiances are plotted in units of $\mu_0 F_0$, where $\mu_0 F_0$ is the incident flux, for Rayleigh (solid lines) and isotropic (dashed lines) phase functions for ten azimuthal angles with the solar zenith angle at 36.9°. The top set of curves gives the reflected radiances due to multiple scattering. The bottom set of curves gives the reflected radiances which have suffered scattering only once. The middle set of curves gives the contribution of the higher orders of scattering. They are obtained by subtracting the results of single scattering from those of the corresponding multiple scattering.

2.3.2 Cloudy Atmospheres With Mie Phase Function

For more general phase functions, such as Mie phase functions, it is impossible to obtain solutions of the radiative transfer equation in the form of mathematical functions as is the case for isotropic and Rayleigh scattering. Furthermore, solutions using the Eddington approximation give the unphysical result that for conservative scattering, the anisotropy is independent of optical depth. Here, the radiative transfer equation (2.1) is solved using the adding-doubling method (Coakley et al., 1983) for a cloudy atmosphere with optical depth τ = 20 and τ = 0.75. The optical depth, τ = 20, is typical of a cloud with droplets having an equivalent radius (= 6 μm), a drop density = 300 drops/cm^3 and being 500 meter thick.

Cloud droplet sizes are usually comparable to or larger than the wavelength of solar radiation. Mie phase functions are needed to describe the angular distribution of scattered radiances in cloudy atmospheres. For numerical radiative transfer calculations, the Mie phase function is often approximated by the Henyey-Greenstein phase function (Goody and Young, 1989)

$$P_{HG}(\mu; g) = \frac{1 - g^2}{(1 + g^2 - 2g\mu)^{3/2}} \tag{2.6}$$

where μ is the cosine of the scattering angle and g is the asymmetry factor defined by

$$g = \frac{1}{2} \int_{-1}^{1} d\mu \mu P_{HG}(\mu) \ . \tag{2.7}$$

g > 0, if forward scattering dominates, g < 0, if backward scattering dominates, and g = 0 for isotropic and Rayleigh scattering.

Fig. 2.8 shows the results of the bidirectional reflectivity function (BDRF) in the principle plane for nonabsorbing ($\tilde{\omega} = 1.$) and absorbing ($\tilde{\omega} = 0.9$) cloudy atmospheres with a solar zenith angle of 36.8°. The asymmetry factor, g, is 0.82. For clouds without absorption, the BDRF is almost constant near nadir. Limb-darkening occurs at the limb. The limb-darkening is probably due to the increasing optical path length with view zenith angle. With larger optical path lengths, photons at a given depth in the cloud have a lower probability of escaping to space without suffering further scattering. With absorption, limb-brightening occurs. Clearly, with absorption, the BDRF is more anisotropic than that for the nonabsorbing case. The BDRF is smaller at nadir and larger at the limb than that for the nonabsorbing case. Because of absorption, contributions by the higher orders of scattering are negligible. Single scattering is a major contributor to the reflection and leads to large BDRF at forward scattering angles.

The lower diagram in the Fig. 2.8 shows the BDRFs for thin clouds, $\tau = 0.75$. Clearly, the effect of absorbing on the BDRF is small. For both absorbing and nonabsorbing cases, the degree of anisotropy is obviously larger than that for thick clouds. For thin clouds, single scattering dominates.

The dependence of the BDRF on the solar zenith angle is shown in Fig. 2.9 for the nonabsorbing cloudy atmosphere with optical depth $\tau = 20$. The curves shown are for solar zenith angles, 36.8°, 56.8°, 74.3° and 86.2°. Clearly, with increasing solar zenith angle, the values of the BDRFs increase at the limb but decrease at nadir. That means the degree of anisotropy increases.

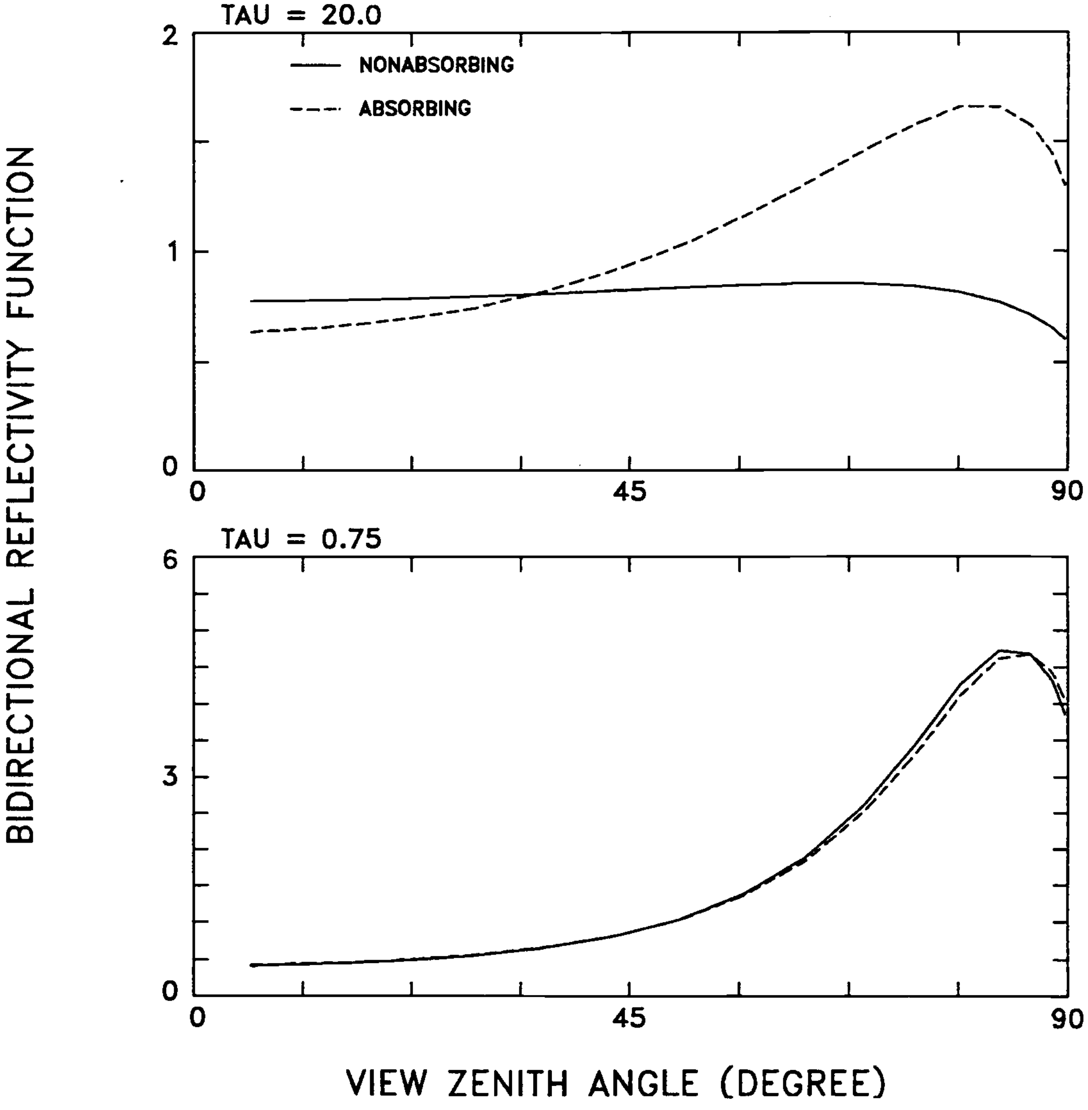

Figure 2.8 The bidirectional reflectivity functions (BDRFs) in the principle plane, ϕ = 0°, obtained using the adding-doubling method for a cloudy atmosphere. The upper diagram shows the BDRF for nonabsorbing (solid line) and absorbing (dashed line) atmosphere for $\tau_1 = 20.0$ at a solar zenith angle, $\theta_0 = 36.8°$. The lower diagram shows the same but for $\tau_1 = 0.75$.

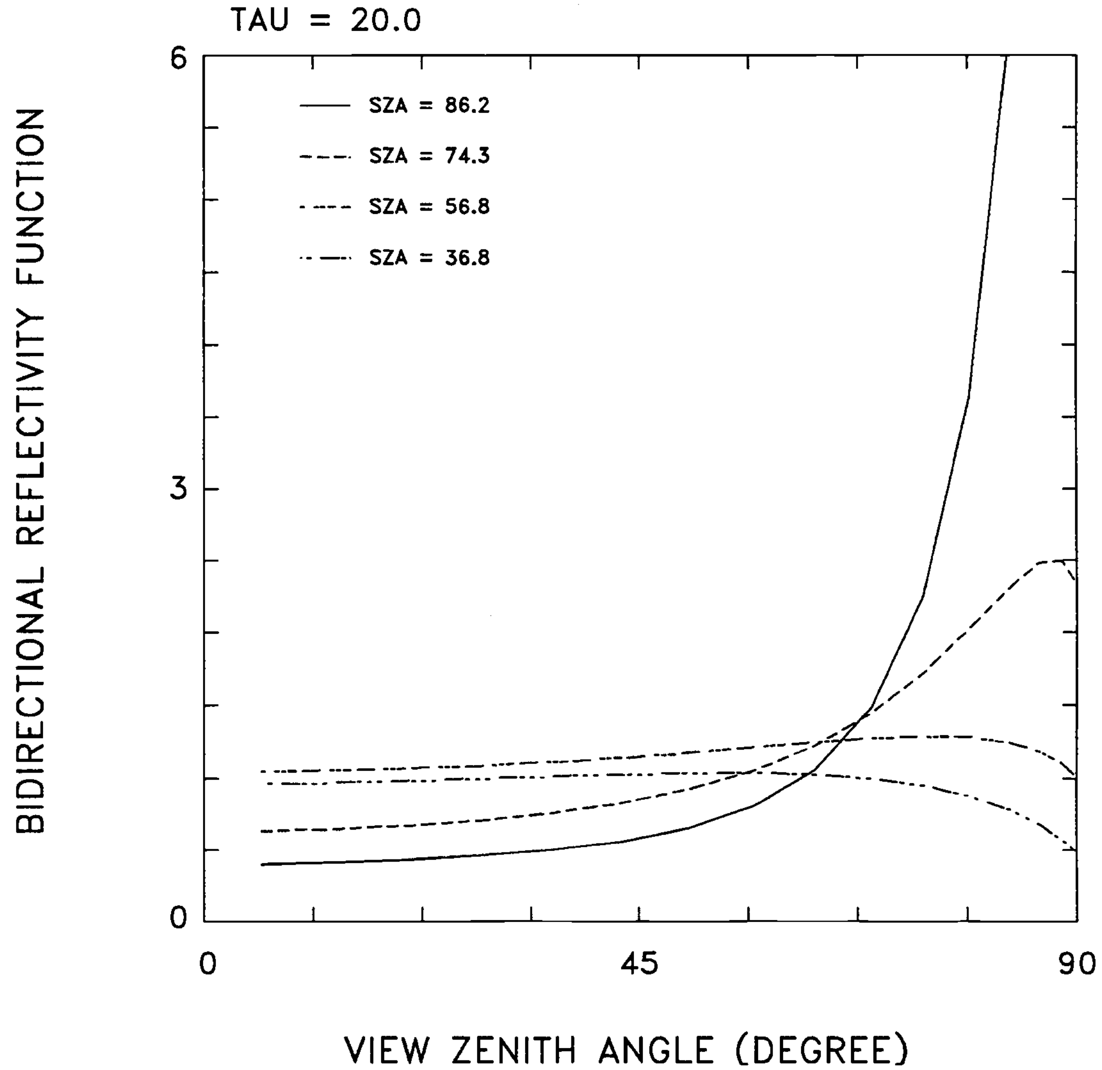

Figure 2.9 Solar zenith angle dependence of the bidirectional reflectivity functions (BDRFs) in the principle plane, $\phi = 0°$. The BDRFs are obtained using the adding-doubling method for a nonabsorbing cloud atmosphere with optical depth $\tau_1 = 20.0$.

2.4 Angular Dependence Of Emitted Longwave Radiation

The radiation emitted from the earth's surface and clouds are attenuated by both scattering and absorbing processes. For clear sky, Rayleigh scattering cross sections, which are of order 10^{-31} cm^2, become negligibly small when compared with cross sections for absorption by molecules (order 10^{-20} cm^2) at infrared wavelengths (Liou, 1980). Moreover, the molecular absorption optical depth are so larger that scattering and absorption by aerosols can often be neglected (Coakley et al. 1983). As a result, the transfer equation for terrestrial radiation generally includes only absorption and emission. It is given by

$$\mu\frac{dI(\tau,\mu)}{d\tau} = I(\tau,\mu) - B(\tau) \tag{2.8}$$

where B(τ) is the blackbody emission. Notice that the emitted longwave radiation is assumed to be azimuthally symmetric because of the random nature of molecular emission (Goody and Yung, 1989). Under the boundary conditions

$$\begin{aligned} I(0,-\mu) &= 0. \\ I(\tau_1,\mu) &= B(\tau_1) \end{aligned} \tag{2.9}$$

(2.8) can be solved. The upward radiances at the top of the atmosphere are given by

$$I(0,\mu) = B(\tau_1)e^{-\tau_1/\mu} + \int_0^{\tau_1} B(\tau')e^{-(\tau'-\tau)/\mu}\frac{d\tau'}{\mu} \ . \tag{2.10}$$

In the case of clouds, the scattering and absorption cross sections of cloud particles can have comparable magnitudes particularly for the parts of the spectrum outside of the molecular absorption bands. The effects of absorption, emission and scattering must be considered together. The radiative transfer equation is now given by

$$\mu\frac{dI(\tau,\mu)}{d\tau} = I(\tau,\mu) - (1-\tilde{\omega})B(\tau) - \frac{\tilde{\omega}}{2}\int_{-1}^{1} P(\mu,\mu')I(\mu,\mu')d\mu' \ . \tag{2.11}$$

The reflectivity and the transmissivity for an isothermal cloud can be obtained by solving (2.11) based on the Eddington approximation (Liou, 1992). The reflectivity is given by

$$R = \frac{(U+1)(U-1)}{N}\left(e^{\lambda\tau} - e^{-\lambda\tau}\right) \tag{2.12}$$

and the transmissivity is given by

$$T = \frac{4U}{N} \tag{2.13}$$

where $N = (U+1)^2 e^{\lambda\tau} - (U-1)^2 e^{-\lambda\tau}$, $U = \frac{3}{2}\frac{(1-\tilde{\omega}g)}{\lambda}$, $\lambda^2 = 3(1-\tilde{\omega}g)(1-\tilde{\omega})$, and g is the asymmetric factor defined by (2.7).

Clouds tend to be optically thick at infrared wavelengths, i.e., $\tau >> 1$. As (2.12) and (2.13) show, in the optically thick limit, $\tau >> 1$, the reflectivity, R, is given by

$$R \rightarrow \frac{(U-1)}{(U+1)} = \frac{\frac{3}{2}(1-\tilde{\omega}g) - \lambda}{\frac{3}{2}(1-\tilde{\omega}g) + \lambda} \; . \tag{2.14}$$

For typical water clouds, $\tilde{\omega} = 0.7$, g = 0.8 and $\lambda = 0.63$, R is equal to 0.03 which is small. The transmissivity, T, is zero. For an optically thick isothermal cloud, it can be easily shown that the net flux of emitted radiation within the cloud is zero. Because of the high opacity of clouds, the net flux of emitted radiation within clouds will be close to zero even in the presence of temperature gradients. As a good approximation, optically thick clouds can be treated as blackbodies. For optical thin clouds such as cirrus, they have non-zero transmissivities but nearly zero reflectivities. For such clouds the small reflectivity is generally ignored and the emissivity, ϵ, is set equal to

$$\varepsilon = 1 - T \tag{2.15}$$

where T is the transmissivity. In either case, clouds can be treated as slabs that interrupt the transfer of radiation through an otherwise absorbing and emitting molecular atmosphere.

The solution of the radiative transfer equation for emitted longwave radiances at the top of the atmosphere is given by

$$I(0,\mu) = B_s(\tau_1)e^{-\tau_1/\mu} + \int_0^{\tau_1} B_a(\tau')e^{-(\tau'-\tau_1)/\mu}\frac{d\tau'}{\mu} \tag{2.16}$$

where τ_1 is the optical depth of the atmosphere, B_s is the emission from the earth's surface, and B_a is the emission for the atmosphere at optical depth τ'. Clearly, for the atmosphere with a fixed optical depth, limb darkening is expected in the angular distribution of emitted radiances. That is, emitted radiances decrease with increasing view zenith angle (decreasing μ). This, however, is not true for an isothermal earth-atmosphere system. As is shown in (2.16), for the isothermal earth-atmosphere system, the right-hand term is given by

$$\begin{aligned} &B_s(\tau_1)e^{-\tau_1/\mu} + B_a \int_0^{\tau_1} e^{-(\tau'-\tau)/\mu}\frac{d\tau'}{\mu} \\ &= B_s(\tau_1)e^{-\tau_1/\mu} + B_a\left(1 - e^{-\tau_1/\mu}\right) \\ &= B_a + (B_s(\tau_1) - B_a)e^{-\tau_1/\mu} \\ &= B_a \end{aligned} \tag{2.17}$$

where B_a is the blackbody emission from the atmosphere. (2.17) shows that the isothermal earth-atmosphere system, i.e., $B_s = B_a$, emits radiation like a blackbody. The emitted radiances at the top of atmosphere are independent of view zenith angle. But if $B_a < B_s$, which is usually the case, then limb darkening occurs.

In conclusion, due to the anisotropic character of scattering and to the variation of optical path length with viewing angle, radiation reflected by the earth-atmosphere is anisotropically distributed. The degree of anisotropy is determined by the cloud optical properties as well as by the solar zenith angle.

3. ANGULAR DEPENDENCE MODELS: DEFINITION AND CONSTRUCTION

3.1 Introduction

The relation between the radiance I in units of $Wm^{-2}sr^{-1}$and the flux πF in units of Wm^{-2} is given by

$$\pi F = \pi I R^{-1} \tag{3.1}$$

where R is the anisotropic factor. R is dimensionless.

Angular dependence models (ADMs) are used to convert radiances observed at a particular view angle to radiative fluxes. In the development of the ADMs, large quantities of satellite scanning measurements, which are able to represent a wide range of earth surfaces and cloud types for all sun-target-satellite geometries, are required. In the case of the Earth Radiation Budget Experiment (ERBE), a set of specially designed instruments aboard the Nimbus-7 satellite were used to obtain ADMs. A biaxial scanning instrument was used to obtain observations for a wide range of viewing geometries (Jacobowitz et al., 1984). Two auxiliary instruments: the Nimbus-7 Temperature and Humidity Infrared Radiometer (THIR) and Total Ozone Mapping Spectrometer (TOMS) were used to classify cloud types (Stowe et al., 1988). Using Nimbus-7 ERB scanner measurements, Taylor and Stowe (1984) developed the ERBE ADMs for four clear uniform surface types; water, land, snow and ice, and four uniform overcast cloud scene types: low, middle, high water, and high ice clouds. Further studies suggested that the fraction of cloud cover is likely to be the most crucial factor in the determination of the ADMs (Davies, 1984). As a result, Suttles et al. (1988, 1989) improved the Nimbus-7 ADMs by defining a set of ADMs which cover the range of cloud conditions in four categories; clear (0% – 5% cloud cover), partly cloudy (5% – 50%), mostly cloudy (50% – 95%), and overcast (95% – 100% cloud cover). These four cloud categories were combined

Table 3.1 Scene types for the ERBE angular dependence models (from Suttles et al., 1988).

Scene type	Cloud cover, %
Clear ocean	0 to 5
Clear land	"
Clear snow	"
Clear desert	"
Clear land-ocean mix	"
Partly cloudy ocean	5 to 50
Partly cloudy over land or desert	"
Partly cloudy land-ocean mix	"
Mostly cloudy ocean	50 to 95
Mostly cloudy land or desert	"
Mostly cloudy land-ocean mix	"
Overcast	95 to 100

with four uniform surface types: ocean, land, desert, ice/snow and an ocean/land mix to form twelve scene types for the ERBE ADMs as listed in Table 3.1.

A detailed description of the development of the ERBE ADMs is given by Suttles et al. (1988, 1989). Each radiance pair of Nimbus-7 ERB scanning radiometer measurements was located in one of 18630 equal-area regions of approximately (160 km)^2 each. The observations were tagged with 1) solar zenith, view zenith and relative azimuthal angles, 2) surface type and 3) cloud condition. The surface type was obtained from a static geographic map. The cloud condition was determined by analysis of high-resolution (6 km) THIR data and moderate-resolution (50 km) TOMS data. The ADMs were then derived statistically as will be shown in the next section. It must be pointed out that the cloud scene identification used to derive the ADMs should be the same as that used when the ADMs are applied. Usually they are not. For example, for ERBS, there were no THIR and TOMS instruments. As a result, a maximum likelihood estimation (MLE) cloud scene identification was developed to reproduce the THIR and

TOMS results on the basis of scanner shortwave and longwave radiance pairs (Wielicki and Green, 1989).

The formalism for the angular dependence models (ADMs), as well as several functions that describe the anisotropy for purposes of comparing the anisotropy associated with different scenes, will be given in section 3.2. The MLE scene identification and its application will be discussed in section 3.3. Finally, examples of the ERBE ADMs will be presented in section 3.4. A summary of the general characteristics of the ERBE ADMs will also be given.

3.2 Basic Definitions

3.2.1 Angular Coordinate System

The angular coordinate system used in this investigation follows that used in ERBE. Fig. 3.1 illustrates the coordinate system.

The target area is at latitude Θ and longitude Φ on the Earth. The solar zenith angle is θ_o. The principal plane is the plane containing the ray from the sun to the target area and the zenith ray that is normal to the target area. The energy reflected or emitted from the earth-atmosphere system is measured by the satellite at zenith angle θ and a relative azimuthal angle ϕ which is measured from the principal plane. $\phi = 0^o$ corresponds to reflection in the direction of forward scattering, and $\phi = 180^o$ corresponds to reflection in the direction of backward scattering.

3.2.2 Reflected Radiative Flux

Because the earth's surfaces are not homogeneous, the radiance I reflected by the earth-atmosphere system is not only a function of the solar zenith angle, θ_o, the viewing zenith θ, the relative azimuth ϕ, but also a function of colatitude Θ, longitude Φ. The colatitude Θ is the angle which is 0° at the north pole and increases to 180° at the south pole. As was discussed in chapter 1, the reflected radiances and fluxes are related by

$$\pi F(\Theta,\Phi;\theta_0) = \int_0^{2\pi} d\phi \int_0^{\frac{\pi}{2}} d\theta \sin\theta \cos\theta I(\Theta,\Phi;\theta_0,\theta,\phi) \ . \tag{3.2}$$

A bidirectional reflectance function (BDRF) is introduced to describe the angular

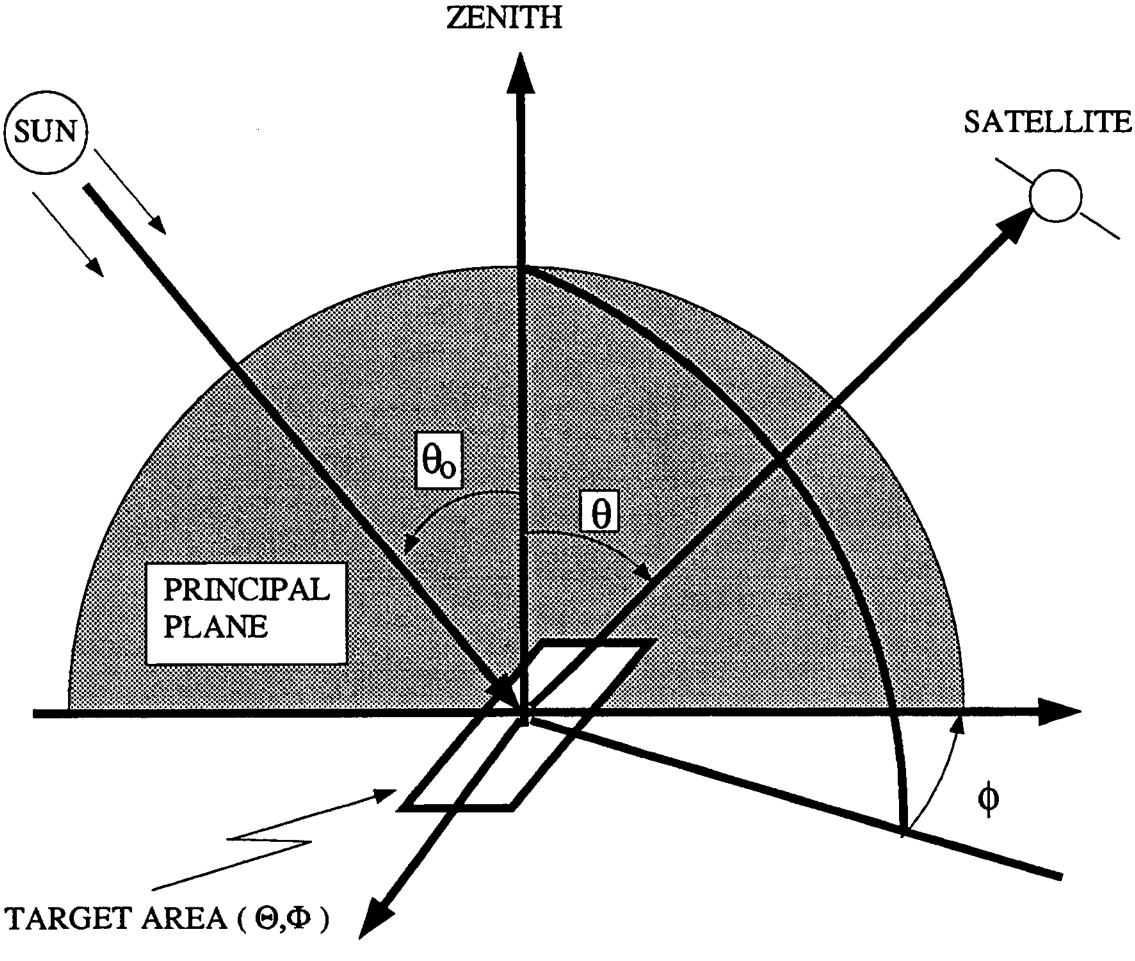

Figure 3.1 Sun, satellite, and target geometry. In the figure, θ_0 is the solar zenith angle, θ is the satellite view zenith angle, and ϕ is the relative azimuth angle. The plane which includes both incident direction and zenith direction is called the principal plane.

characteristics of reflected radiation field. The BDRF is defined as the ratio of the radiative flux reflected by an equivalent Lambertian surface to the actual flux:

$$BDRF(\Theta,\Phi;\theta_0,\theta,\phi)=\frac{\pi I(\Theta,\Phi;\theta_0,\theta,\phi)}{\pi F(\Theta,\Phi;\theta_0)}\ . \tag{3.3}$$

Thus, if the radiance is Lambertian, that is, independent of viewing zenith and azimuth angles, then

$$\pi F(\Theta,\Phi;\theta_0)=\pi I(\Theta,\Phi;\theta_0) \tag{3.4}$$

and

$$BDRF(\Theta,\Phi;\theta_o)=1\ . \tag{3.5}$$

Substituting (3.3) into (3.2), the normalization property for the $BDRF(\Theta,\Phi;\theta_0,\theta,\phi)$ is found to be given by

$$\pi^{-1}\int_0^{2\pi}d\phi\int_0^{\frac{\pi}{2}}d\theta\sin\theta\cos\theta BDRF(\Theta,\Phi;\theta_0,\theta,\phi)=1\ . \tag{3.6}$$

Moreover, by definition the albedo is given by

$$\alpha(\Theta,\Phi;\theta_0)=\frac{\pi F(\Theta,\Phi;\theta_0)}{\cos\theta_0 E_0} \tag{3.7}$$

where E_0 is the solar constant corrected for the Earth-Sun distance and $\pi F(\Theta,\Phi,\theta_0)$ is the reflected radiative flux. The BDRF and albedo are related by

$$\alpha(\Theta,\Phi,\theta_0)=\frac{\pi I(\Theta,\Phi;\theta_0,\theta,\phi)}{BDRF(\Theta,\Phi;\theta_0,\theta,\phi)\cos\theta_0 E_0}\ . \tag{3.8}$$

3.2.3 Emitted Radiative Flux

Thermal emission is the process by which molecular internal energy is transferred to radiative energy. Because of the random nature of molecular emission, emitted longwave radiation is assumed to be azimuthally symmetric (Goody and Yung, 1989). For longwave radiation, a limb-darkening function (LDF) is defined as

$$LDF(\Theta,\Phi,t;\theta)=\frac{\pi I(\Theta,\Phi,t;\theta)}{\pi F(\Theta,\Phi,t)} \tag{3.9}$$

with the normalization condition given by

$$2\int_{0}^{\frac{\pi}{2}} d\theta \sin\theta \cos\theta LDF(\Theta,\Phi,t;\theta)=1 \tag{3.10}$$

where t is the time of observation. It should be pointed out that unlike the BDRF, time is included in the limb-darkening models because the emitted longwave radiation is determined by factors, such as surface temperature, atmospheric composition and lapse rate. These factors vary significantly with time (Taylor et al., 1983). For shortwave radiation (wavelength < 4 μm), such variations do not influence reflected broadband shortwave radiances appreciably. So, the BDRFs used in ERBE are assumed to be independent of time.

The emitted longwave flux is given by

$$\pi F(\Theta,\Phi,t)=2\pi\int_{0}^{\frac{\pi}{2}} d\theta \sin\theta \cos\theta I(\Theta,\Phi,t;\theta)\ . \tag{3.11}$$

3.2.4 Formulation Of Angular Dependence Models

ERBE used discrete representations of the ADMs. In discrete form the relationship between the radiative flux and intensity is given by

$$F_i = \sum_{k=1}^{8} (\phi_{k+1} - \phi_k) \sum_{j=1}^{7} \bar{I}_{ijk} (\sin^2 \theta_{j+1} - \sin^2 \theta_j) \ . \tag{3.12}$$

The BDRF is given by

$$R_{ijk} = \frac{\pi \bar{I}_{ijk}}{\sum\limits_{m=1}^{8} (\phi_{m+1} - \phi_m) \sum\limits_{n=1}^{7} \bar{I}_{imn} (\sin^2 \theta_{n+1} - \sin^2 \theta_n)} \tag{3.13}$$

with the normalization condition

$$\pi^{-1} \sum_{k=1}^{8} (\phi_{k+1} - \phi_k) \sum_{j=1}^{7} R_{ijk} (\sin^2 \theta_{j+1} - \sin^2 \theta_j) = 1 \ . \tag{3.14}$$

Index i refers to solar zenith angle, index j refers to viewing zenith angle, and index k refers to azimuth angle. The discrete approximation of BDRF, R_{ijk}, is called the anisotropic factor. The angular bins used for the ADMs are listed in the Table 3.2 for shortwave models and the Table 3.3 for longwave models.

The longwave radiances are assumed to change with colatitude Θ, time of year t, and viewing zenith angle θ. For time variations, the four seasons (based on the Northern Hemisphere) are winter (December, January, and February), spring (March, April, and May), summer (June, July, and August), and fall (September, October, and November). Also, the integrals in (3.11) and (3.9) can be written in the discrete forms

$$F_{nq} = \sum_{j=1}^{7} \bar{I}_{njq} (\sin^2 \theta_{j+1} - \sin^2 \theta_j) \tag{3.15}$$

and

$$R_{njq} = \frac{\bar{I}_{njq}}{\sum_{m=1}^{7} \bar{I}_{nmq}\left(\sin^2\theta_{m+1} - \sin^2\theta_m\right)} \tag{3.16}$$

with the normalization condition

$$2\sum_{j=1}^{7} R_{njq}\left(\sin^2\theta_{j+1} - \sin^2\theta_j\right) = 1 \tag{3.17}$$

where index n refers to colatitude, index j refers to viewing zenith angle, and index q refers to time of year with seasonal resolution.

Nimbus-7 ERB data was used to develop the ERBE ADMs. All available measurements were collected and binned according to the solar zenith angle, view zenith angle, relative azimuth angle, colatitude and longitude of the observation in order to describe the angular variation of radiances for each scene type. Although smaller bin sizes lead to better descriptions of the angular variation, it was found that the numbers of observations at some angles were too small for accurate estimates of the mean radiances. As a result, a compromise was reached between discrete bin errors and sample errors of the mean. Recently, Dlhopolsky and Cess (1992) argued that the bin size of the ERBE ADMs was unsatisfactory. Their results showed that higher resolution of the angular bins, especially for small relative azimuth angles, was needed to significantly reduce the errors in the estimated albedo for clear oceans. In this investigation, no effort is made to assess the effect of the bin size on the ADMs. The angular bins used here are those used in ERBE.

In constructing ADMs, it is assumed that all like surfaces reflect similarly. That is, the Atlantic Ocean reflects radiation like the Pacific or the Indian Ocean. The Sahel desert reflects like the Mojave or the Gobi desert, etc. With this assumption the ADMs are determined by compiling and averaging observations with equal weights for a particular scene type independently of geographic location (Θ, Φ). Although it has been shown that oceans do not have the same reflectivity and deserts do not have the same reflectivity

(Eaton and Dirmhirn, 1979; Davis and Cox, 1982), no assessments have been made of the errors in ADMs.

Table 3.2 Angular bin definitions for shortwave radiation (from Suttles et al., 1988).

Bin Number	Solar zenith angle θ_o, deg	Viewing zenith angle θ, deg	Azimuthal angle ϕ, deg
1	0 to 25.84	0 to 15	0 to 9
2	25.84 to 36.87	15 to 27	9 to 30
3	36.87 to 45.57	27 to 39	30 to 60
4	45.57 to 53.13	39 to 51	60 to 90
5	53.13 to 60.00	51 to 63	90 to 120
6	60.00 to 66.42	63 to 75	120 to 150
7	66.42 to 72.54	75 to 90	150 to 171
8	72.54 to 78.46		171 to 180
9	78.46 to 84.26		
10	84.26 to 90.00		

Table 3.3 Angular bin definitions for longwave radiation (from Suttles et al., 1989).

Bin Number	Viewing zenith angle θ, deg	Colatitude angle Θ, deg
1	0 to 15	0 to 18
2	15 to 27	18 to 36
3	27 to 39	36 to 54
4	39 to 51	54 to 72
5	51 to 63	72 to 90
6	63 to 75	90 to 108
7	75 to 90	108 to 126
8		126 to 144
9		144 to 162
10		162 to 180

3.2.5 Measures Of Anisotropy

Here, simple measures of anisotropy are defined. They will facilitate the comparison of BDRF and LDF for various scene types. A new function is introduced to measure the absolute degree of anisotropy (DA). DA is the absolute deviation of the BDRF from isotropy. It is given by

$$DA(\Theta, \Phi, t; \theta_0) = \int_0^{2\pi} d\phi \int_o^{\pi/2} |BDRF(\Theta, \Phi, t; \theta_0, \theta, \phi) - 1| d\theta \ . \tag{3.18}$$

The azimuthally averaged anisotropy is used to show the degree of anisotropy for different solar zenith angles. For a particular solar zenith angle, the azimuthally averaged anisotropy (AAA) is given by

$$AAA(\Theta, \Phi, t; \theta_0, \theta) = \pi^{-1} \int_0^{2\pi} d\phi BDRF(\Theta, \Phi, t; \theta_0, \theta, \phi) \ . \tag{3.19}$$

It is a function of view zenith angle and has a normalization condition obtained from (3.6)

$$\int_0^{\frac{\pi}{2}} d\theta \cos\theta \sin\theta AAA(\Theta, \Phi, t; \theta_0, \theta) = 1 \ . \tag{3.20}$$

DA can be written in terms of AAA,

$$DA(\Theta, \Phi, t; \theta_0) = \int_0^{\pi/2} |AAA(\Theta, \Phi, t; \theta_0, \theta) - 1| d\theta \ . \tag{3.21}$$

For different scene types, large values of DA imply that the reflected or emitted radiation is highly anisotropic.

3.3 The Maximum Likelihood Estimate Cloud Scene Identification

The proper identification of scene type is a key element in the accurate estimation of radiative fluxes at the top of the atmosphere (Smith et al., 1986; Wielicki and Green, 1989). Scene type of the underlying surface is known from a static geographic map. The scene identification discussed here classifies cloud cover conditions. These conditions are functions of fractional cloud cover, cloud height, cloud type, and cloud microphysical properties (such as particle size and particle distribution). Wielicki and Green (1989) review the evolution of scene identification methods. Here, the MLE method and its application for ERBE observations is briefly described.

In statistical estimation theory, the MLE method is the most general and powerful estimation procedure. The MLE method has the property that given a large enough sample number, the probability that estimators differ from the true values goes to zero (Kendall and Stuart, 1961). Estimators with this attribute are called consistent estimators. Also, the MLE estimators have the highly desirable property of being asymptotically normal and asymptotically efficient, i.e., they produce the minimum variance, for large samples under general conditions (Cramer, 1946).

Given a sample of n observations $\{x_i\}$ from a known distribution, MLE estimates the unknown parameters $\{\vartheta_i\}$ of the sample by choosing the most probable value of $\{\vartheta_i\}$ through maximizing the likelihood function, L. L is given by

$$L = p(x_1|\theta_1, \theta_2, ..., \theta_k)...p(x_n|\theta_1, \theta_2, ..., \theta_k) \tag{3.22}$$

where $p(x_i|\theta_1, ..., \theta_k)$ is the distribution function of $\{x_i\}$.

Consider the cloud type associated with measurement pair I_{sw} and I_{lw}, and a known surface type: ocean, land, desert, ice/snow, or coastal. The probability that the measurement was from cloud type q is

$$P(I_{sw}, I_{lw}\, are\ from\ q) = P(I_{sw}, I_{lw}|q)P(q) \tag{3.23}$$

where the conditional probability $P(I_{sw}, I_{lw}|q)$ is modeled by a bivariate normal distribution given by

$$P(I_{sw}, I_{lw}|q) = \frac{e^{-(Q/2)}}{2\pi\sigma_{sw}^{q}\sigma_{lw}^{q}\left[1-(\rho^{q})^{2}\right]^{1/2}} \tag{3.24}$$

and

$$Q = \frac{1}{\left[1-(\rho^{q})^{2}\right]}\left[\left(\frac{I_{sw}-L_{sw}^{q}}{\sigma_{sw}^{q}}\right)^{2} - 2\rho^{q}\left(\frac{I_{sw}-L_{sw}^{q}}{\sigma_{sw}^{q}}\right) \times \left(\frac{I_{lw}-L_{lw}^{q}}{\sigma_{lw}^{q}}\right) + \left(\frac{I_{lw}-L_{lw}^{q}}{\sigma_{lw}^{q}}\right)^{2}\right] . \tag{3.25}$$

Nimbus-7 ERB data provided all of the parameters: the standard deviations $\sigma_{sw}^{q}, \sigma_{lw}^{q}$, the expected shortwave and longwave radiances L_{sw}^{q}, L_{lw}^{q}, the shortwave-longwave correlation coefficient ρ^{q}, and $P(q)$, the probability that a given observation had scene type q. Fig. 3.2 illustrates these quantities for the four cloud conditions in a bispectral diagram.

In the case of ERBE, the values of the parameters which were needed for the calculation of (3.23) were obtained from the Nimbus-7 ERB observations. It was assumed that the mean shortwave and longwave radiances varied according to a bivariate normal distribution. Cloud conditions were divided into four categories; clear, partly cloudy, mostly cloudy, and overcast. The cloud type with the highest probability of occurrence (the maximum likelihood in statistical sense) was assigned for each shortwave and longwave radiance pair.

It must be pointed out that for a particular geographic location and a particular sun-earth-satellite viewing geometry, both the shortwave and the longwave radiances vary with cloud cover, three dimensional cloud structures, cloud type, cloud microphysical properties, and other atmospheric variables (haze, aerosols), etc. These factors can cause large variations in the shortwave and longwave radiances within each cloud class. As shown in Fig. 3.2, the distribution of measurement pairs within each class is represented by equiprobability ellipses which in turn are characterized by the mean values (crosses), the standard deviations (proportional to the lengths of the axes of the ellipses), and the correlations between the longwave and shortwave radiances (shown by the tilt of the principal axes of the ellipses with respect to the radiance coordinate system). In the example, the longwave and shortwave radiances for a single field of view are indicated by the dot. The MLE assigns the indicated observation in this example to the mostly cloudy category. This assignment is the most probable given the values of the shortwave and longwave radiances.

Clearly, the validity of the scene identification obtained with the MLE method depends on the Nimbus–7 ERB scanning radiometer observations and the THIR/TOMS scene identification.

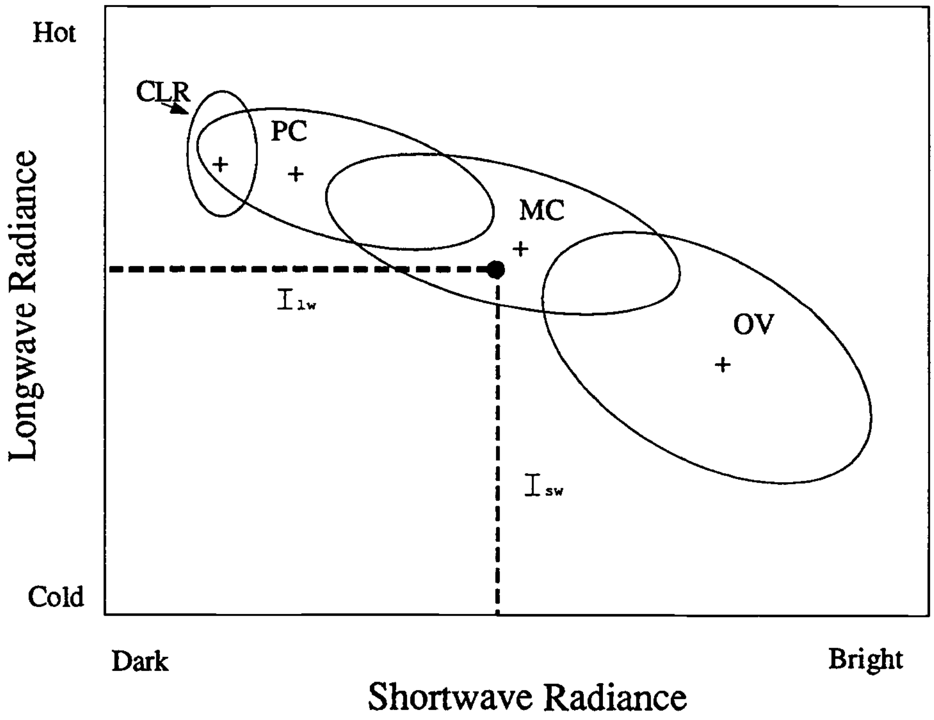

Figure 3.2 Schematic diagram of Maximum Likelihood Estimation scene identification.

3.4 Examples Of The ERBE ADMs

Fig. 3.3 gives examples of the ERBE ADMs in polar coordinates. The coordinate axes are view zenith angle, which increases in the radial direction, and azimuthal angle, which increases counterclockwise in the polar direction. The figure shows anisotropic factors for the three cloud-cover conditions over oceans and for overcast scenes with overhead sun (solar zenith angle $0 < \theta_o < 25.8^o$). The dependence of the reflected radiances on sun-target-satellite geometry is evident. The maximum anisotropy is generally in the forward scattering direction.

The azimuthally averaged anisotropy is shown in Fig. 3.4 as a function of viewing zenith angle for two different solar zenith angle bins $0 < \theta_o < 25.8^o$ and $60^o < \theta_o < 66.4^o$. For small solar zenith angles, the azimuthally averaged anisotropy decreases with increasing viewing zenith angle. The dominance of specular reflection in the anisotropy appears for clear ocean scenes. For large solar zenith angles, the azimuthally averaged anisotropy increases with view zenith angle (i.e., a limb-brightening effect). Shown in Fig. 3.5 is the degree of anisotropy defined in (3.18) as a function of solar zenith angle. The degree of anisotropy decreases as the cloud amount increases from clear sky (cloud cover < 5%) to overcast (cloud cover > 95%). For fixed solar zenith angle, the degree of anisotropy, however, does not decrease linearly with increasing cloud cover. Generally the four cloud scene types become more anisotropic with increasing solar zenith angle.

Several characteristics of ADMs are summarized as follows: 1) anisotropic factors increase with viewing zenith angle (i.e., limb brightening); 2) the largest anisotropic factors occur in the principal plane, where the azimuthal angle is 0^o or 180^o, and the smallest occur around an azimuthal angle of 90^o; 3) for solar zenith angles near 0^o (overhead sun), the models are the closest to being Lambertian (isotropic reflection). They become less Lambertian with increasing solar zenith angles.

Examples of ERBE longwave angular models for ocean and overcast scenes are given in Fig. 3.6. The figure shows examples for the north pole, the tropics and the south pole in the northern hemisphere fall (September, October, November). Limb-darkening exists for all scenes. Suttles et al. (1989) concluded that the mean anisotropic factors show a dependence on the view zenith angle for all scene types and these factors are nearly independent of scene type, colatitude, and season.

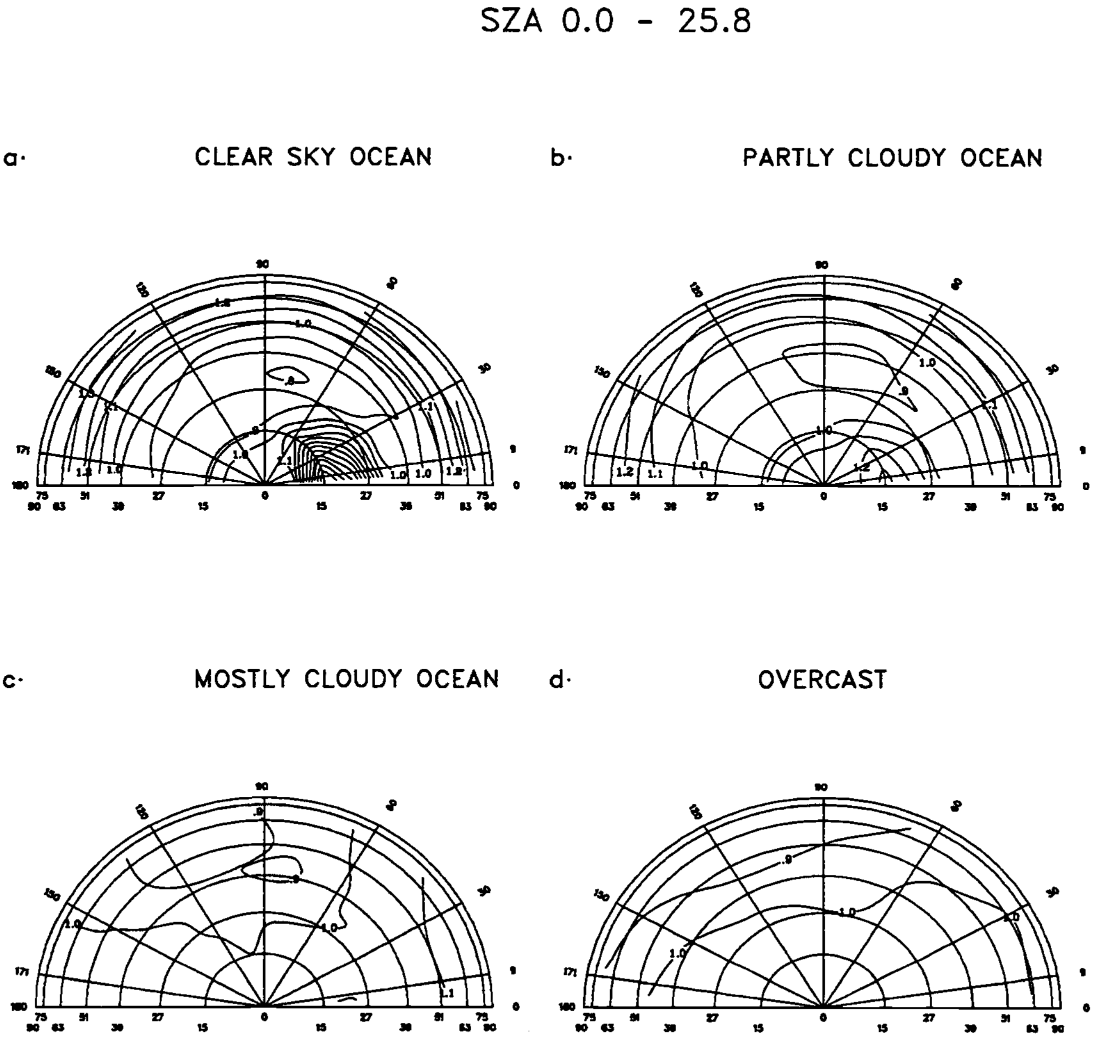

Figure 3.3 Examples of ERBE angular dependence models for ocean and overcast scenes with overhead sun. The radial axis is the view zenith angle which increases from the origin, and the polar axis is the relative azimuth angle which increases counterclockwise. The contours are of anisotropic factors with an increment of 0.1.

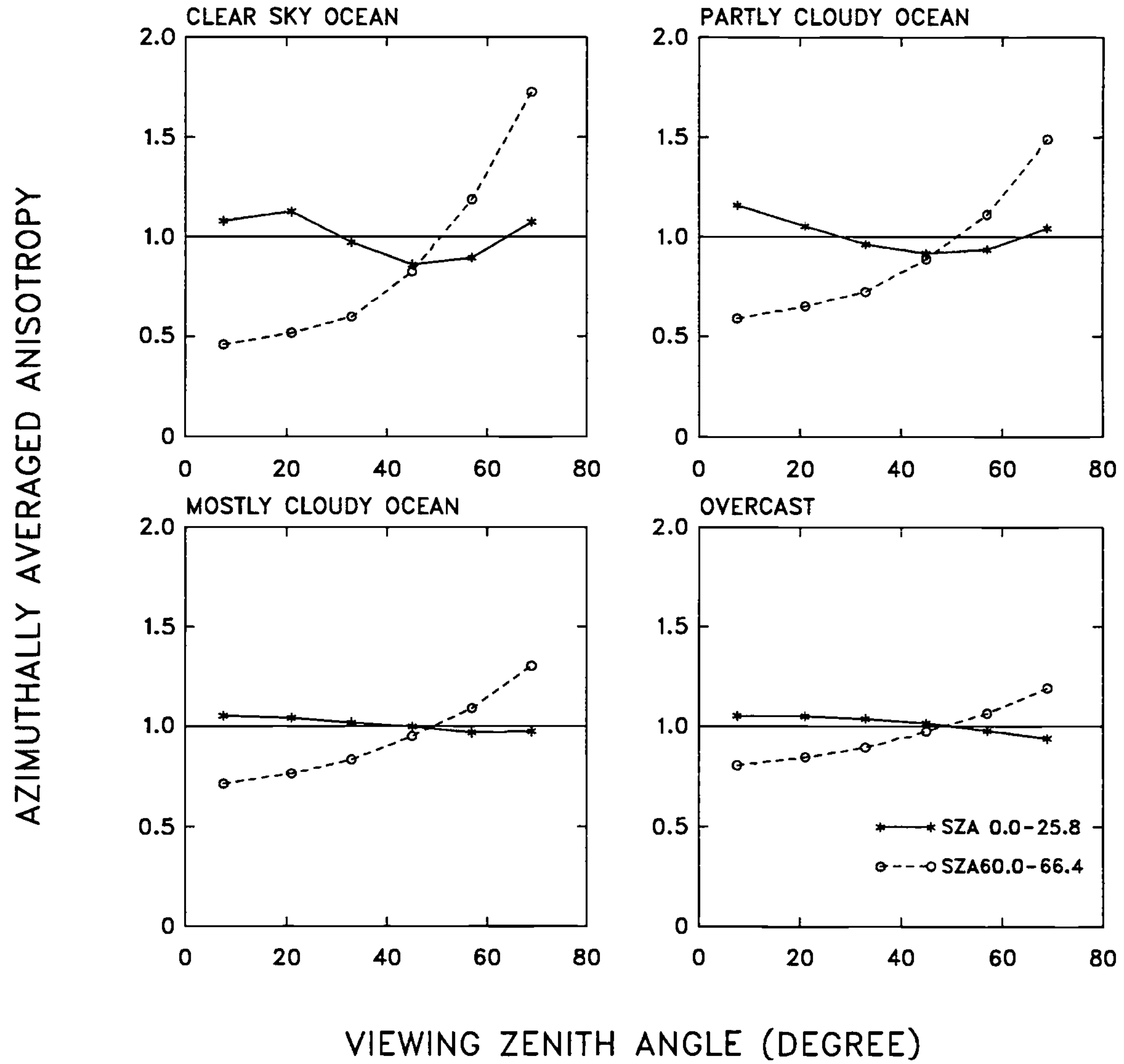

Figure 3.4 Examples of azimuthally averaged anisotropy for solar zenith angles $0 < \theta_o < 25.8^o$ (solid lines) and $60^o < \theta_o < 66.4^o$ (dashed lines). The azimuthally averaged anisotropy equals one for isotropic cases.

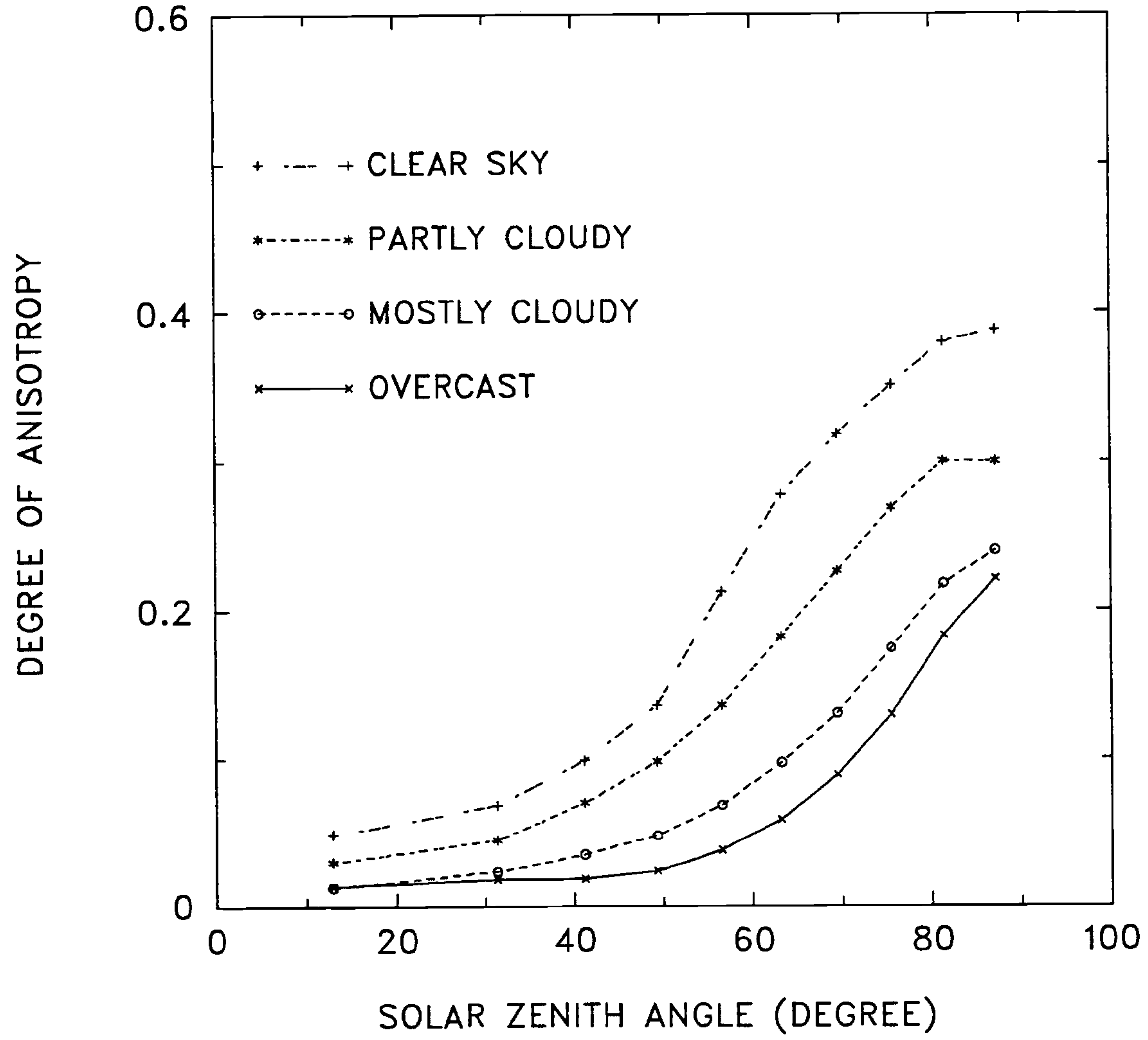

Figure 3.5 Examples of degree of anisotropy for the three cloud conditions over oceans and for overcast scenes as a function of solar zenith angle. For isotropic reflection, the degree of anisotropy equals zero.

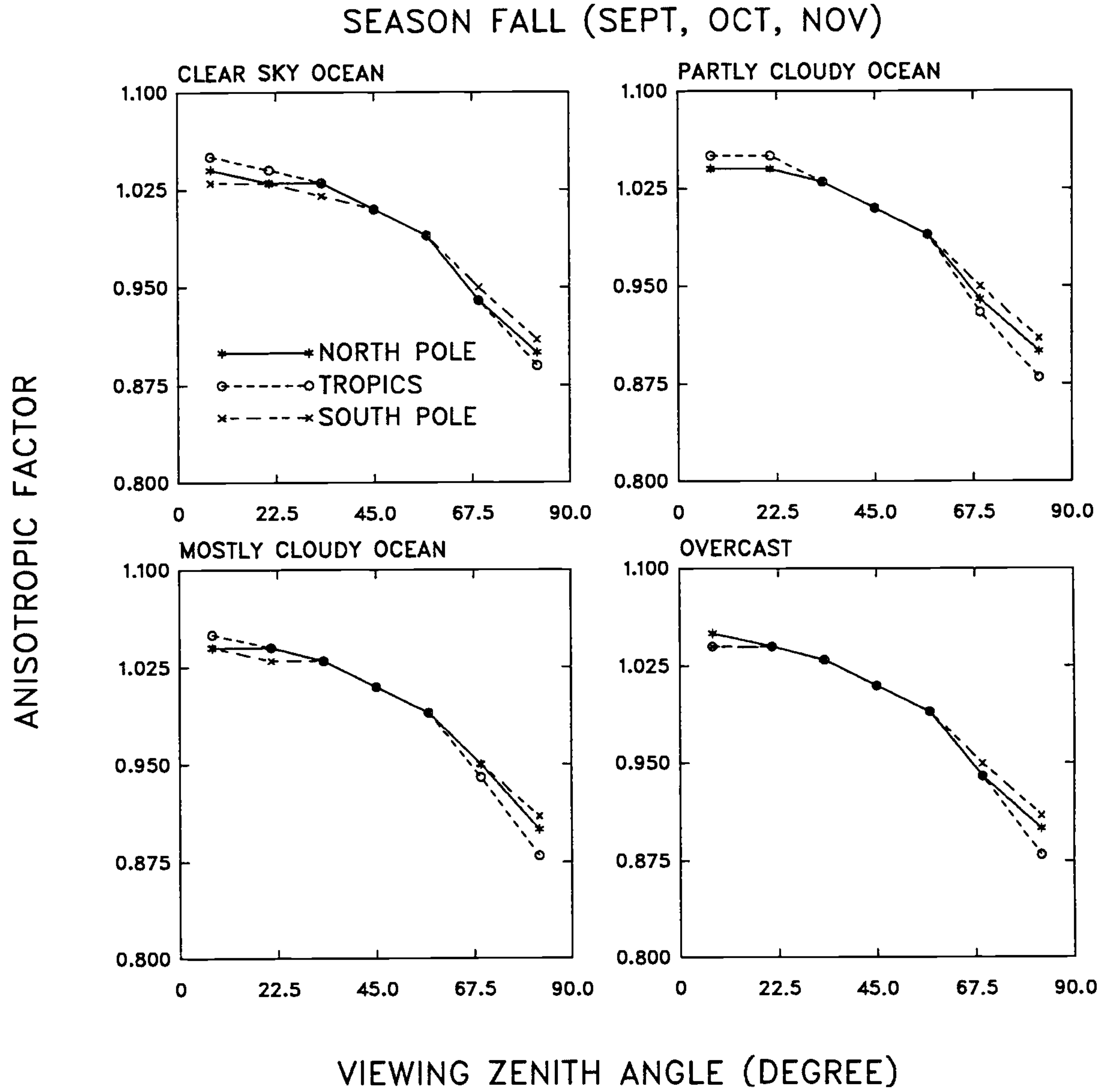

Figure 3.6 Examples of limb-darkening models for the north pole, the tropics and the south pole in the northern hemisphere fall (September, October, November). For isotropic emission, the anisotropic factor equals unity.

4. SENSITIVITY OF OBSERVED ANISOTROPY TO SCANNER SPATIAL RESOLUTION

4.1 Introduction

In ERBE, angular dependence models (ADMs) are used to convert satellite scanning radiometer measurements to radiative fluxes at the top of the atmosphere. Because there are distinguishable characteristics of angular distribution for the radiation emanating from different scenes, one must apply an appropriate ADM for the scene being viewed in order to obtain an accurate estimate of the flux (Davis and Cox, 1982; Smith et al., 1986; Baldwin and Coakley, 1991). As was discussed in the previous chapter, ERBE ADMs give anisotropic factors for 12 scene types, i.e., five surface types: ocean, land, snow/ice, desert and coast combined with four cloud types: clear, partly cloudy, mostly cloudy and overcast, in 560 angular bins of the sun-earth-view geometry (Suttles et al., 1988, 1989). They are the most complete set of angular models currently being used for the conversion of radiance to flux.

Nimbus–7 ERB scanning radiometer measurements were used to construct the ERBE ADMs (Suttles et al., 1988, 1989). The scene types of the Nimbus-7 ERB observations were identified by using the measurements from the THIR/TOMS instruments (Taylor and Stowe, 1984). The ERBE ADMs should be applied with the same scene identification method used to derive them. Unfortunately, the Earth Radiation Budget Satellite (ERBS) had no THIR/TOMS instruments for scene identification. A maximum likelihood estimation (MLE) method was developed to provide scene identification on the basis of broadband shortwave and longwave radiance pairs. The link between radiance pairs and scene type was based on the Nimbus-7 ERB statistics (Wielicki and Green, 1989). Good agreement was found between the cloud fraction derived from the ERBE MLE method and that identified by the THIR/TOMS method (Suttles et al., 1992).

In principle, the anisotropic factor should depend only on the scene type and sun-earth-view geometry. Because the field of view of a scanning radiometer grows from nadir to limb, the ADMs should be independent of spatial resolution. The ERBE ADMs were applied as if the models were independent of variations in the instrument field of view size with varying view zenith angle. Because cloud optical properties vary greatly over relatively small spatial and temporal scales, using coarse bispectral radiance pairs for scene identification, the ERBE MLE is subject to identification errors. The ERBE scene identification errors are thought to vary systematically with view zenith angle. The systematic errors are due to the nature of cloud spatial distribution combined with the growth of scanner field of view size from nadir to limb. If clouds were uniformly distributed in space, then cloud scene types identified using scanner measurements would not be influenced by changes in field of view size with view zenith angle. Clouds are not uniformly distributed in space but tend to cluster on specific spatial scales (Chang and Coakley, 1993). Thus, fields of view at nadir which are identified as clear or overcast scenes are most likely extracted from the midst of broken cloud systems. They are subject to cloud or clear contamination. In contrast, fields of view near the limb identified as clear or overcast scenes, provided they are actually clear or overcast, are likely to be surrounded by clear or overcast scenes, and are subject to less cloud or clear contamination. Therefore, due to the effect of cloud clustering combined with the growth of field of view size from nadir to limb, there could well be a varying degree of cloud (or clear) contamination from nadir to limb in the scanning radiometer measurements.

As was shown in chapter 3, anisotropy of reflected and emitted radiation is sensitive to the degree of cloud cover. The varying degree of cloud (or clear sky) contamination affects the anisotropy of the observed radiances. For example, regions identified as being cloud-free and have less cloud contamination should reflect and emit radiation that is more anisotropic than similar regions which have more cloud contamination. Consequently, because of scene identification errors the anisotropy obtained with ERBE scanner observations is expected to depend on the spatial resolution of the observations.

If the scanner had a constant spatial resolution from nadir to limb, i.e., the size of the field of view did not vary with increasing view zenith angle, the measurements would be expected to have a constant degree of cloud or clear sky contamination from nadir to limb. This expectation assumes, of course, that aside from effects due to cloud clustering there are no other factors affecting the view zenith angle dependence of scene identification errors. In order to search for the effect of the varying degree of cloud or clear contamination on the ADMs, a sensitivity test is conducted by comparing the anisotropy derived from the observations which have a nearly constant size field of view with that of full resolution scanner observations. Observations which have a constant size field of view are constructed from ERBS scanner observations by summing fields of view at nadir to form a single field of view whose size matches a single ERBS scanner field of view near the limb.

4.2 ERBS Scanning Radiometer

The data used in this investigation are taken from global ERBS scanning radiometer measurements for September, October, November, 1986. ERBS was launched from space shuttle mission 41–G on October 5, 1984. The satellite achieved an orbit at an altitude of 610 km and an inclination of 57°. The scanning radiometer on board has three channels: a shortwave channel, which covers 0.2 – 5.0 μm, a longwave channel, which covers 5.0 – 50.0 μm, and a total channel, which covers 0.2 – 50.0 μm (Kopia, 1986). The spectral range of the scanners covers a large portion of the entire solar and earth radiation spectrum. Only unfiltered shortwave and longwave radiances are used. These radiances are the raw measurements after corrections have been made for the spectral filters of the radiometer.

The ERBS scanner has a fixed 3.0° × 4.5° hexagonal aperture. The size of the field of view (FOV) at ground increases from about $(40\ \mathrm{km})^2$ at nadir to about $(300\ \mathrm{km})^2$ at the limb. Fig. 4.1 schematically illustrates how the size of the FOV increases with satellite view zenith angle. The radiometric samples were taken at nadir angles separated by 2.2°.

There is an overlap in both the scanning and the satellite orbit directions. Table 4.1 lists the average size of the FOV for each view zenith angle bin used in the ERBE ADMs.

Table 4.1 Bin averaged ERBE scanner field of view size from nadir to limb.

Bin No.	View zenith angle (degree)	Length along scanning direction (km)	Length along satellite track direciton (km)	Size of area (10^4 km^2)
1	7.24	32.665	48.445	0.158
2	21.80	36.978	51.381	0.190
3	32.89	44.716	56.184	0.252
4	44.34	60.862	64.724	0.396
5	56.49	97.841	79.849	0.790
6	69.03	215.678	109.231	2.440
7	79.48	550.564	151.091	8.319

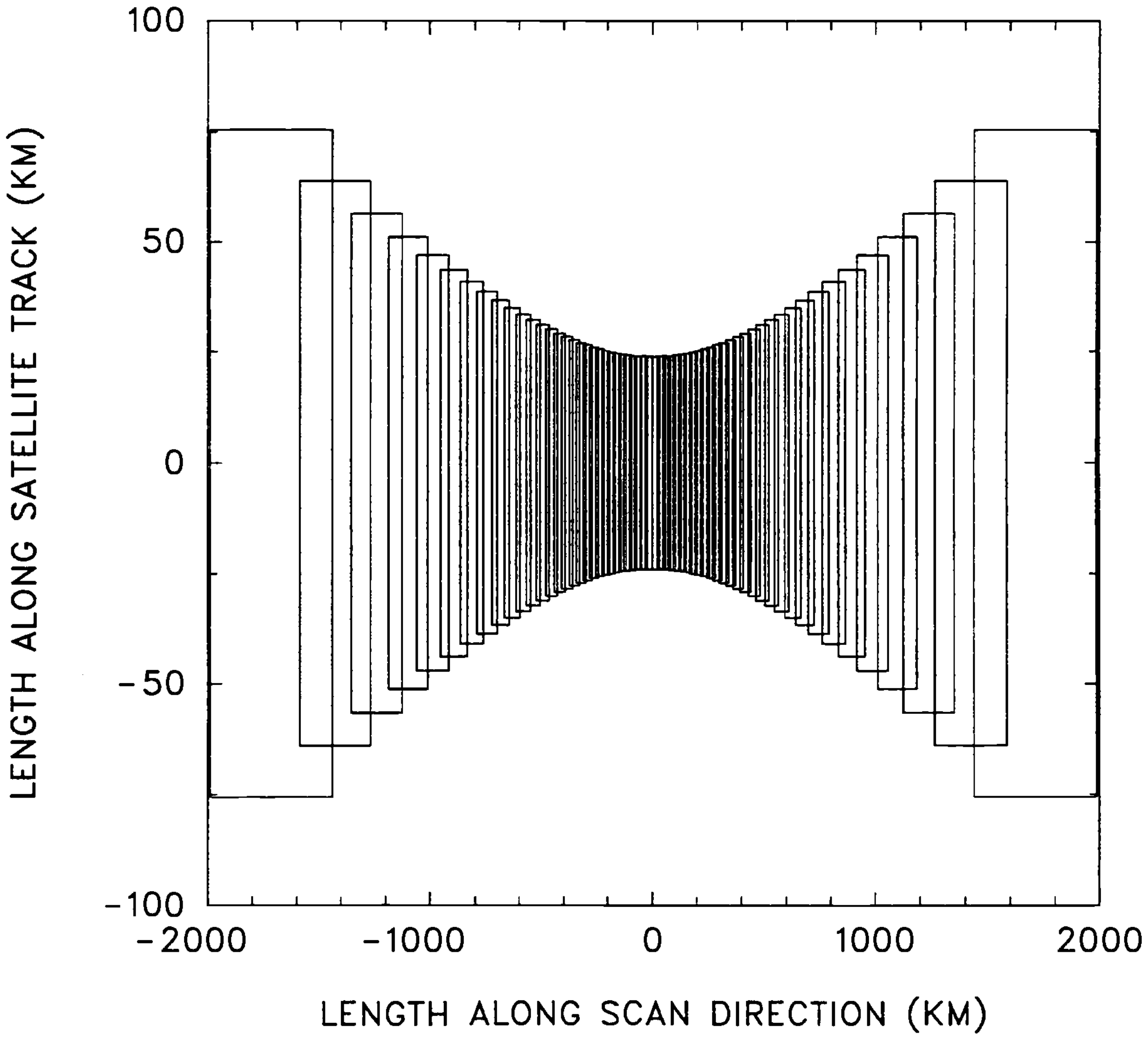

Figure 4.1 Schematic illustration of the size of the ERBS scanner field of view from nadir to limb.

4.3 Construction Of The Constant Size Field Of View Data Set

Following the conventional ERBE classification for view zenith angle bins, a constant size field of view (CFOV) is constructed for each view zenith angle bin. CFOV is obtained by averaging observations from contiguous fields of view at nadir so that the resulting observation has the same spatial scale as that for the field of view at a view zenith angle of 75°. To limit the size of the field of view, only six view zenith angle bins with 75° as the largest view zenith angle are used. Fig. 4.2 shows how the constant size fields of view were constructed. An appropriate number of nadir ERBE scanner fields of view were summed to form a single field of view, the size of which matched a single ERBE scanner field of view near the limb. Table 4.1 gives the number of ERBE scanner fields of view in both scanning direction and satellite track direction for each angular bin for the summation. Also listed are the differences of the field of view sizes for the new observations. The differences vary by less than 15%.

Table 4.2 Number of ERBE scanner fields of view for each bin used to form constant size fields of view.

Bin No.	View zenith angle (degree)	No. of scan spots in average	No. of scan lines in average	Percent difference in size of area
1	0.0 - 15.0	6	2	6.3%
2	15.0 - 27.0	5	2	-5.1%
3	27.0 - 39.0	4	2	7.5%
4	39.0 - 51.0	3	2	14.8%
5	51.0 - 63.0	2	1	-10.0%
6	63.0 - 75.0	1	1	0.0%

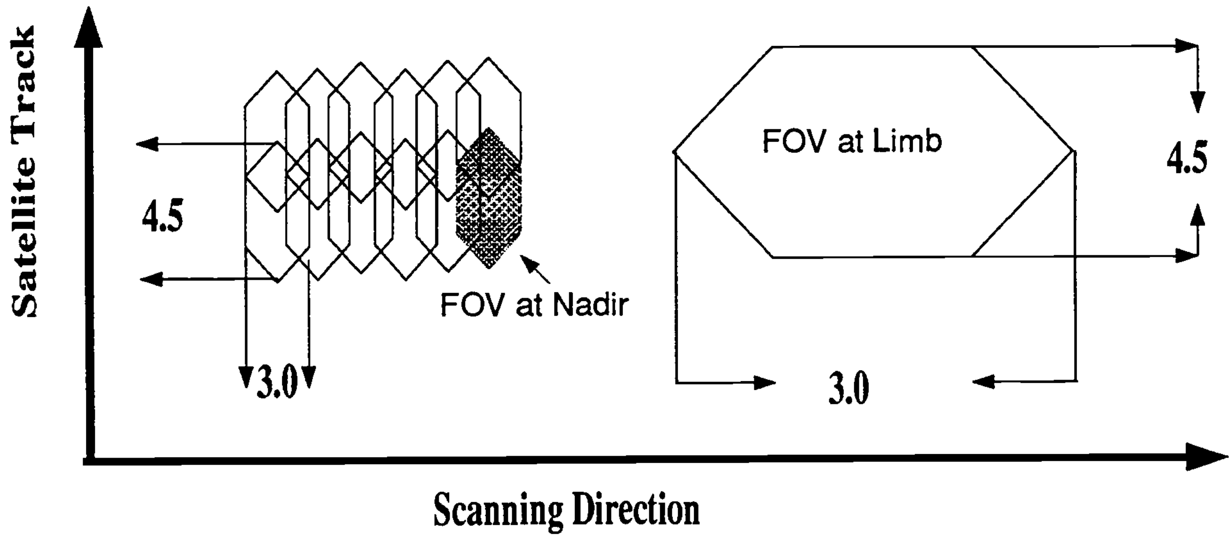

Figure 4.2 Construction of constant size field of view.

Because the degree of anisotropy depends on the scene type being viewed, an appropriate scene type must be assigned for the constant size field of view observations. The scene for each ERBS pixel was identified by the ERBE MLE method as one of twelve scene types. In order to avoid complications due to surface heterogeneity, constant size fields of view were constructed only for those pixels whose fields of view had homogeneous geographic scene types: ocean, land, desert, ice/snow. The cloud amount in constant size fields of view was taken to be a weighted average cloud cover given by

$$\mathrm{AMT} = \frac{A_{\mathrm{CLR}}N_{\mathrm{CLR}} + A_{\mathrm{PC}}N_{\mathrm{PC}} + A_{\mathrm{MC}}N_{\mathrm{MC}} + A_{\mathrm{OV}}N_{\mathrm{OV}}}{N_{\mathrm{TOTAL}}} \tag{4.1}$$

where N_{CLR}, N_{PC}, N_{MC} and N_{OV} are the number of clear, partly cloudy, mostly cloudy and overcast ERBS pixels in the constant size field of view. N_{TOTAL} is the total number of ERBS pixels. The weighting factors, A_{CLR} , A_{PC} , A_{MC} , A_{OV}, are the mean cloud cover fractions for the four cloud categories used in the ERBE ADMs. Table 4.3 gives the values of the weighting factors and the criteria used to determine the cloud type for

Table 4.3. Criteria for determining cloud scene types of the constant size field of view observations.

Cloud scene type	Criteria for cloud scene types	Weighting factor for each cloud scene, A
Clear	0 - 5%	2.5%
Partly cloudy	5 - 50%	27.5%
Mostly cloudy	50 -95%	77.5%
Overcast	95 - 100%	97.5%

the constant size field of view. For example, when the fractional cloud amount of the constant size field of view is less than 5%, the cloud scene type is assigned as clear.

4.4 Independent Samples

Because of the varying degree of cloud cover allowed within each scene type, the standard deviation of the anisotropy associated with a particular sun-earth-view geometry and scene type is large. Fig. 4.3 shows examples of the standard deviations of the ERBE ADMs expressed as a percent of the anisotropic factor for the solar zenith angle bin (36.9° – 45.6°) in polar coordinates. Regions for which the standard deviations are greater than 30% are crosshatched. Clearly, the variability of the ADMs is quite large. For most angular bins the variability is greater than 20%. Partly and mostly cloudy scenes, because of the large ranges of cloud fractions involved, have larger variabilities than do clear and overcast scenes. In order to determine the significance of the differences in the anisotropy between full resolution observations and constant size field of view observations, the "noise" caused by the variability and the finite observing period must be estimated. The noise is defined as

$$\text{noise} = \frac{\sigma}{\sqrt{\text{n}}} \tag{4.2}$$

where σ is the standard deviation of observations and n is the number of statistically independent observations.

Generally, for two independent normal distributions with means μ_1 and μ_2, standard deviations σ_1, σ_2 and sample sizes n_1, n_2, the significance of the difference between the two means is determined by the test statistic (Brownlee, 1965):

$$\frac{\mu_1 - \mu_2}{\sqrt{\frac{\sigma_1^2}{n_1} + \frac{\sigma_2^2}{n_2}}} \; . \qquad (4.3)$$

For the two–sided *t* test at the 90% confidence level, the critical region is

$$\mu_1 - \mu_2 < u_{\frac{\alpha}{2}}\sqrt{\frac{\sigma_1^2}{n_1} + \frac{\sigma_2^2}{n_2}} \text{ and } \mu_1 - \mu_2 > u_{1-\frac{\alpha}{2}}\sqrt{\frac{\sigma_1^2}{n_1} + \frac{\sigma_2^2}{n_2}} \qquad (4.4)$$

where $u_{0.95} = 1.64$. But, in calculating the variance of the mean as σ^2/n, the observations in each distribution are assumed to be independent.

It has been shown that radiation fields are spatially correlated on a scale of 1000 ~ 2000 km (Cahalan et al., 1982). Using the ERBS scanner measurements, Payette (1989) presented a comprehensive study of the spatial correlation properties of the ERBS scanner data. The results showed that the successive along- or across-track shortwave and longwave radiance measurements were highly correlated. A complete decorrelation was obtained for measurements separated by approximately 2000 km. Fig. 4.4 gives an example of the spatial autocorrelation coefficients as a function of number of scan lines for shortwave and longwave radiance measurements. The coefficients are for the consecutive ERBS nadir observations with an overhead sun for September, 1986. For measurements separated by a distance d, the autocorrelation coefficient is defined as

$$\rho(d) = \frac{\mathrm{cov}(0, d)}{\sigma(0)\sigma(d)} \qquad (4.5)$$

where σ is the standard deviation and cov(0, d) is the covariance. ρ has values varying from –1 to 1. If measurements are independent, ρ equals zero. Fig. 4.4 shows that for a distance of less than about 40 scan lines, which is approximately equivalent to 2000 km, the observations are highly correlated. Such observations are likely to come from the same weather system. In the development of the ERBE ADMs, all available measurements obtained by the Nimbus–7 ERB scanning radiometers were sorted into the angular bins defined in the Tables 3.2 and 3.3. Following this method, the ERBS observations for September, October and November, 1986 were sorted into angular bins to develop the ADMs. One mean value for each angular bin (hereafter referred to as the bin-average method) was obtained based on the highly correlated ERBS observations.

Generating independent samples from correlated observations is known as prewhitening. Though there are many prewhitening techniques, because of the huge volume of ERBS observations, the method used to prewhiten the observations should be simple, efficient and provide a high degree of independence. A simple technique was described by Baldwin and Coakley (1991) (hereafter referred to as the BC method). They found that estimates obtained by averaging observations over 40 consecutive scan lines were sufficiently independent for a particular sun-target-satellite geometry.

The Mean Square Successive Difference Test (MSSDT) was used in this thesis to test the hypothesis of randomness (Brownlee, 1965). Given a sequence of observations $x_1, ..., x_n$ from a population N(μ, σ^2), there are two ways to estimate the true variance σ^2. The first is the unbiased estimator

$$s^2 = \frac{1}{n-1} \sum_{i=1}^{n} (x_i - \bar{x})^2 \tag{4.6}$$

and, the second is

$$d^2 = \frac{1}{n} \sum_{i=1}^{n-1} (x_{i+1} - x_i)^2 \, . \tag{4.7}$$

It is easy to prove that $E\left[d^2/2\right] = \sigma^2$. Usually consecutive observations tend to be correlated positively with their predecessors (Fig. 4.4) so that successive differences $x_{i+1} - x_i$ tend to be smaller than they would be under the null hypothesis that the observations are independent. Thus, the expected value of $d^2/2$ is less than that of s^2. The randomness test is based on the test statistic

$$\frac{\frac{d^2/2}{s^2} - 1}{\sqrt{(n-2)(n^2-1)}} \tag{4.8}$$

which is distributed as a unit normal deviate under the null hypothesis.

Nearest neighbor correlations were used to test whether the samples obtained with the BC method were independent. For the majority of angular bins the samples were highly correlated at the 90% confidence level. In this study, such correlations were avoided by skipping every other set of 40 scan lines. This procedure will be referred to as the modified Baldwin-Coakley (MBC) method. Fig. 4.5 presents the results of the randomness test for the samples obtained using the BC and MBC method based on the ERBS shortwave radiance measurements for September, 1986. In the figure, the percentage of angular bins found to contain independent samples is plotted as a function of view zenith angle for an overhead sun. The hatched bars are for the BC method, and the blank bars are for the MBC method. About 60% of the angular bins contained correlated estimates using the BC method. This percentage was reduced to about 15% using the MBC method.

The effect of spatial correlation was clearly shown in comparisons of the estimates obtained by applying the bin-average method, the BC method and MBC method. Observations for the comparison were taken from ERBS shortwave scanner data for September, October, November, 1986. Fig. 4.6 gives the results for the means and sample noise given by (4.2). The figure shows the azimuthally averaged result for ocean scenes at all solar zenith and viewing zenith angles. The differences of the estimated means for the three methods are small. They are about 3.3% for clear sky, about 2.5% for partly cloudy, about 5.4% for mostly cloudy and about 6.3% for overcast.

Measurements used in the bin-average method were most likely obtained from the same weather system. The variation of samples was expected to be small. By contrast, measurements used in the MBC method were highly independent of each other. Thus, a large variation in the samples was expected. The "noise" level was used to describe the variation of samples which was caused by the variability of cloud amount within each scene type combined with the finite observing period. As shown in Fig. 4.6, the estimated "noise" level from the samples obtained using the MBC method increased by a factor of 10 or more above those obtained using the bin-average method. For example, in the case of clear sky, the "noise" level for the bin-average samples was about 0.065 $Wm^{-2}sr^{-1}$ but increased to about 0.217 $Wm^{-2}sr^{-1}$ for the BC samples and about 0.286 $Wm^{-2}sr^{-1}$ for the MBC method. When the "noise" level is underestimated, using (4.4) the inference that the two means differ significantly will often be erroneous.

In this study, independent samples will be obtained using the MBC method. The method will be used to construct angular dependence models for both ERBS full resolution observations and constant size field of view observations.

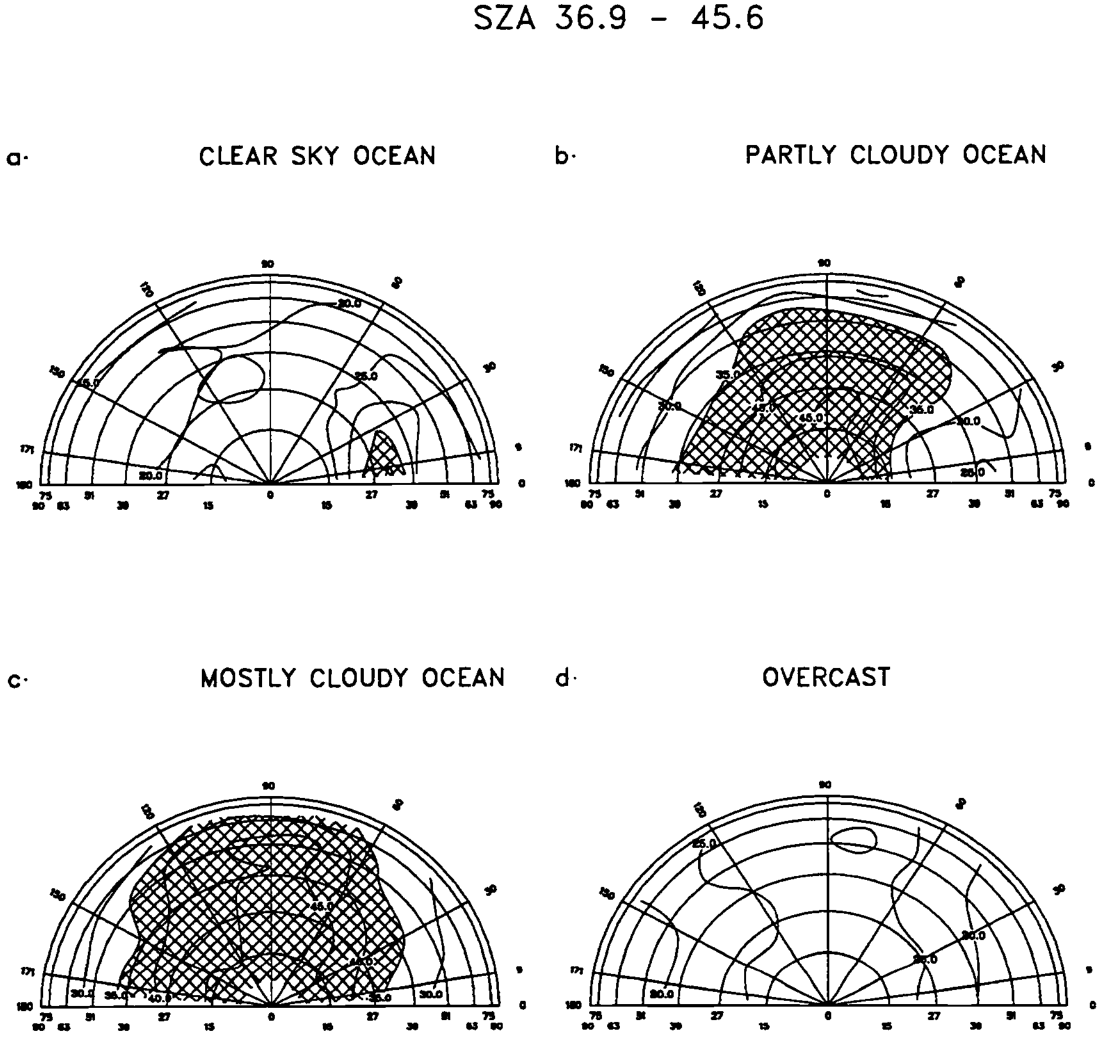

SZA 36.9 - 45.6

a· CLEAR SKY OCEAN

b· PARTLY CLOUDY OCEAN

c· MOSTLY CLOUDY OCEAN

d· OVERCAST

Figure 4.3 Examples of the standard deviations for the ERBE ADMs expressed as a percent of the anisotropic factor. The view zenith angle increases in the radial direction. The relative azimuth angle increases counterclockwise in the polar direction. The increment of contours is 5%. Regions for which the standard deviations are greater than 30% are crosshatched.

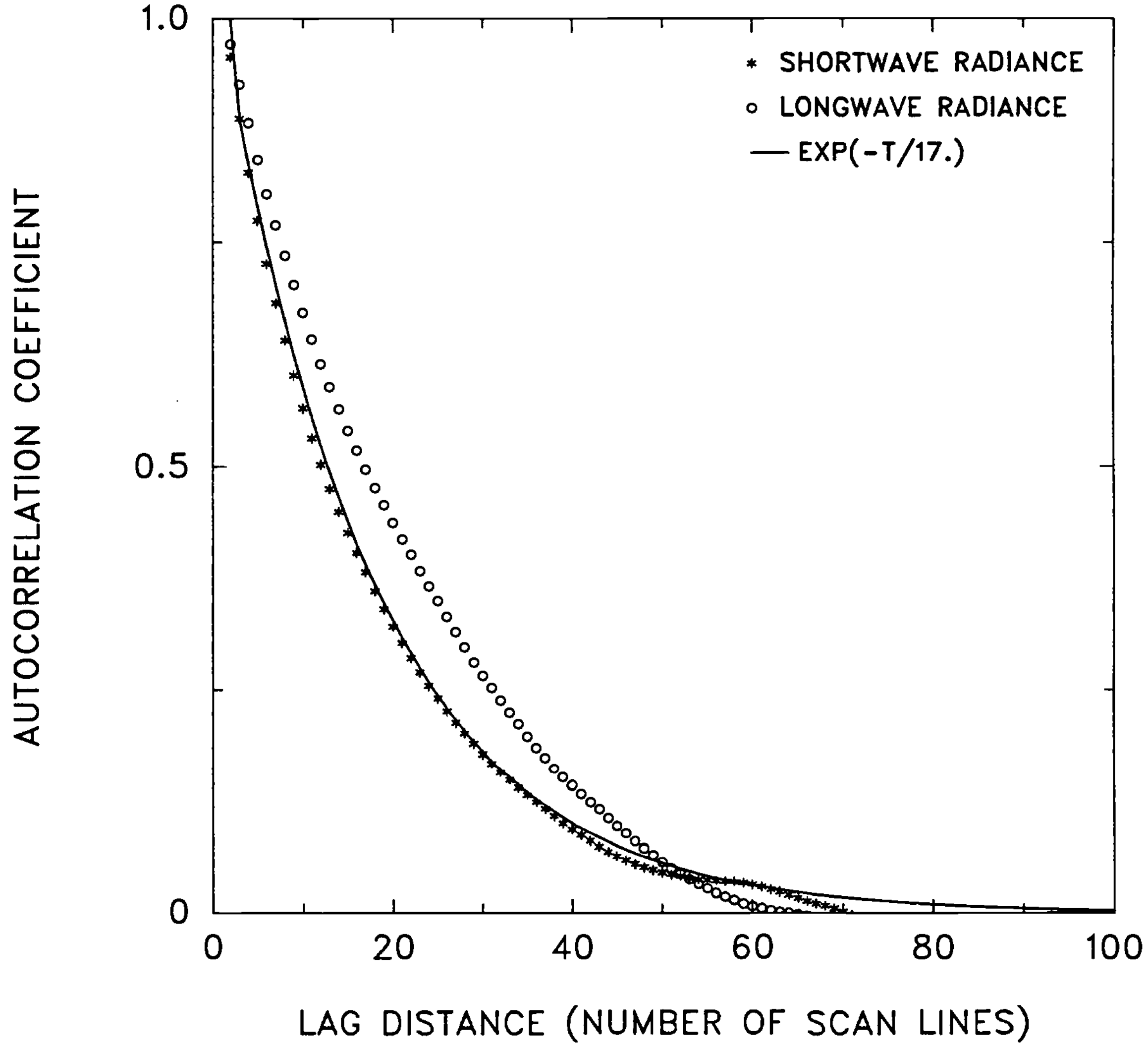

Figure 4.4 Spatial autocorrelation coefficients as a function of number of scan lines for shortwave (stars) and longwave (circles) radiances. The calculation was based on consecutive ERBS nadir observations with an overhead sun for September, 1986.

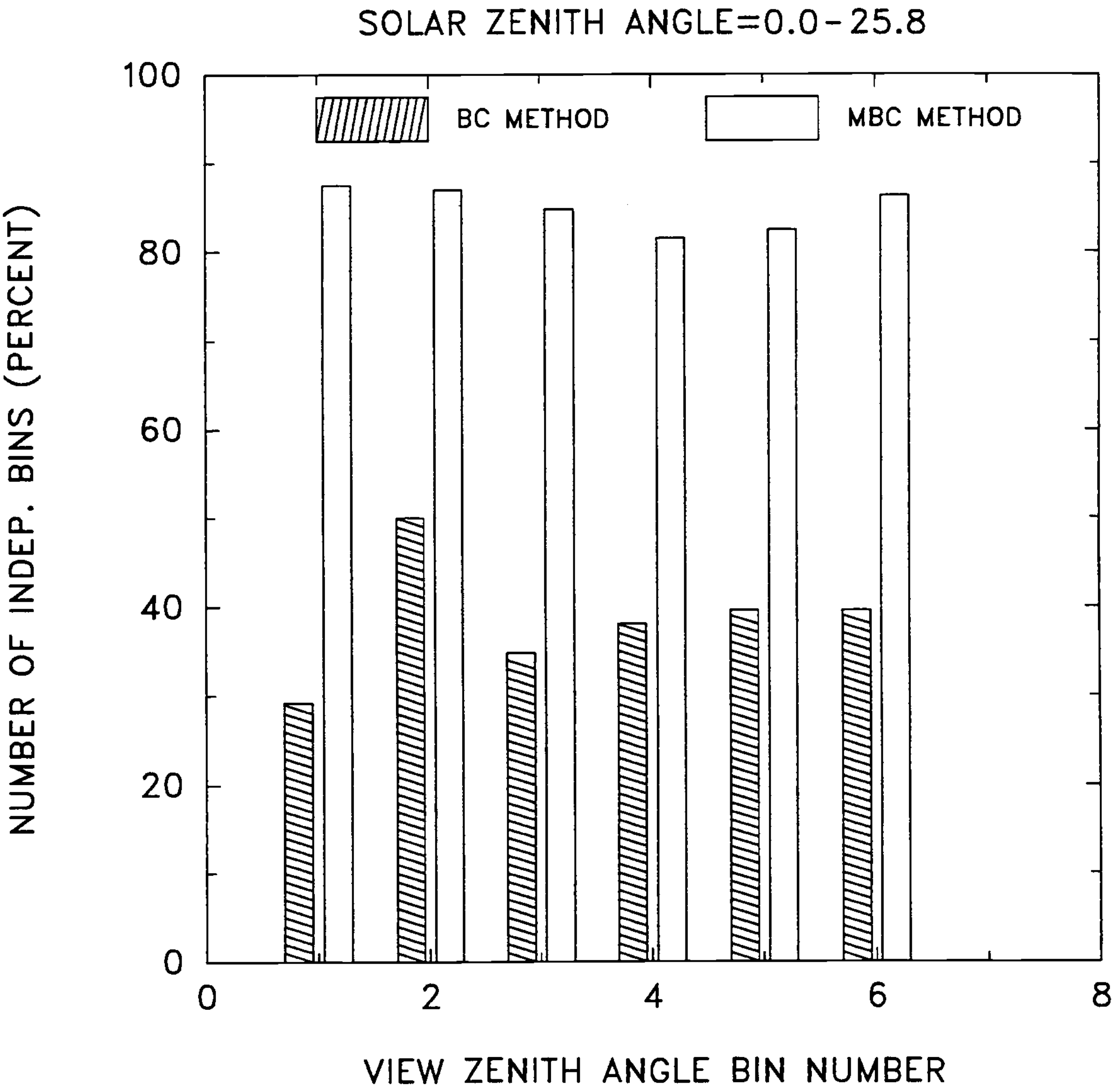

Figure 4.5 Percentage of angular bins containing independent samples using the BC and MBC methods. The percentages are based on the Mean Square Successive Difference Test. The hatched bars are for the BC method, and the blank bars are for the MBC method. The results are for ERBS shortwave radiances for overhead sun for September, 1986.

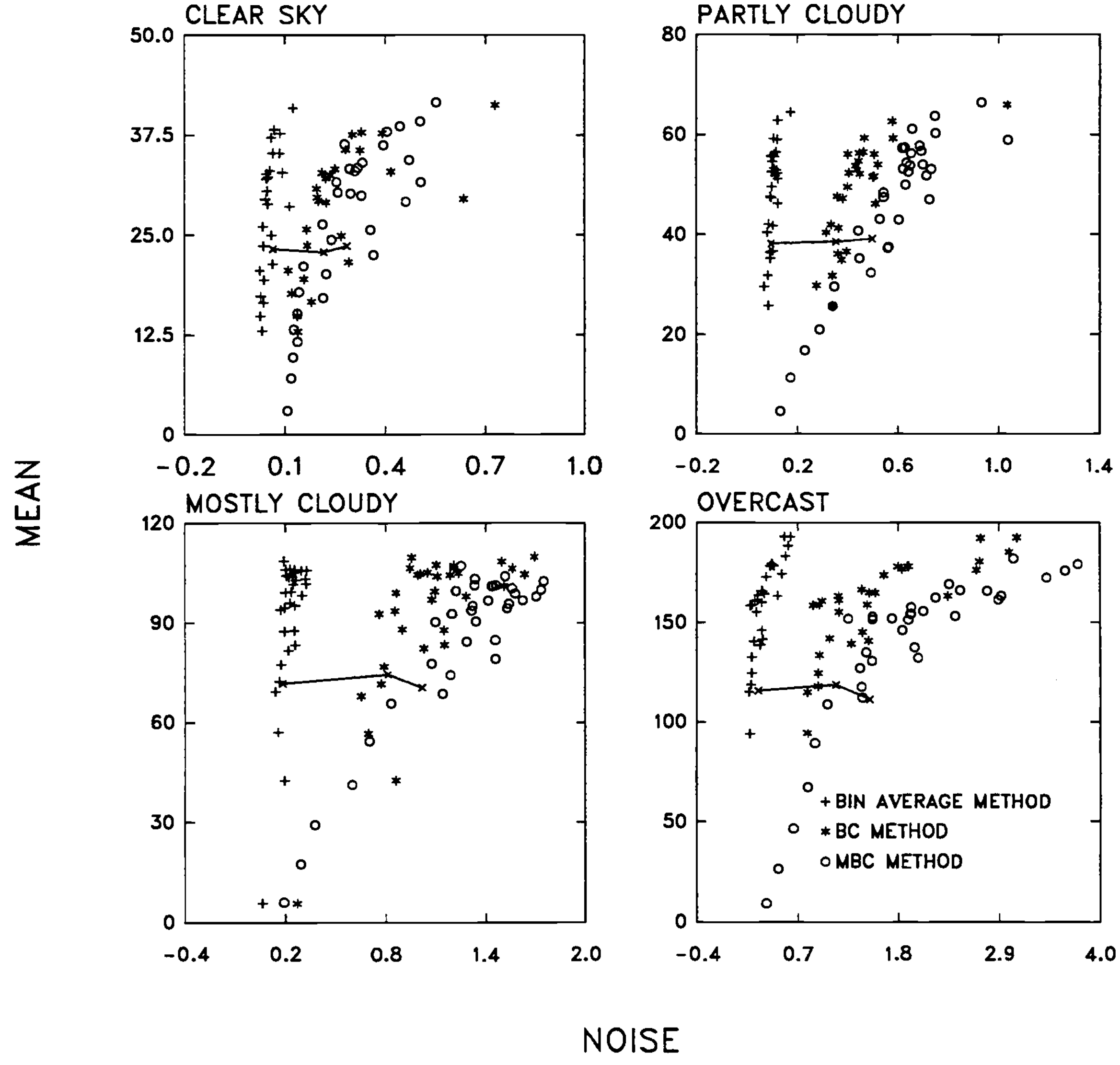

Figure 4.6 Comparison of the estimated means and noise levels obtained using the bin-average method, the BC method and MBC method. The means and noise levels are plotted in units of $Wm^{-2}sr^{-1}$. The results are for ERBS shortwave radiances for overhead sun for September, 1986.

4.5 Pseudo-Angular Dependence Models

Because of the ERBS orbit and the cutoff in satellite view zenith angle used here in the construction of constant size field of view observations, approximately 25% of the sun-earth-satellite angular bins have either no observations or too few observations for the purpose of constructing ADMs. Following Baldwin and Coakley (1991), a pseudo-angular dependence model is defined based on (3.13). The pseudo model is given by

$$P(\mu_{oi},\mu_j,\phi_k) = \frac{\pi I(\mu_{oi},\mu_j,\phi_k)}{\sum\limits_{m,n} \omega_{mn} I(\mu_i,\mu_m,\phi_n)} \tag{4.9}$$

where $\mu_{0\mathrm{i}}$ is the cosine of the solar zenith angle and is associated with solar zenith angle bin i, μ_j is the cosine of view zenith angle and is associated with view zenith angle bin j, ϕ_k is the azimuthal angle and is associated with azimuthal angle bin k. The quadrature weights $\omega_{mn} = 2\mu_m \Delta\mu_m \Delta\phi_n$ and $\Delta\mu_m = \sin^2\theta_{m+1} - \sin^2\theta_m$. The pseudo-angular dependence model is restricted to be normalized over only those angular bins for which a minimum number of observations were obtained. In this investigation the minimum number was set to be eight. The percent difference between pseudo-angular dependence models derived from the full resolution observations (hereafter referred to as FFOV model) and that derived from constant size field of view observations (hereafter referred to as CFOV model) is defined as:

$$\Delta P(\mu_{oi},\mu_j,\phi_k)(\%) = 100 \times \frac{P^{FFOV}(\mu_{oi},\mu_j,\phi_k) - P^{CFOV}(\mu_{oi},\mu_j,\phi_k)}{\frac{1}{2}\{P^{FFOV}(\mu_{oi},\mu_j,\phi_k) + P^{CFOV}(\mu_{oi},\mu_j,\phi_k)\}} . \tag{4.10}$$

4.6 Results

Figs. 4.7 and 4.8 show examples of the differences in anisotropy between full resolution ERBE scanner and constant size field of view observations for clear, partly cloudy, mostly cloudy ocean, and overcast scenes. Fig. 4.7 gives the percent differences

(FFOV model — CFOV model) for the solar zenith angle bins which have the largest domains for which the differences are significant. Fig. 4.8 gives the same as Fig. 4.7 but for solar zenith angle bins which have the smallest domains having significant differences. The increment of the contours in the figures is 2.5%. Shaded regions indicate that the differences are significant at the 90% confidence level.

Results from 40 models (clear ocean, partly cloudy ocean, mostly cloudy ocean and overcast scenes over ten solar zenith angle bins) indicate that: 1) significant and systematic differences exist between angular dependence models derived from full resolution observations and those derived from constant size field of view observations for all scene types; 2) the bins which have significant differences at the 90% confidence level are 28% for clear, 42% for partly cloudy and 18% for mostly cloudy ocean scenes, and 21% for overcast scenes; 3) the differences are generally small. Differences in the pseudo-ADMs are less than 10% for clear and partly cloudy ocean, and less than 5% for mostly cloudy ocean and overcast scenes; 4) the differences increase with solar zenith angles. The largest differences usually occur in the direction of forward scattering.

An index of the effect of field of view size on anisotropy is the azimuthally averaged anisotropy defined by (3.19). Examples of the azimuthally averaged anisotropy (AAA) are given in Fig. 4.9. Only the angular bins for which there were significant differences in the anisotropy between the FFOV and CFOV models were used for the calculation. The anisotropic factors in the angular bins for which there were no significant differences in the anisotropy were set equal to zero. In the figure, the AAAs are the weighted averages for all solar zenith angle bins given by

$$\overline{AAA}(\mu_j) = \frac{\sum\limits_{i=1}^{10} AAA(\mu_{0i}, \mu_j)\mu_{0i}\Delta\mu_0}{\sum\limits_{i=1}^{10} \mu_{0i}\Delta\mu_0} \tag{4.11}$$

where the index i is for the ten solar zenith angle bins, $\Delta\mu_0 = 0.1$ and $\sum\limits_{i=1}^{10} \mu_{0i}\Delta\mu_0 = \frac{1}{2}$. It is clear that with increasing cloud cover the values of the AAAs approach unity while the degree of limb-brightening decreases. The CFOV models are generally more anisotropic than the FFOV models except for partly cloudy scenes. Differences between the two models are less than 10% as is shown in Fig. 4.10.

The degree of anisotropy (DA) defined by (3.18) for the FFOV and CFOV models are shown in Fig. 4.11. The angular bins for the calculation of the DA are restricted to those for which there are significant differences between the FFOV and CFOV models. Fig. 4.11 shows that the degree of anisotropy for both the FFOV and CFOV models grows with increasing solar zenith angle, and again, decreases with increasing cloudiness. Fig. 4.12 gives the differences of the DA between the FFOV and CFOV models. For cloud-free scenes, there are negative values for almost all solar zenith angle, which means that radiation reflected from constant size fields of view is more anisotropic than that reflected from the full resolution fields of view. As noted in section 4.1, because of scene identification errors combined with the effect of cloud clustering, CFOV observations are expected to be more anisotropic than FFOV observations. The result shown in Fig. 4.12 is consistent with expectations.

Fig. 4.13 shows the limb darkening obtained for emitted longwave radiances and Fig. 4.14 shows differences in the limb darkening for those angular bins that had significant differences in the anisotropy between the FFOV and CFOV models. Again for cloud-free regions, the constant size field of view observations are more anisotropic than are the full resolution observations.

Figs. 4.10, 4.12 and 4.14 show that overcast scenes are also more anisotropic for the constant size field of view observations than they are for the full resolution observations. This result counters expectations that the constant size field of view observations should be more isotropic for overcast scenes. If overcast scenes are correctly identified, then the degree of clear contamination is expected to be larger for small fields of view than it is for large fields of view. Consequently, the ADMs associated with small fields of view are expected to be more anisotropic than those for the large fields of view. The cause of the counter result is thought to be due to the ERBE MLE scene identification.

In summary, because there was a large variation of cloud optical properties over relatively small spatial and temporal scales, cloud scene identification based on coarse spatial resolution bispectral radiance pairs was likely to be prone to errors. Moreover, because clouds clustered on certain spatial scales and because the field of view of the scanner grew from nadir to limb, there was likely to be more cloud contamination in clear scenes at nadir than in clear scenes at the limb, provided the scene identification correctly identifies clear scenes at the limb. Since anisotropy is a function of scene type, due to the varying degree of cloud or clear contamination from nadir to limb, the anisotropy derived from the various scene types from the ERBE scanner was expected to be a function of spatial scale. In fact, for CFOV observations, clear scenes were expected to be more anisotropic than FFOV observations and conversely overcast scenes were expected to be more isotropic.

The CFOV observations were constructed based on ERBS scanner observations with the ERBE MLE scene identification. Comparing the anisotropy obtained using the CFOV observations with that obtained using the FFOV observations, there was indeed a spatial scale dependence of the anisotropy. For clear scenes, the results were observed to be consistent with expectations, i.e., the CFOV observations were more anisotropic than the FFOV observations. For overcast scenes, however, the CFOV observations were not more isotropic than the FFOV observations. This result counters the anticipated effects of cloud clustering and scene identification errors. Gross errors in the ERBE MLE scene identification are thought to be the cause.

The differences between the FFOV and CFOV models were small, i.e., less than 10% for clear and partly cloudy ocean scenes, and less than 5% for mostly cloudy ocean and overcast scenes. Taking the average difference as 3%, this led to a 3%, or 341 $\mathrm{Wm^{-2}} \times 3\% = 10\ \mathrm{Wm^{-2}}$ as the typical difference in the estimated flux based on (3.1).

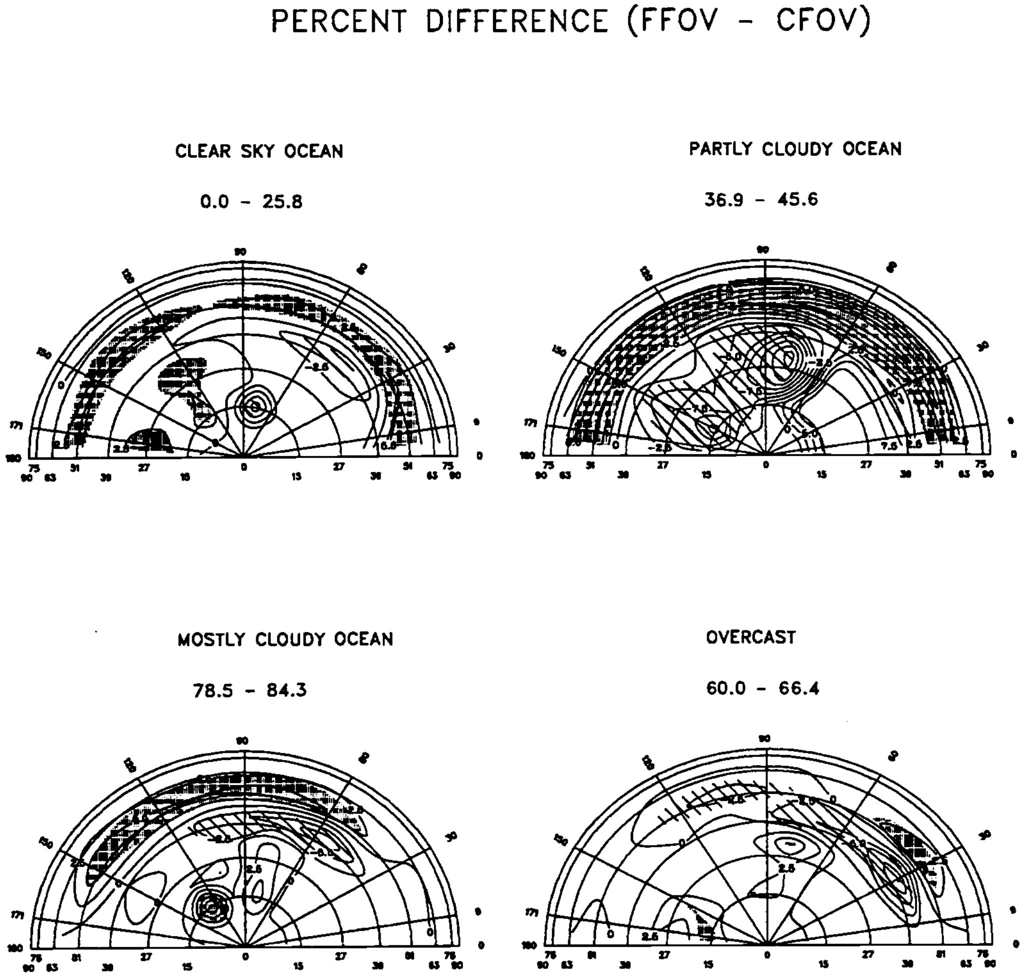

PERCENT DIFFERENCE (FFOV - CFOV)

CLEAR SKY OCEAN

0.0 - 25.8

PARTLY CLOUDY OCEAN

36.9 - 45.6

MOSTLY CLOUDY OCEAN

78.5 - 84.3

OVERCAST

60.0 - 66.4

Figure 4.7 Percent difference between the FFOV and the CFOV pseudo-angular dependence models for the solar zenith angle bins which have the largest domains for which the differences are significant. The solar zenith angles for each scene type are given in the figure. The radial axis is for view zenith angle, and the polar axis is for the relative azimuth angle. The increment of contours is 2.5%. Regions in which the differences are positive and significant at the 90% confidence level are shaded, and those that are negative and significant are hatched.

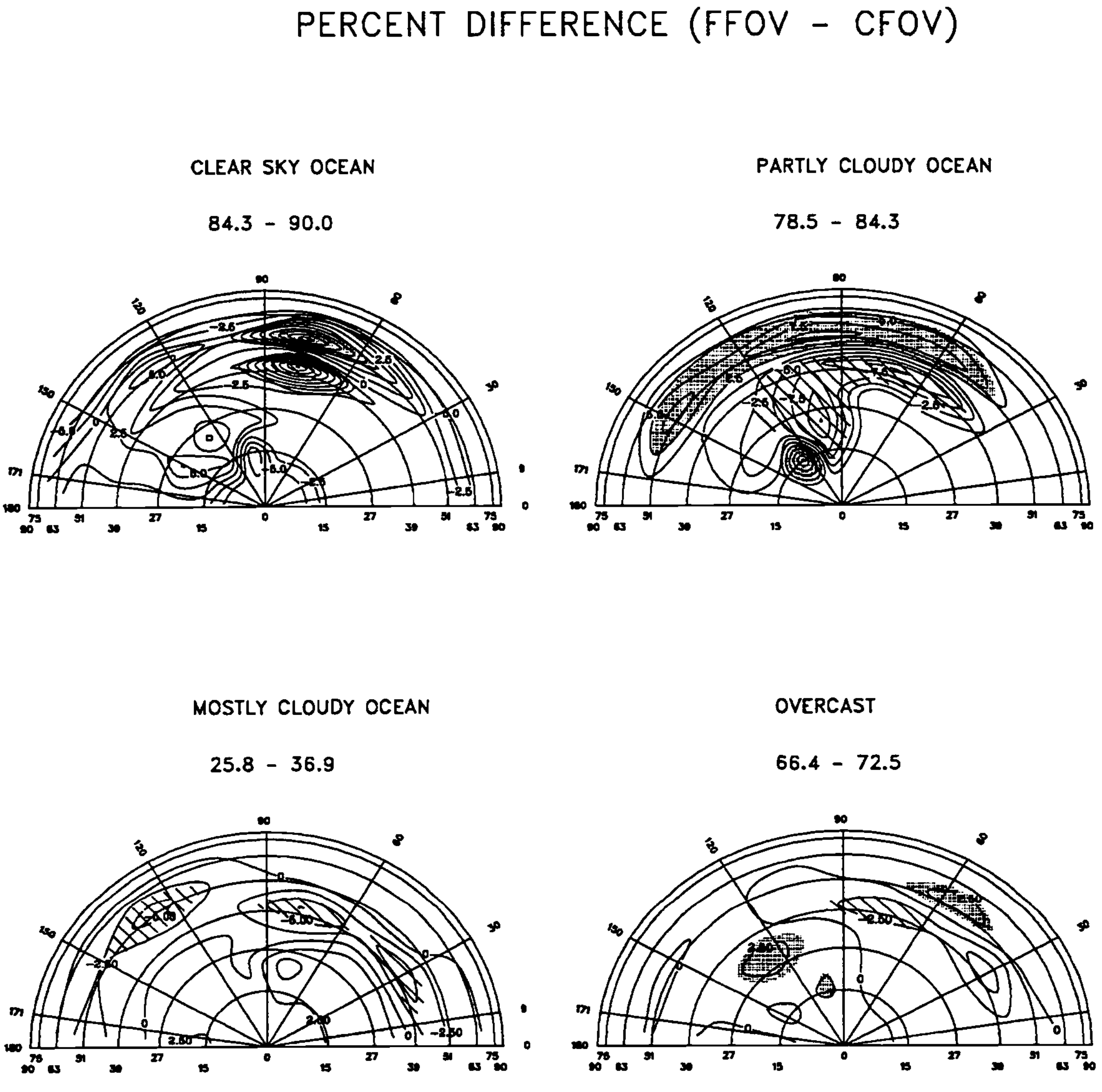

Figure 4.8 Same as Fig. 4.7 but for the solar zenith angle bins which have the smallest domains for which the differences are significant.

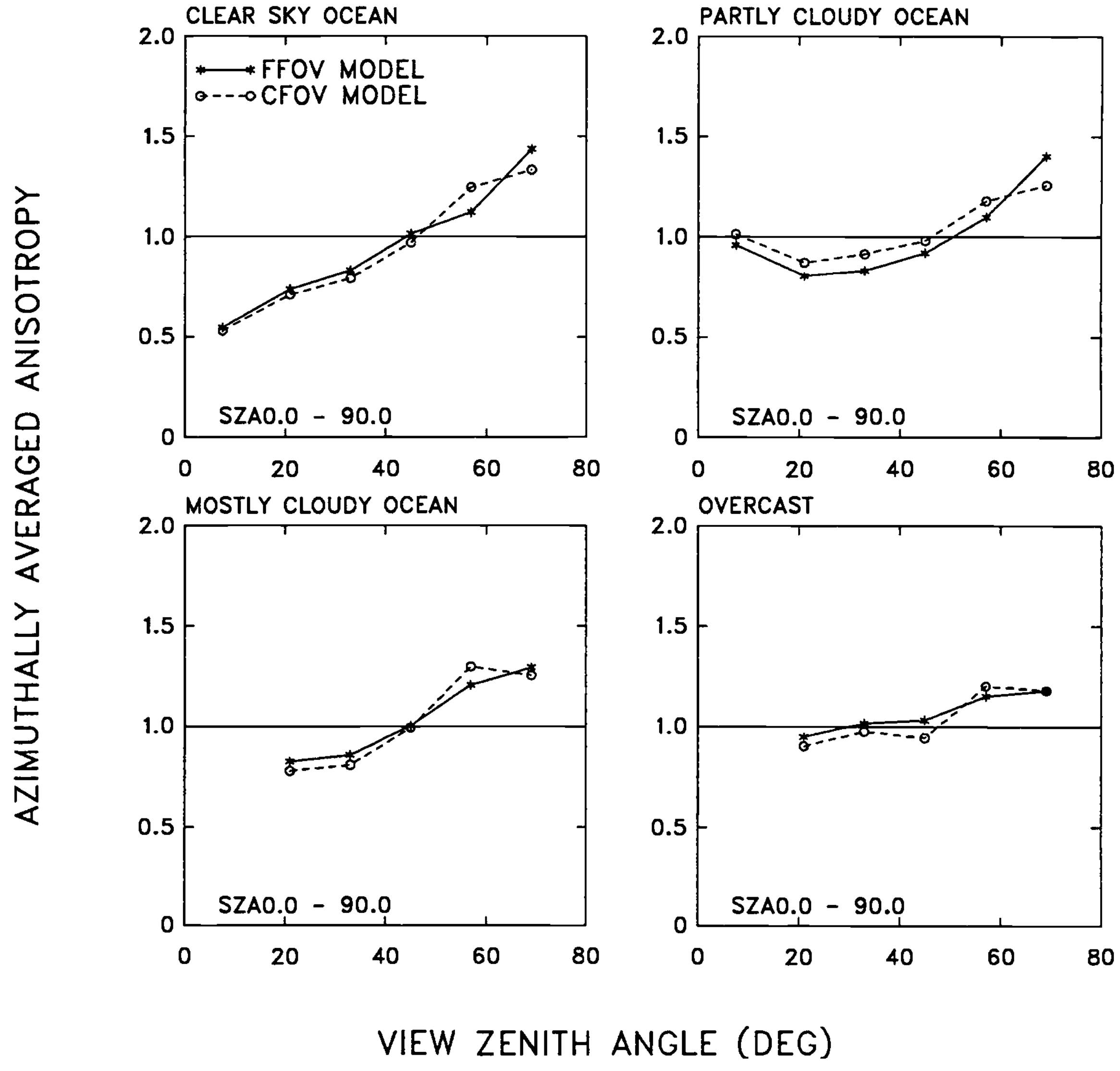

Figure 4.9 Azimuthally averaged anisotropy averaged over all solar zenith angles based on the angular bins which had significant differences between the FFOV and CFOV models (shortwave observations).

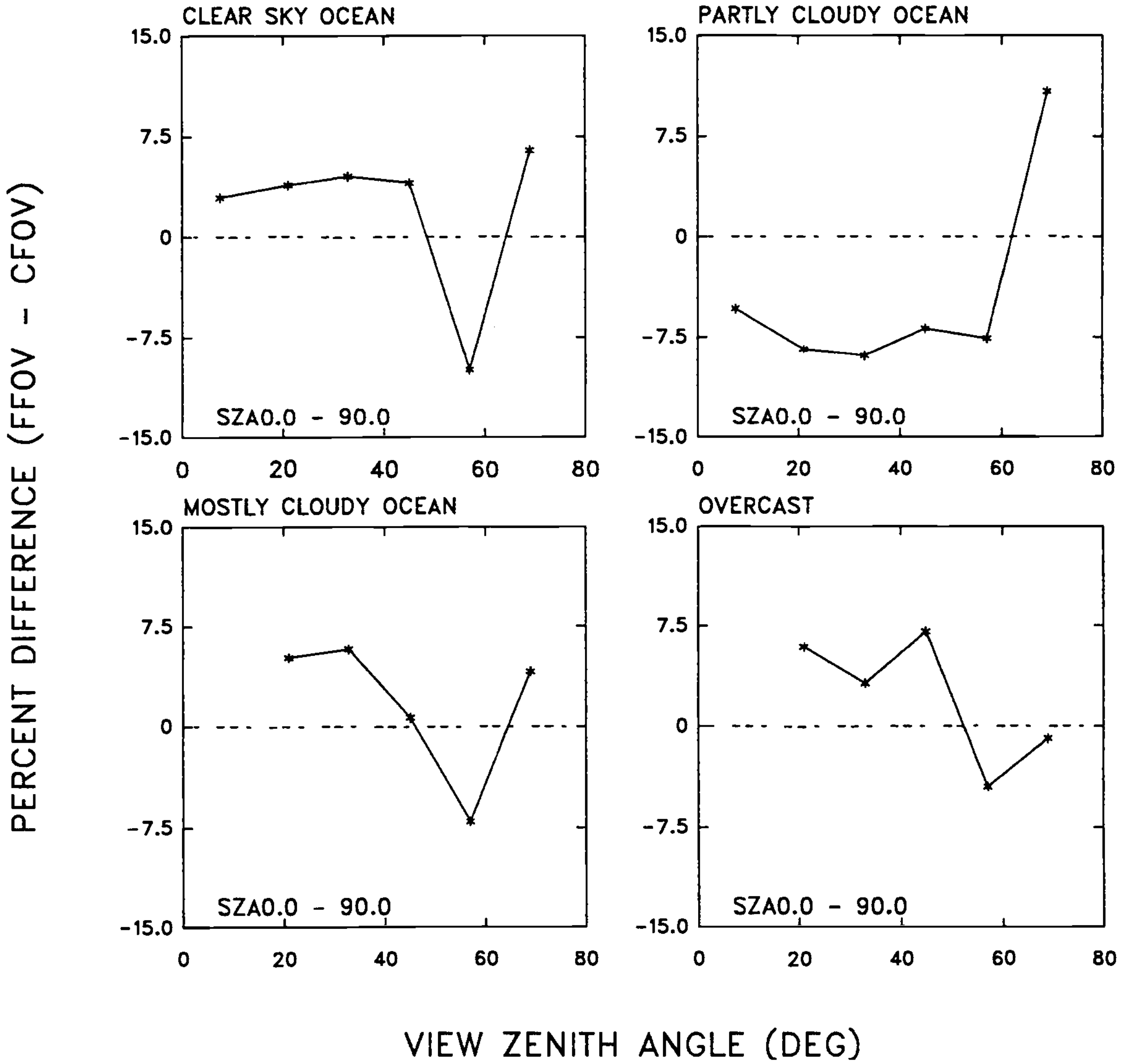

Figure 4.10 Percent differences of the azimuthally averaged anisotropy averaged over all solar zenith angles based on the angular bins which had significant differences between the FFOV and CFOV models (shortwave observations).

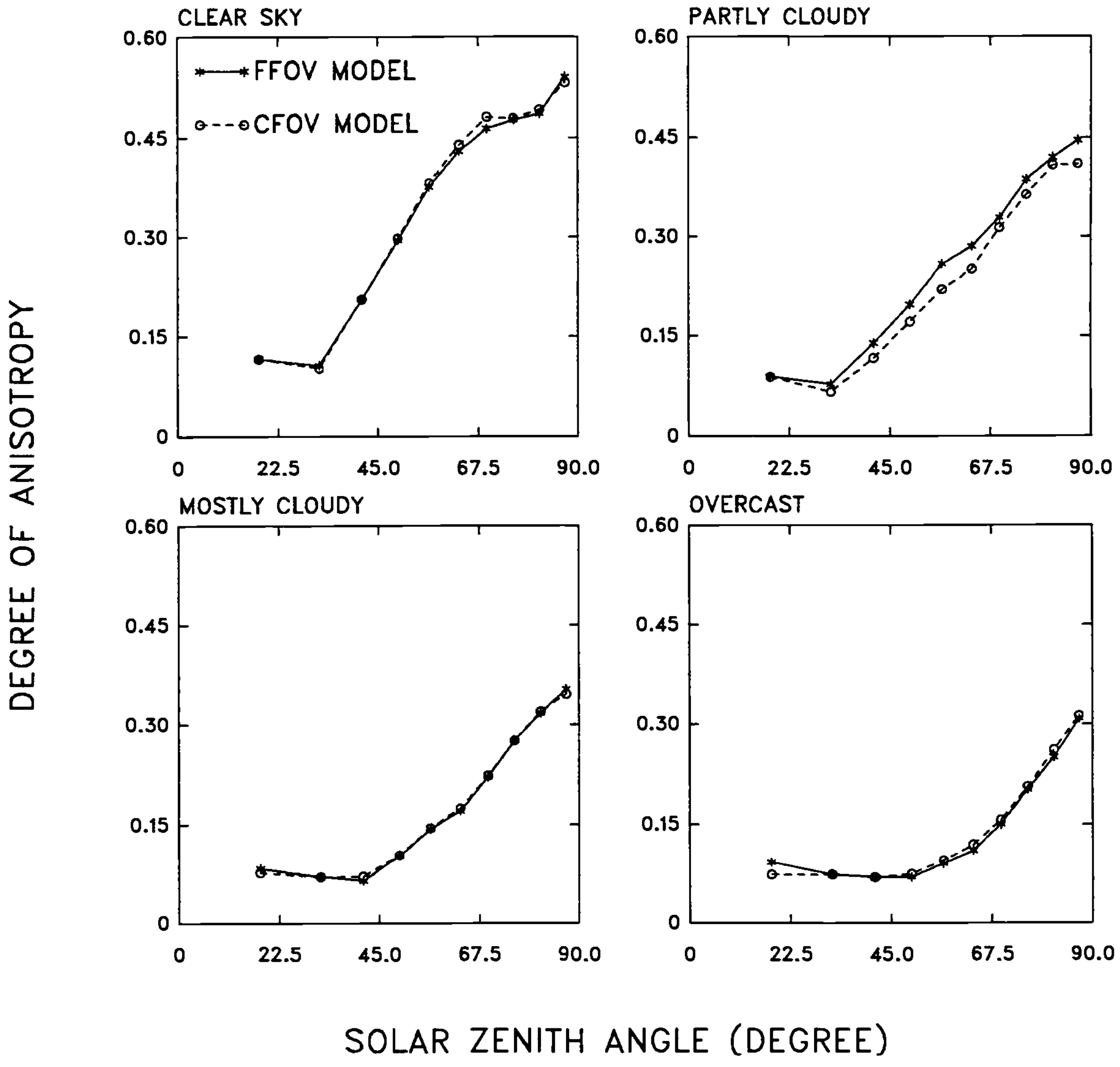

Figure 4.11 Degree of anisotropy as defined by (3.18) for the FFOV and CFOV Models calculated from the angular bins which had significant differences (shortwave observations).

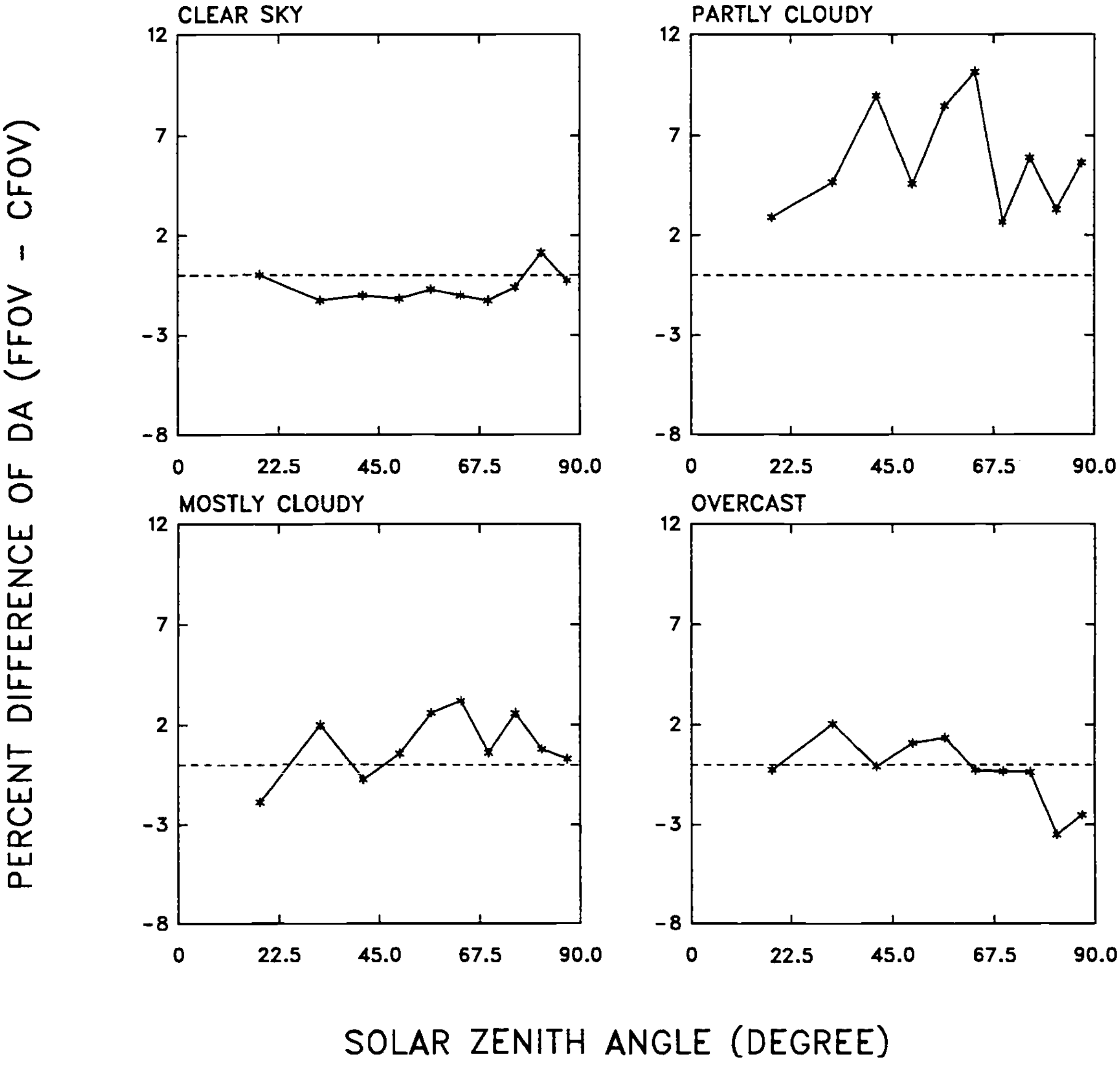

Figure 4.12 Percent differences in the degree of anisotropy between the FFOV and CFOV models for the angular bins which had significant differences (shortwave observations).

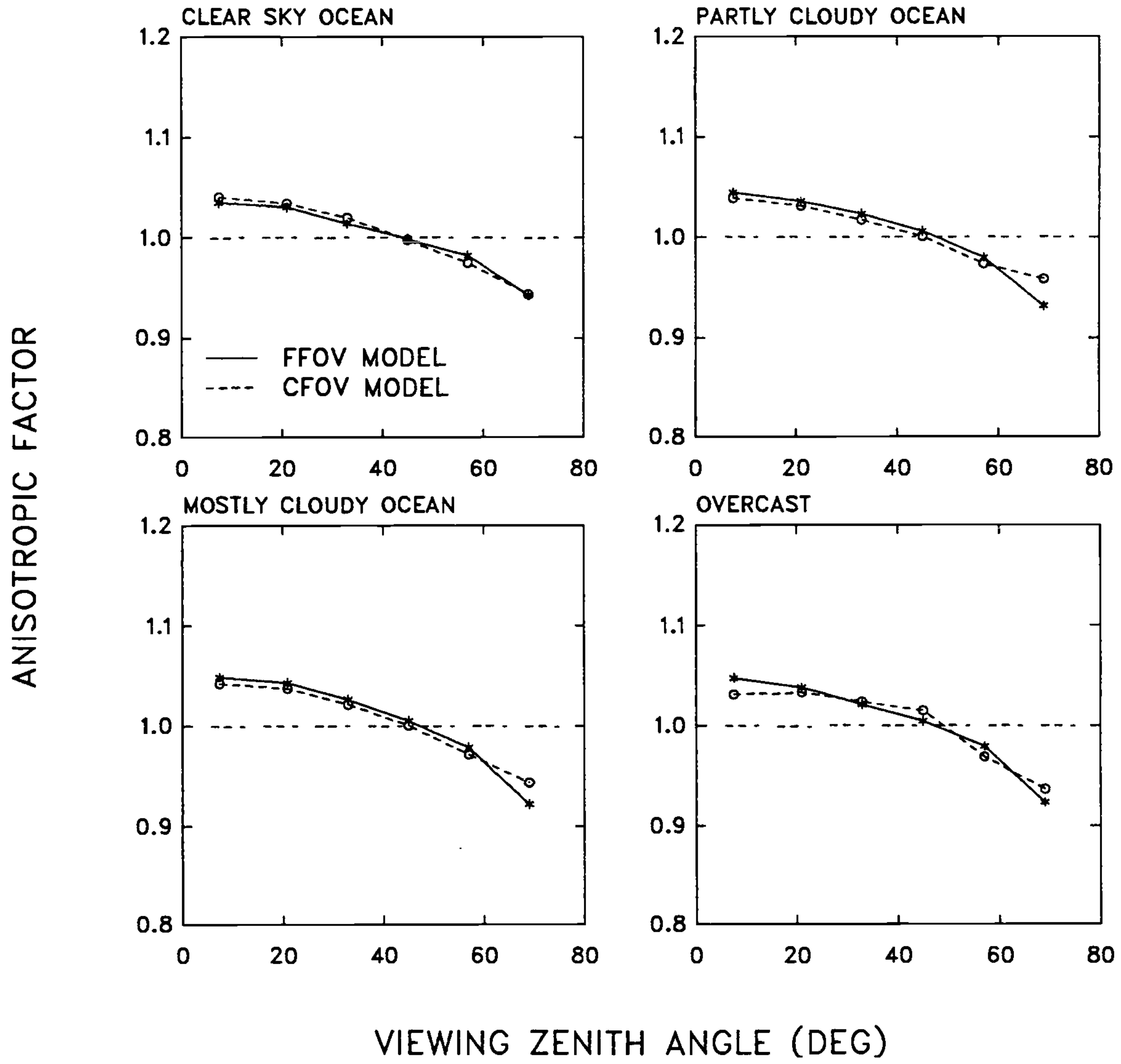

Figure 4.13 Azimuthally averaged anisotropy averaged over all latitudes for the angular bins which had significant differences between the FFOV and CFOV models (longwave observations).

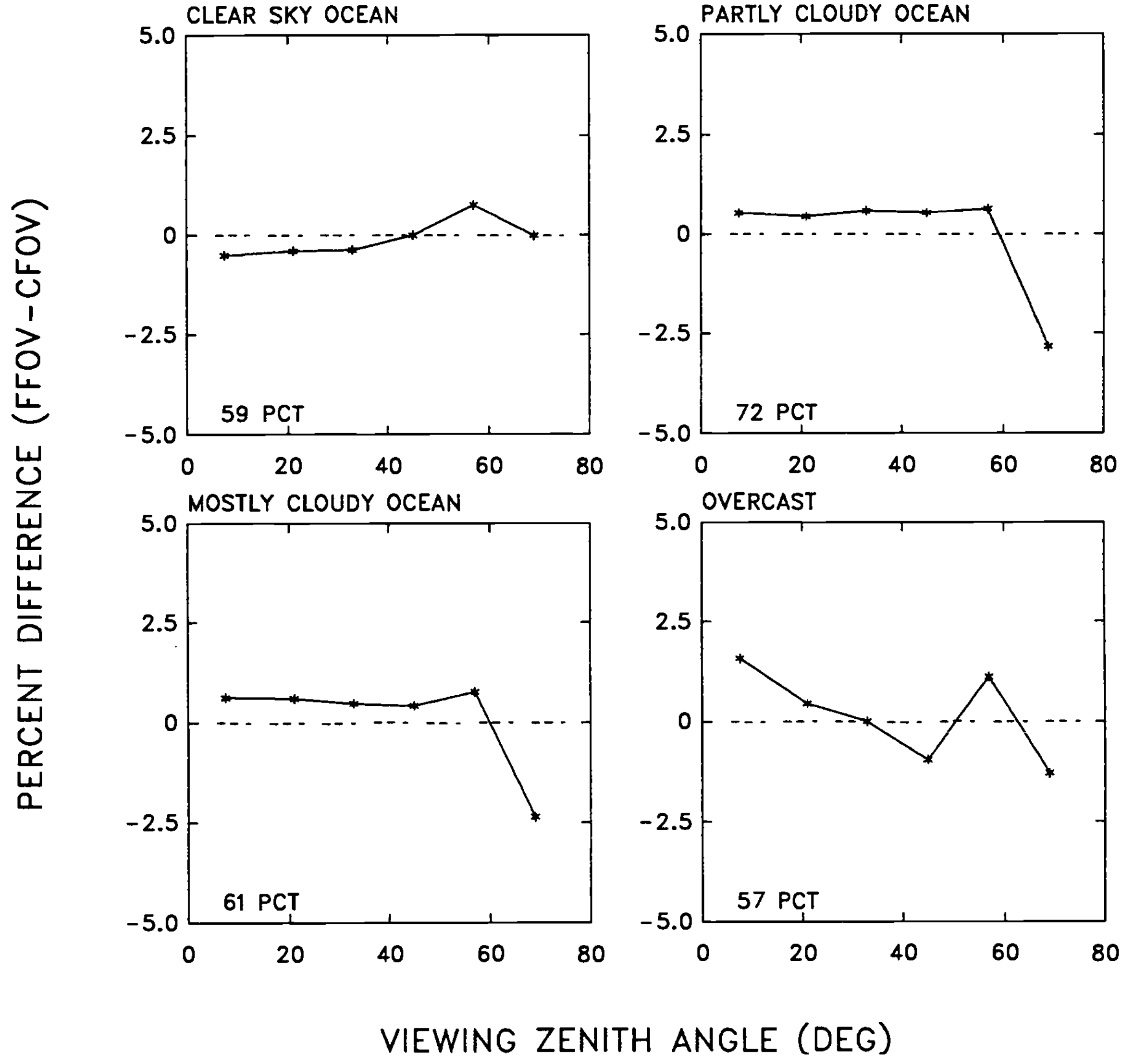

Figure 4.14 Percent differences in the azimuthally averaged anisotropy averaged over all latitudes for the angular bins which had significant differences between the FFOV and CFOV models (longwave observations). The percentages of the angular bins found to be significant were 59% for clear ocean, 72% for partly cloudy ocean, 61% for mostly cloudy ocean, and 57% for overcast scenes.

5. AN APPROACH FOR THE DEVELOPMENT OF INSTRUMENT INDEPENDENT ANGULAR DEPENDENCE MODELS

5.1 Introduction

Because of the large variation of cloud optical properties over relatively small spatial and temporal scales (Wielicki and Parker, 1992), it is impossible to obtain correct scene identification based on coarse resolution bispectral radiance pairs. The ERBE observations are subject to scene identification errors. Because of the nonlinear relationship between shortwave and longwave radiances, the scene identification errors are sensitive to instrument spatial resolution (Baldwin and Coakley, 1991). Scanner field of view size increases from nadir to limb. As a result, the scene identification errors will be a function of satellite zenith angle. The vertical development of clouds is another contributing factor which could cause scene identification errors. For broken clouds, the vertical extent is roughly comparable to their horizontal dimension. Radiances observed by a scanner are due to radiation reflected and emitted by both cloud tops and sides. It is impossible for scanning instruments to distinguish radiation reflected or emitted by cloud sides from that reflected or emitted by cloud tops. With increasing view angle, the contribution from cloud sides increase. Consequently, the fractional cloud cover for a scene at the limb appears to be larger than that of the same scene at nadir. The effect of cloud sides could lead to cloud scene identifications at nadir that are inconsistent with those obtained at the limb.

Clouds tend to cluster. The clustering of clouds combined with the growth of scanner field of view size from nadir to limb and scene identification errors leads to a varying degree of cloud or clear contamination from nadir to limb. The comparison between the anisotropy derived from the observations which have a constant size field of view (CFOV) and that obtained by using the full-resolution (FFOV) data demonstrates that this varying degree of cloud or clear contamination could cause the dependence of observed anisotropy on the instrument spatial resolution.

CFOV observations have larger field of view size than do FFOV observations. Because of cloud clustering, CFOV observations are expected to be less cloud (clear) contaminated than the FFOV data set, provided the scene identification correctly identifies clear (overcast) scenes. Since the degree of anisotropy decreases with increasing fractional cloud cover, the ADMs constructed using the CFOV data set are expected to be more anisotropic for clear scenes but more isotropic for overcast scenes than those obtained using the FFOV data set. Results obtained in chapter 4 showed that based on the ERBE MLE scene identification, the enhanced anisotropy appeared for CFOV clear ocean scenes. The overcast scenes, however, failed to show the expected trend toward isotropy. Gross errors in the ERBE scene identification are thought to be the cause.

In the following, errors in the ERBE MLE method are revealed in the angular dependence of the frequencies of occurrence for the four ERBE cloud cover conditions. Reasons for these errors are discussed in section 5.3. Because of the angular dependence in the ERBE MLE scene identification errors, a bispectral threshold method is developed in order to identify scene types that are consistent from nadir to limb. The thresholds rely on two assumptions: 1) the ERBE MLE correctly identifies scenes at nadir and 2) for a sufficient number of observations, the frequencies of occurrence for each cloud scene type should be constant from nadir to limb for CFOV observations. The ERBS observations at nadir are used to simulate the frequencies of occurrence for off-nadir angles. The CFOV ADMs and FFOV ADMs are constructed based on the threshold scene identification. These models are compared in section 5.5.

5.2 Scene Identification Errors

The ERBE MLE method was developed to identify cloud scene types based on results obtained from the Nimbus-7 ERB experiment (Wielicki and Green, 1989). The scene types of the Nimbus-7 ERB observations were identified by using the measurements from the THIR/TOMS instruments. For the Nimbus-7 ERB scanner, the size of the field of view was almost constant for view zenith angles less than 70°. To obtain a constant size field of view, the scan head was designed to rotate at different stepping rates so that larger aperture fields of view were at nadir and smaller aperture fields of view at the limb (Jacobowitz et al., 1984). On average, the observed fractional cloud cover should be insensitive to view zenith angle provided the field of view size is held fixed. Applying the ERBE MLE method to the Nimbus-7 ERB scanner observations for June, 1979, Suttles et al. (1992) found that the derived fractional cloud cover varied little with view angle for angles less than 70°.

The scanner aboard ERBS had a spatial resolution of about 40 km at nadir. The resolution was different from that of the Nimbus-7 ERB scanner which was about 90 km. The ERBS scanning radiometer measurements were identified by the ERBE MLE. The performance of the ERBE MLE scene identification was checked by examining view zenith angle dependence of the derived fractional cloud cover for CFOV observations. The fractional cloud cover for a particular view zenith angle was calculated as follows

$$\mathrm{CLD} = \frac{A_{\mathrm{CLR}}N_{\mathrm{CLR}} + A_{\mathrm{PC}}N_{\mathrm{PC}} + A_{\mathrm{MC}}N_{\mathrm{MC}} + A_{\mathrm{OV}}N_{\mathrm{OV}}}{N_{\mathrm{TOTAL}}} \tag{5.1}$$

where N_{CLR}, N_{PC}, N_{MC} and N_{OV} were the number of clear, partly cloudy, mostly cloudy and overcast ERBS pixels. N_{TOTAL} was the total number of ERBS pixels. The weighting factors, A_{CLR} , A_{PC} , A_{MC} , A_{OV} , were the mean cloud cover fractions for the four cloud categories used in the ERBE ADMs. $A_{\mathrm{CLR}} = 2.5\%$ for clear, $A_{\mathrm{PC}} = 27.5\%$ for partly cloudy $A_{\mathrm{MC}} = 77.5\%$, for mostly cloudy and $A_{\mathrm{OV}} = 97.5\%$ for overcast scenes.

Fig. 5.1 shows the cloud cover obtained from ERBS observations for ocean and overcast scenes for September, October, November, 1986. There is an increase in cloud amount of about 10.9% from nadir to limb for the CFOV observations. This result illustrates that the ERBE MLE scene identification errors vary systematically with view zenith angle. The figure also shows results for FFOV observations. Cloud amount also increases with view zenith angle. The increase for the FFOV observations is about 16.5%. The lines in the figure do not meet as they should at the largest view zenith angle bin because different scan lines are used for the FFOV and CFOV data sets. The difference is due to sampling errors. Clearly, for both the FFOV and CFOV observations, the fraction of cloud cover identified by the ERBE MLE depends on the satellite zenith angle.

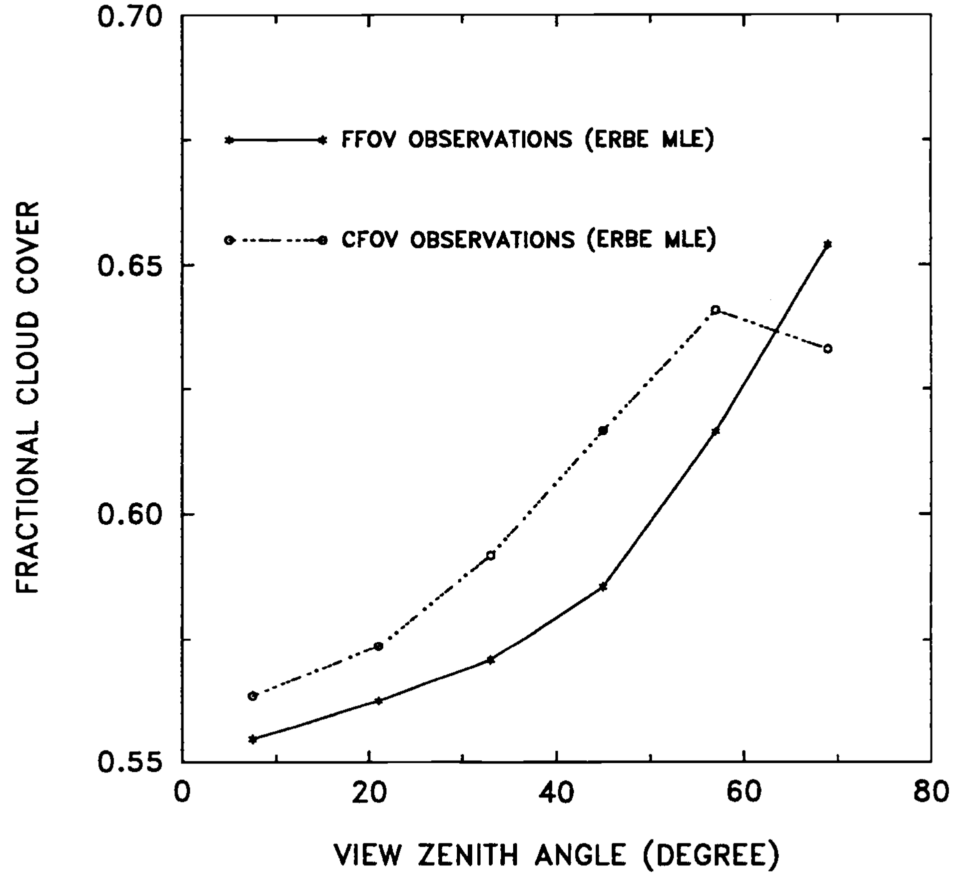

Figure 5.1 Fractional cloud cover derived by using the ERBE MLE method for the FFOV observations (solid line) and CFOV observations (dashed line) obtained from the ERBS scanner for September, October, November, 1986.

Fig. 5.2 shows the frequency of occurrence for the FFOV observations (solid lines) and CFOV observations (dashed lines) of the four cloud cover categories identified by the ERBE MLE. For the FFOV observations, the frequency of occurrence decreases for clear sky scenes and increases for overcast scenes with increasing view zenith angle. The frequencies are almost constant from nadir to limb for both partly cloudy and mostly cloudy scenes. For the CFOV observations, the frequency of occurrence for clear sky scenes is almost constant, but for partly cloudy and mostly cloudy scenes the frequencies decrease and for overcast scenes the frequencies increase with increasing view zenith angle.

Regions that are about (60 km)^2 contain broken clouds approximately 70% of the time and regions that are about (250 km)^2 contain broken clouds about 90% of the time (Chang and Coakley, 1993). Fig. 5.3 gives a typical daily cloud picture obtained from Geostationary satellite imagery data (GOES). It is clear that there is a high probability that the large fields of view will be either partly or mostly cloudy. The FFOV observations have a small field of view size at nadir and a large field of view size at the limb. There should be more clear and overcast scenes at nadir and fewer at the limb. Likewise, there should be fewer partly cloudy and mostly cloudy scenes at nadir and more at the limb. Fig. 5.2 shows that with the exception of the clear scenes, which decrease in frequency with increasing view zenith angle, the frequencies of occurrence for the other scene types counter the expected trends. The overcast scene type even shows increasing frequency of occurrence from nadir to limb. The discrepancies between the MLE results and expectations can be seen more clearly for the CFOV observations. With a constant size field of view from nadir to limb, the frequencies of occurrence are expected to be constant for all four cloud cover categories. Again, except for the clear scene type, the results for all three cloud scenes identified by the ERBE MLE counter expectations.

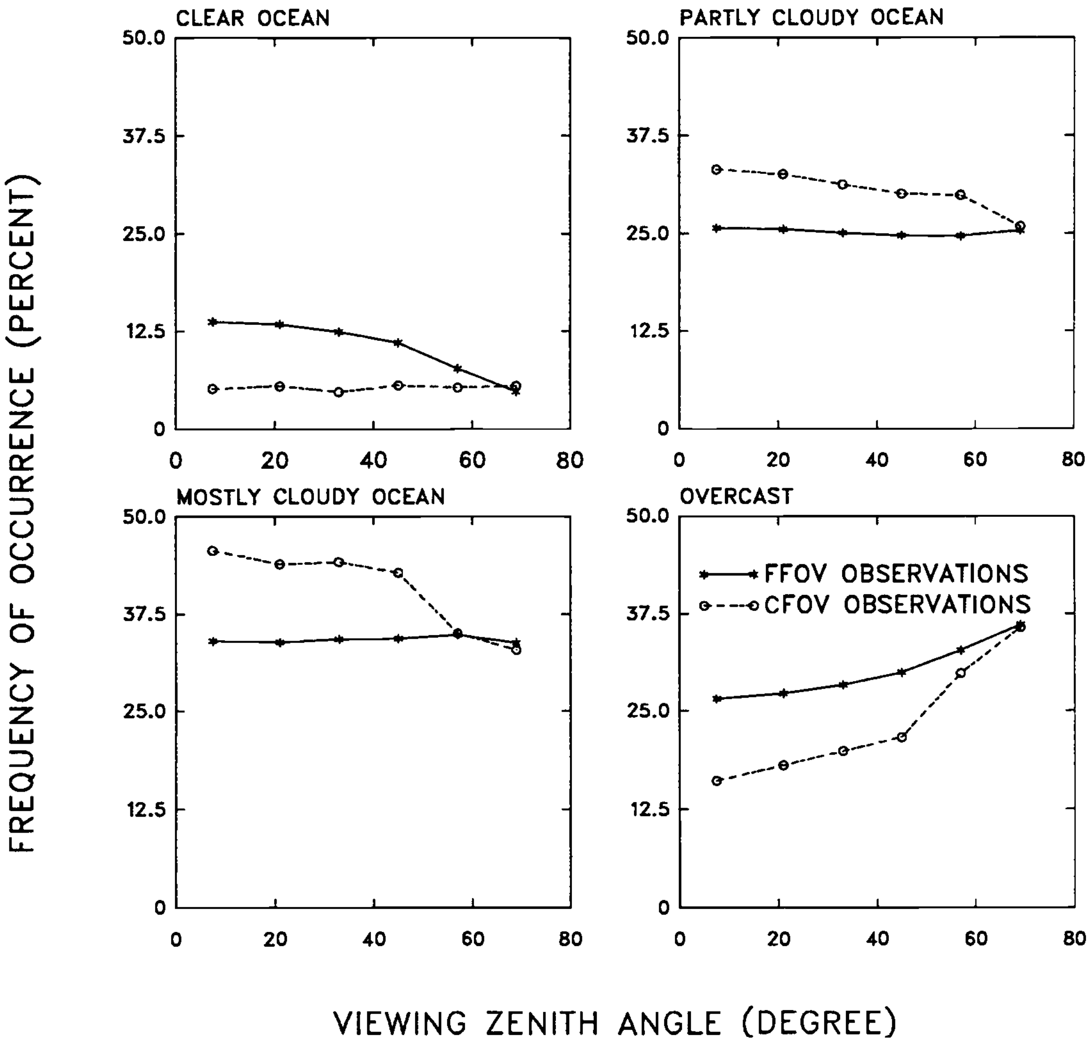

Figure 5.2 Frequency of occurrence for three cloud scene types over ocean and overcast scenes calculated for the FFOV data set (solid line) and CFOV data set (dashed line) obtained from the ERBS scanner observations employing the ERBE MLE scene identifications for September, October, November, 1986.

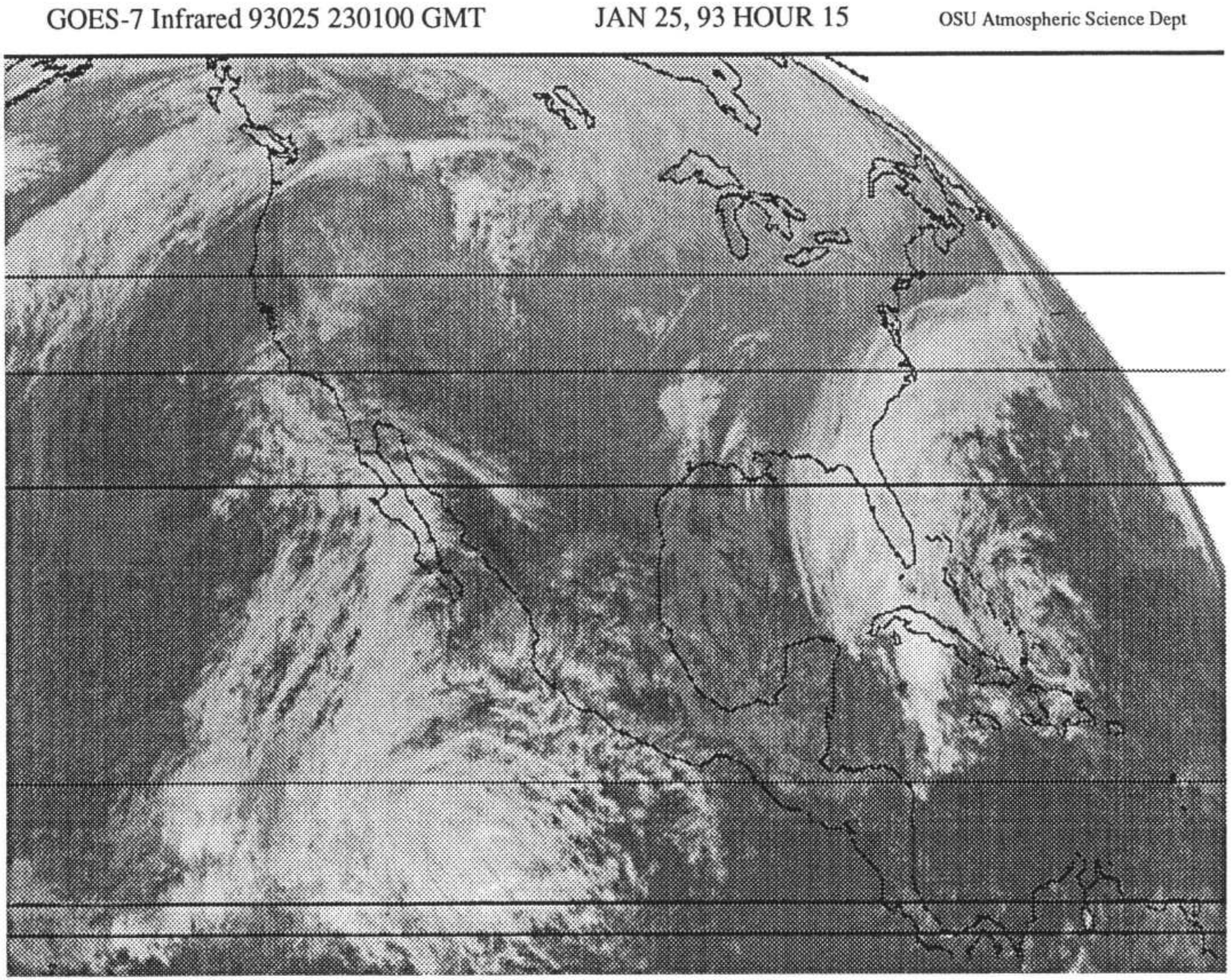

Figure 5.3 Example of daily cloud picture obtained from GOES satellite observations.

5.3 Causes Of Scene Identification Errors

Analysis of satellite imagery data indicates that clouds are frequently broken at the resolution of the ERBE scanner. For certain types of broken clouds, for example, cumuliform clouds, the vertical dimensions are on the same order as the horizontal dimensions. Both theoretical studies (McKee and Cox, 1974; Davies, 1978; Davies, 1984; Welch and Wielicki, 1984; Breon, 1992; Kobayashi, 1993) and analysis of satellite imagery data (Coakley and Davies, 1986; Coakley, 1991) show that broken clouds reflect solar radiation differently than their plane-parallel counterparts. Broken clouds also influence the radiation field through cloud-cloud interactions, cloud side viewing and shadowing effects. These effects should be taken into account when the fraction of cloud cover is estimated from observed radiances. For scanning radiometers, for which the spatial resolution of the field of view decreases from nadir to limb, two questions arise. First, with increasing view zenith angle, how do cloud sides affect estimates of cloud cover? Second, how does the increasing field of view size affect cloud identification due to the effect of cloud clustering?

5.3.1 Effects Of Cloud Vertical Extent On The Estimation Of Cloud Cover

Fig. 5.4 illustrates the effect of cloud vertical extent on the estimation of cloud cover made by the ERBS scanning instrument. In Fig. 5.4, there are three individual clouds extending vertically to different altitudes. When the scanner looks directly downward (nadir view), the fraction of cloud cover is given by the summation of the effective cloud top areas of the individual clouds. By contrast, when the scanner looks at the same scene with large view zenith angle, in addition to the cloud tops, the cloud sides are also viewed as part of the cloud cover. The contribution of cloud sides to the cloud cover becomes larger with increasing view angle. Consequently, through the "eyes" of a scanner, on average, there are more clouds at the limb than at nadir. Thus, the fractional

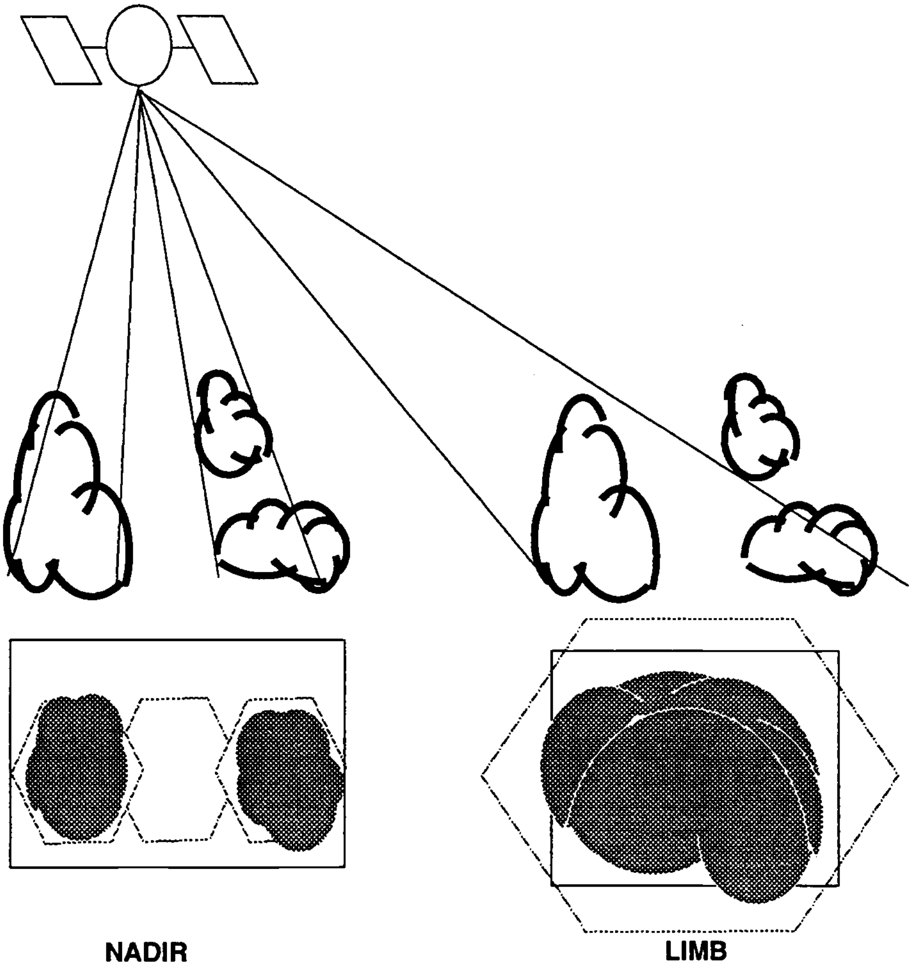

Figure 5.4 Illustration of the effect of cloud vertical structure on the estimation of cloud cover at the limb. Fields of view are given in the hexagons.

cloud cover obtained by using scanning radiometer observations should increase with view zenith angle. This increase occurs for the ERBE MLE method.

To illustrate the effect of cloud sides on estimates of cloud cover, the ERBE MLE results are compared with a theoretical study made by Davis et al. (1979). Davis et al. showed that for cubic clouds the effective cloud cover was greater than the geometric cloud cover by the factor (1 + tanθ), where θ was the view zenith angle. For the sake of comparison only, the ERBS observations identified as being overcast by the ERBE MLE are used here. Overcast scenes are those for which the fractional cloud cover is thought to be greater than 95%. If the ERBE MLE is affected by cloud sides, then the population of overcast scenes identified will increase from nadir to limb. Since the effect of cloud sides is negligible for the fields of view at nadir, the ERBE scene identification is assumed to be correct at nadir. The population of overcast scenes for off-nadir angles is simulated by averaging a certain number of ERBS neighboring observations at nadir to make up areas which match the sizes of the fields of view at off-nadir angles. The made-up data set is then used to simulate the population along the scan lines. Details of the simulation procedure are given in the next section. The simulated population of overcast scenes is thought not to be affected by cloud sides.

Fig. 5.5 shows the ratio of the ERBE MLE population to the simulated population as a function of view zenith angle. If the ERBE MLE is affected by cloud sides, then the ratio will increase with satellite zenith angle. Fig. 5.5 clearly shows such an increase. The theoretical result given by Davis et al. (1979) for cubic clouds is also shown in Fig. 5.5. Good agreement between the theoretical and observed results is somewhat fortuitous. Since the ERBE MLE is subject to scene identification errors, the simulated population is probably wrong. Nevertheless, the results shown in here are consistent with effects due to cloud sides.

5.3.2 Effects Of The Clustering Of Clouds

Clouds are not uniformly distributed in space. They tend to cluster on certain spatial scales (Fig. 5.3). Consequently, small regions that are identified as being cloud-free are frequently extracted from the midst of broken cloud systems and are likely to be cloud contaminated. On the other hand, large regions that are cloud-free, provided they are indeed cloud-free, are likely to be extracted from vast regions that are also cloud-free and are thereby free of cloud contamination. The same situation occurs for overcast scenes with clear contamination. The ERBS scanner observations are now used to demonstrate the effects of clustering.

Consider two field of view sizes at nadir. One is equal to that of the ERBS field of view. The other is equal to that of the CFOV field of view, which is equal to that of the ERBS field of view at a view zenith angle of 75°. For a field of view which

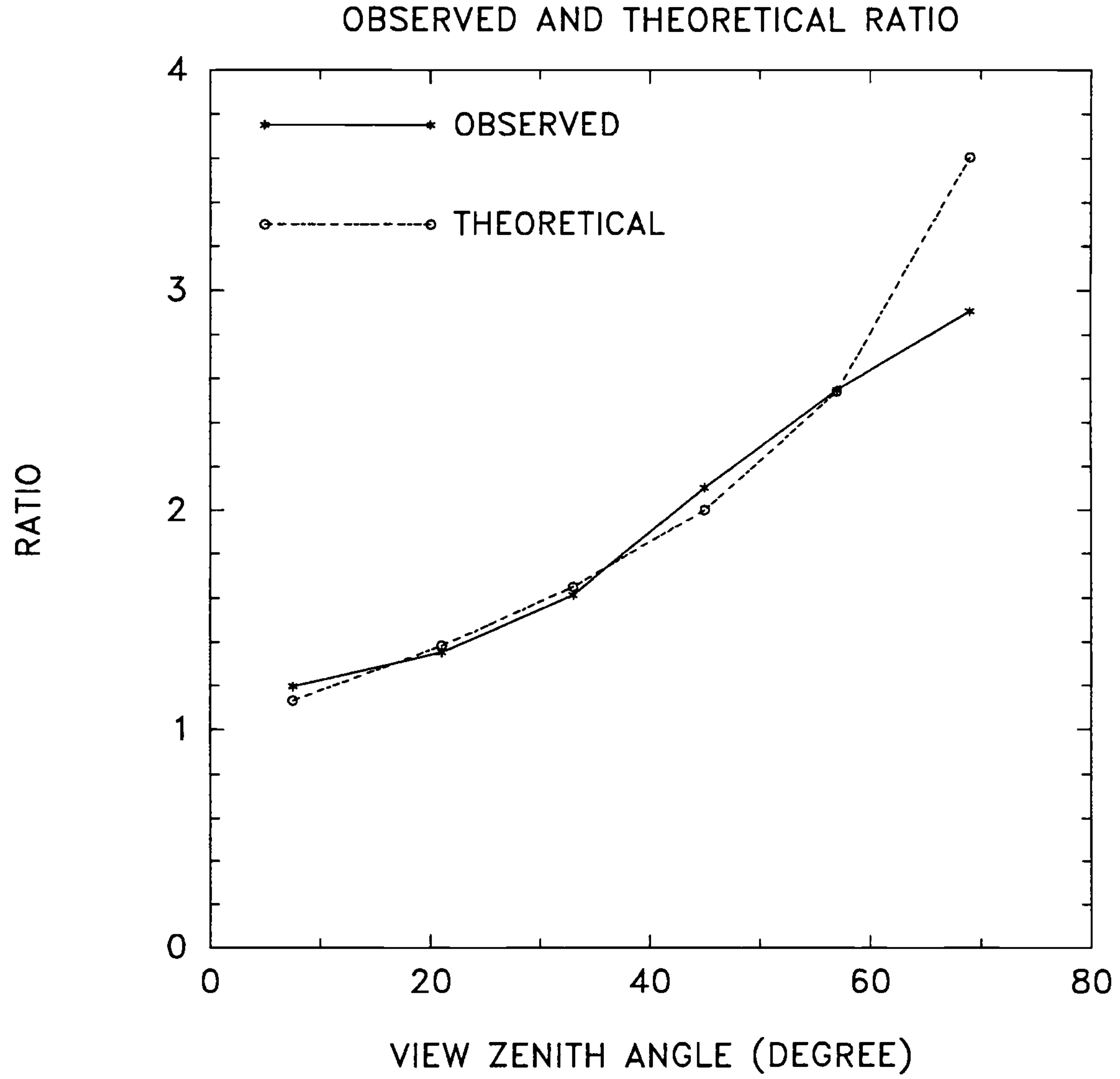

Figure 5.5 Ratio of cloud cover as a function of satellite zenith angle to that at nadir. The observations are for the frequency of overcast scenes identified by the ERBE MLE. The theoretical values are for cubic clouds given by Davis et al. (1979).

was identified as clear ocean by the ERBE MLE, the number of the surrounding fields of view which were also identified as clear oceans were recorded. The same accounting was performed for overcast scenes. For both field of view sizes, full resolution and CFOV, the surrounding fields of view used in the calculation had the size of the ERBS nadir field of view.

Fig. 5.6 shows the probability that the indicated number of surrounding fields of view, expressed as a percentage of the number of adjacent fields of view, have the same scene type as the center field of view. The surrounding pixels have the size of the ERBS nadir field of view. There are twenty such pixels around a CFOV field of view, and eight around a FFOV nadir field of view. The results show that for the large field of view, CFOV, the probability that the surrounding area has the same scene type is larger than that for the small field of view, FFOV. For a clear CFOV field of view, the probability that all surrounding pixels (100%) are also clear is 0.609, and for overcast scenes it is 0.745 that the surrounding pixels are all overcast. For the FFOV case, the corresponding probabilities are 0.478 for clear oceans and 0.627 for overcast scenes. In other words, in the case of the FFOV observations, 52% (37%) of the time individual pixels identified as clear (overcast) are in the midst of a broken cloud field. Therefore, there is a higher probability that the FFOV clear scenes are cloud contaminated (overcast scenes are contaminated by clear breaks in the clouds). By contrast, for the fields of view near the limb, for which the field of view is large, when they are identified as cloud-free (or overcast), provided they are indeed cloud-free (or overcast), it is likely that they are extracted from vast regions that are also cloud-free (or overcast). Results for the CFOV show that only 39% (25%) of the time are clear (overcast) scenes in the midst of a broken cloud field. Consequently, the observations near limb are subject to less cloud contamination (or clear contamination for overcast scenes) provided, of course, the scene identification is correct. These results indicate that the ERBE MLE suffers a varying degree of cloud (for clear scenes) or clear (for overcast scenes) contamination from nadir to limb as a result of the growth in field of view size coupled with the spatial clustering of clouds and the inability to correctly identify scene types using the

MLE method. As shown in Fig. 3.5, the anisotropy of reflected and emitted radiation is sensitive to cloud cover. Thus, using the ERBE MLE scene identification leads to the application of inconsistent ADMs for nadir and limb scenes.

In conclusion, based on scanning radiometer measurements, the ERBE MLE method gives a biased scene identification. The bias is consistent with effects due to cloud vertical structure. They are also due to the varying degree of cloud contamination from nadir to limb. The effect of cloud vertical structure on the MLE increases with increasing view zenith angle while the degree of cloud or clear contamination decreases.

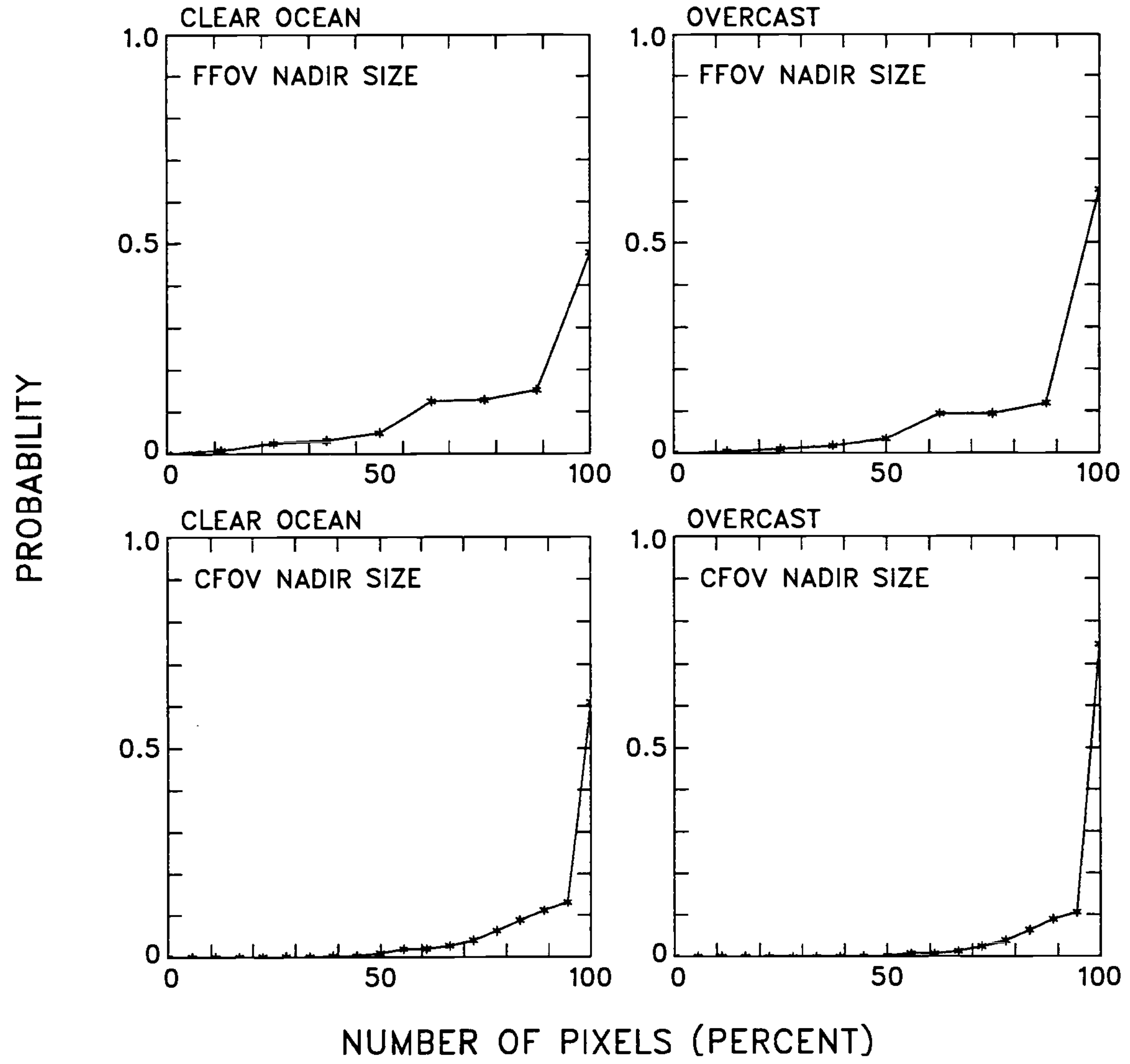

Figure 5.6 Probability that the percentage of surrounding pixels having a spatial resolution of (40 km)^2, will have the same identification as the center pixel. Results are based on the ERBS nadir observations with the ERBE MLE scene identification for September, 1986.

5.4 Method

Using coarse spatial resolution bispectral radiance pairs, the ERBE MLE exhibits scene identification errors that vary systematically with view zenith angle. Errors due to the vertical structure of clouds increase with increasing view zenith angle. Errors due to cloud clustering, however, are expected to be large at nadir but small at the limb. A simple bispectral threshold cloud scene identification method was developed in an attempt to reduce the errors in the MLE scene identification.

A two-step procedure was used to obtain the thresholds from FFOV and CFOV observations. The first step was to simulate frequencies of occurrence for the four cloud categories based on nadir observations. Notice that the effect of cloud sides on estimates of cloud cover was assumed to be negligible at nadir. The cloud scene types at nadir identified by the ERBE MLE were taken to be correct. Then, in the second step, two sets of thresholds were derived according to the simulated frequencies of occurrence for the FFOV and CFOV observations. For FFOV observations, the thresholds were obtained by adjusting the population of scene types based on the simulated frequencies of occurrence. The thresholds based on the CFOV observations were derived under the assumption that the population of scene types should be constant with view zenith angle. The population of scene types were obtained based on the simulated frequencies of occurrence at nadir. The scene identification errors caused by a varying degree of cloud or clear contamination were expected to be reduced significantly using these thresholds.

5.4.1 Adjustment Of Frequencies Of Occurrence

The ERBS nadir observations were used to simulate frequencies of occurrence expected for large view zenith angles. Fig. 5.7 shows the number of neighboring ERBS nadir pixels required to form fields of view which match the area covered by the ERBS fields of view near the limb. The number of the ERBS nadir observations used to simulate the off nadir fields of view is listed in Table 5.1. (4.1) was used to determine the cloud amounts in the simulated fields of view. The cloud types for the simulated fields of view were assigned based on the ERBE criteria. Frequencies of occurrence of the three cloud categories over oceans and overcast scenes were calculated for the simulated fields of view.

Table 5.2 lists simulated frequencies of occurrence as a function of view zenith angle for FFOV observations. The frequencies of occurrence decrease for clear and overcast scenes and increase for partly and mostly cloudy scenes with field of view size growing from 0.158×10^4 $(\mathrm{km})^2$ at nadir to 2.440×10^4 $(\mathrm{km})^2$ at the limb. Broken cloud systems occur 60% of the time at nadir, but, about 80% of the time at the limb.

Table 5.1 Number of nadir pixels used to simulate fields of view from nadir to limb.

Bin number	View zenith angle (degree)	Adjacent fields of view × scan lines
1	0.0 - 15.0	1×1
2	15.0 - 27.0	2×1
3	27.0 - 39.0	3×1
4	39.0 - 51.0	4×2
5	51.0 - 63.0	5×2
6	63.0 - 75.0	6×2

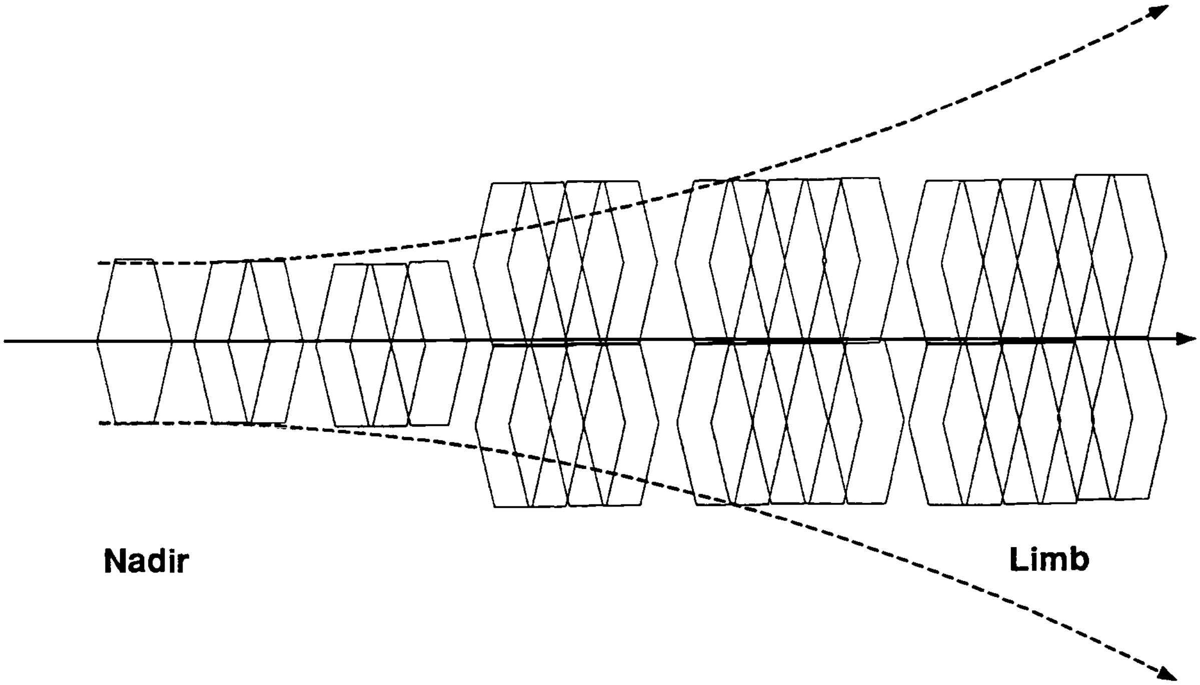

Figure 5.7 Grouping of nadir fields of view used to simulate growth of field of view with view zenith angle. Dashed lines are the boundaries of actual fields of view for ERBS observations.

Table 5.2 Simulated frequencies of occurrence for the FFOV observations as a function of view zenith angle.

Bin No.		1	2	3	4	5	6
View zenith angle (degree)		0.0 - 15.0	15.0 - 27.0	27.0 - 39.0	39.0 - 51.0	51.0 - 63.0	63.0 - 75.0
Simulated field of view size (10^4 km^2)		0.158	0.190	0.252	0.396	0.790	2.440
Frequency of occurrence (%)	Clear	17.2	15.6	13.1	9.6	8.7	7.8
	Partly cloudy	28.6	27.9	32.6	35.8	37.2	37.1
	Mostly cloudy	32.5	36.6	36.8	40.9	41.6	43.4
	Overcast	21.7	19.9	17.5	13.7	12.6	11.8

5.4.2 FFOV Thresholds

Based on the simulated frequencies of occurrence, shortwave and longwave radiance thresholds were determined for the separation of the cloud scene types identified by the ERBE MLE method. These thresholds were adjusted so that the population of observations were equal to that given by the simulated frequencies of occurrence. The adjustments were made for each angular bin. Fig. 5.8 illustrates the procedure. The MLE method for this viewing geometry evidently misidentified some mostly cloudy scenes as overcast, and some clear scenes as partly cloudy scenes. The population of overcast (or clear) scenes had to be reduced according to the simulated frequency of occurrence derived from the nadir observations. The initial longwave threshold radiance was decreased (moved downward in the figure), and the initial shortwave threshold radiance was increased (moved right in the figure) in order to reclassify some of the overcast scenes to mostly cloudy scenes. The ratio of the change in the longwave radiance and the change in the shortwave radiance was determined by the correlation coefficient between the radiances. The threshold boundaries were adjusted in a similar manner for the transition between clear scenes and partly cloudy scenes. After boundaries for overcast and clear scenes were determined, the boundary between partly and mostly cloudy scenes was determined by adjusting both shortwave and longwave radiance values simultaneously in such a way that the boundary remained normal to the line which connected the means of the partly and mostly cloudy observations (cross signs in the figure) as identified by the ERBE MLE scene identification. The final position of the boundary was determined by the values of the adjusted frequencies of occurrence for the particular angular bin. In the example shown, the adjustment caused some points identified as overcast (clear) by the ERBE MLE method to become mostly cloudy (partly cloudy) and some ERBE partly cloudy pixels became mostly cloudy. Since the thresholds were obtained from the FFOV observations, they will be referred to as the FFOV thresholds.

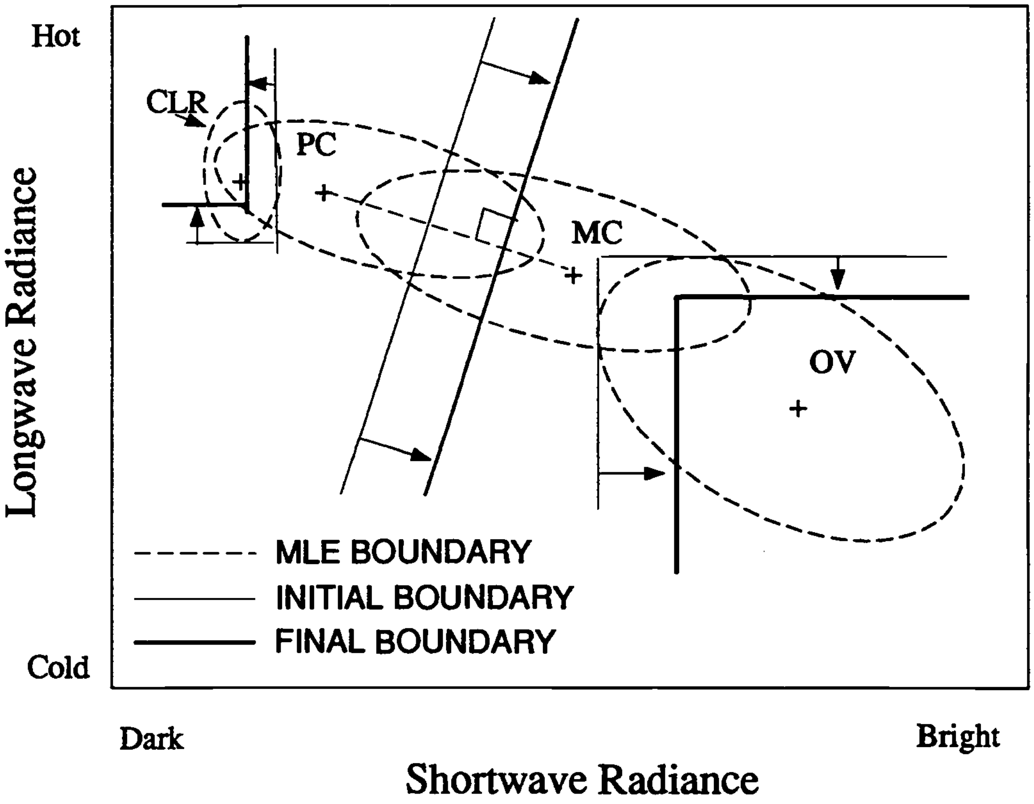

Figure 5.8 Illustration of procedure used to obtain the thresholds based on simulated frequencies of occurrence derived from nadir observations.

Obviously, FFOV thresholds led to mean radiances, standard deviations and correlation coefficients that differed from those in the ERBE MLE. Fig. 5.9 shows an example of the differences for the means of shortwave and longwave radiances obtained by the MLE method and by the FFOV threshold method for ERBS scanner observations. Also shown in Fig. 5.9 are the results for the thresholds derived using the CFOV observations. These thresholds were referred to as the CFOV thresholds in the figure. The procedure for obtaining the CFOV thresholds was the same as that for obtaining the FFOV thresholds.

Fig. 5.9 shows percent differences for the mean radiances as a function of view zenith angle. The differences were calculated by subtracting the radiances obtained using the threshold methods from those obtained using the ERBE MLE. For clear scenes identified using the FFOV thresholds, the means of the reflected shortwave radiances were smaller than those obtained using the ERBE MLE (positive percent differences for all view zenith angles as shown in the figure). The corresponding means of longwave radiances, however, were larger (negative percent differences for all view zenith angles). Conversely, for overcast scenes, the means of the reflected shortwave radiances were larger and the means of the longwave radiances were smaller using the threshold methods. Since clouds reflect more sunlight but emit less longwave radiation than surfaces, these results indicate that the clear (overcast) scenes identified by the FFOV threshold method appeared to be clearer (cloudier) than those identified by the ERBE MLE method and thereby might well have been less cloud (clear) contamination. It should be pointed out that there was no evidence that the threshold identifications were any better at scene identification than the MLE. Here, the intent was only to obtain a consistent identification of scene type with view zenith angle.

Fig. 5.9 also shows that the differences of the mean radiances between the FFOV threshold and MLE methods increased with increasing fractional cloud cover. For cloudy scenes, the differences increased with view zenith angle as well. The cause for this increase is thought to be due to the effect of cloud sides. With increasing view zenith angle, more cloud sides are probably treated by the ERBE MLE as cloud tops. As a result, some mostly cloudy or even partly cloudy scenes were probably misidentified by the ERBE MLE as overcast scenes. Hence, the means of the shortwave (longwave) radiances obtained from the ERBE overcast scenes were expected to be smaller (larger) than those obtained from the real overcast scenes. Such differences should increase as the effect of cloud sides increases from nadir to limb.

Fig. 5.10 shows the frequencies of occurrence for FFOV observations (solid lines) and CFOV observations (dashed lines) based on the FFOV threshold scene identification. For the FFOV observations, the frequencies of occurrence from nadir to limb decrease for clear and overcast scenes and increase for partly and mostly cloudy scenes. For the CFOV observations, the frequencies for all scenes are relatively constant. The variations are caused by the inaccuracy of thresholds used and the lack of sufficient observations in every angular bin in the period of observations used in this study.

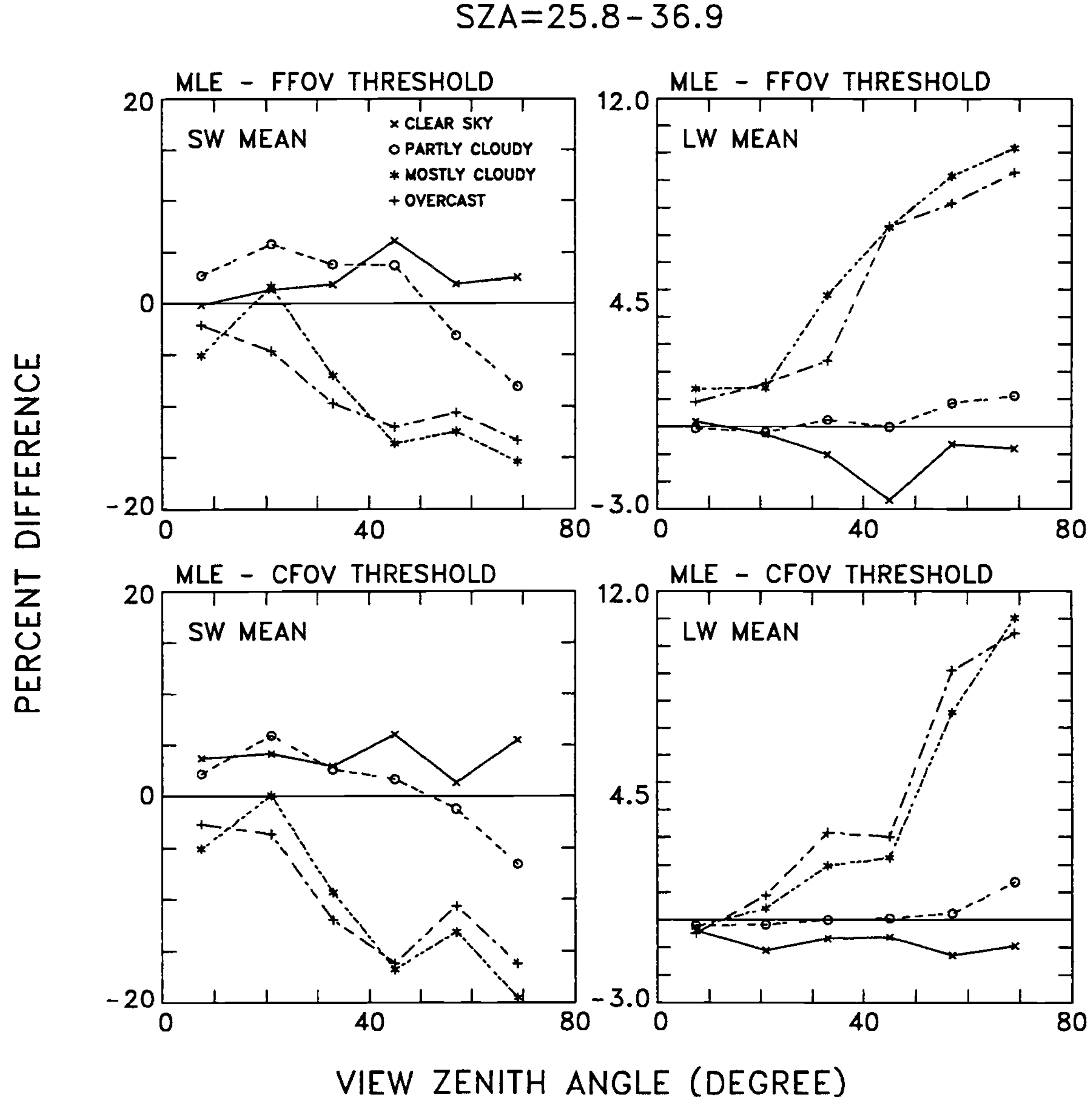

Figure 5.9 Percent differences in the mean radiances for scenes identified by the ERBE MLE method and those identified by the FFOV and CFOV thresholds. The calculations were made by subtracting the means obtained using the thresholds from those obtained using the ERBE MLE based on the ERBS observations for September, October, November, 1986. The results presented in the figure are azimuthally averaged. They are for solar zenith angles between 25.8° and 36.9°.

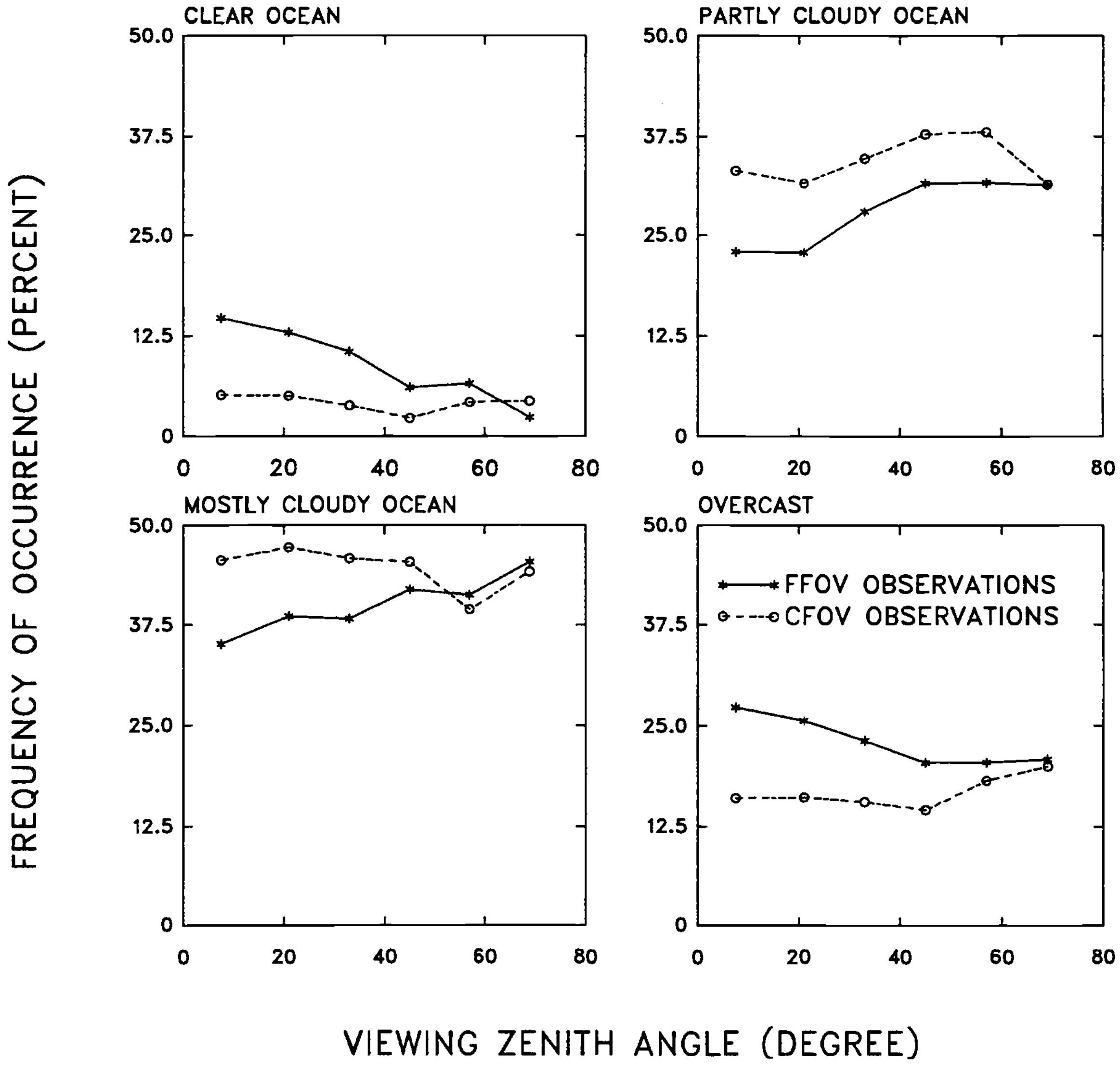

Figure 5.10 Frequencies of occurrence for the FFOV and CFOV observations identified using the FFOV thresholds. The results are based on ERBS observations for September, October, November, 1986.

5.4.3 CFOV Thresholds

The FFOV thresholds were derived for fields of view that grew from nadir to limb. Due to the effect of cloud clustering, the FFOV thresholds were not expected to consistently identify scene types from nadir to limb. The CFOV observations had a constant size field of view. The degree of cloud contamination in these observations should have remained relatively constant with view zenith angle. In the following, thresholds will be derived using frequencies of occurrence for the four cloud categories with the CFOV observations (Fig. 5.10).

Thresholds based on the CFOV were obtained following the same process as that for obtaining the FFOV thresholds. Frequencies of occurrence at nadir, which were obtained based on the ERBE MLE, were assumed to be correct. The frequencies of occurrence were held constant for varying view zenith angle. The thresholds were obtained by adjusting the positions of the boundaries among scene types so that the population of scene types equaled that at nadir. The resulting thresholds will be referred to as CFOV thresholds. Fig. 5.11 shows the FFOV and CFOV thresholds for a particular angular bin with solar zenith angle at 25.8° – 36.9°, view zenith angle at 0.0° – 15.0° and azimuthal angle at 9.0° – 30.0°. The markings indicate the MLE scene identifications, clear (×), partly cloudy (o), mostly cloudy (*) and overcast (+). The pixels which were identified as either clear sky or overcast by the MLE but reidentified by applying the FFOV and CFOV thresholds are marked with the arrows. Clearly, the CFOV thresholds were more restrictive than were the FFOV thresholds for clear and overcast scenes.

Fig. 5.9 shows the means for shortwave and longwave radiances obtained by the MLE and the CFOV threshold methods for the ERBS observations. The results were similar to those for the comparison of the MLE and the FFOV threshold methods. The azimuthally averaged differences in the mean radiances between the FFOV and the CFOV threshold methods are listed in Table 5.3. For reflected shortwave radiances, the means obtained using the CFOV thresholds were smaller for clear/partly cloudy ocean scenes than those obtained using the FFOV thresholds. They were larger for mostly cloudy ocean and overcast scenes. For clear oceans, the means for the longwave radiances were larger for the CFOV than those for the FFOV. Evidently, the CFOV threshold method had clear scenes that were probably less cloud contaminated than those identified by the FFOV thresholds. The overcast scenes identified by the CFOV thresholds generally reflected more sunlight and emitted less longwave radiation than those identified by the FFOV threshold method. The CFOV threshold method had overcast scenes that were probably less clear contaminated than those identified by the FFOV thresholds.

Fig. 5.12 shows the frequencies of occurrence for the four cloud categories identified by the CFOV threshold method for the FFOV (solid line) and CFOV (dashed line) observations based on ERBS observations for September, October, November, 1986. Compared with the results obtained using the FFOV thresholds (Fig. 5.10), almost constant frequencies of occurrence were obtained for the CFOV observations. For FFOV observations, the CFOV thresholds produced frequencies of occurrence near nadir for clear ocean and overcast scenes that were smaller than those produced by the FFOV thresholds. The lower frequencies for FFOV observations were expected because the CFOV thresholds were usually more restrictive than were the FFOV thresholds for clear and overcast scenes. Scenes near nadir, which were identified as being clear or overcast by the FFOV thresholds, were likely to be in the midst of broken clouds. Using the CFOV thresholds, some of these scenes were identified as partly or mostly cloudy.

Table 5.3 Percent differences of the mean radiances for the CFOV and FFOV thresholds. The results were averaged azimuthally for solar zenith angle 25.8° – 36.9°. Observations are from the ERBS scanner for cloudy ocean and overcast scenes for September, October, November, 1986.

Scene type	Percent difference of means (CFOV - FFOV)	
	Reflected shortwave	Longwave
Clear ocean	-6.30	0.64
Partly cloudy ocean	-0.90	0.31
Mostly cloudy ocean	6.26	-0.63
Overcast	6.77	-2.95

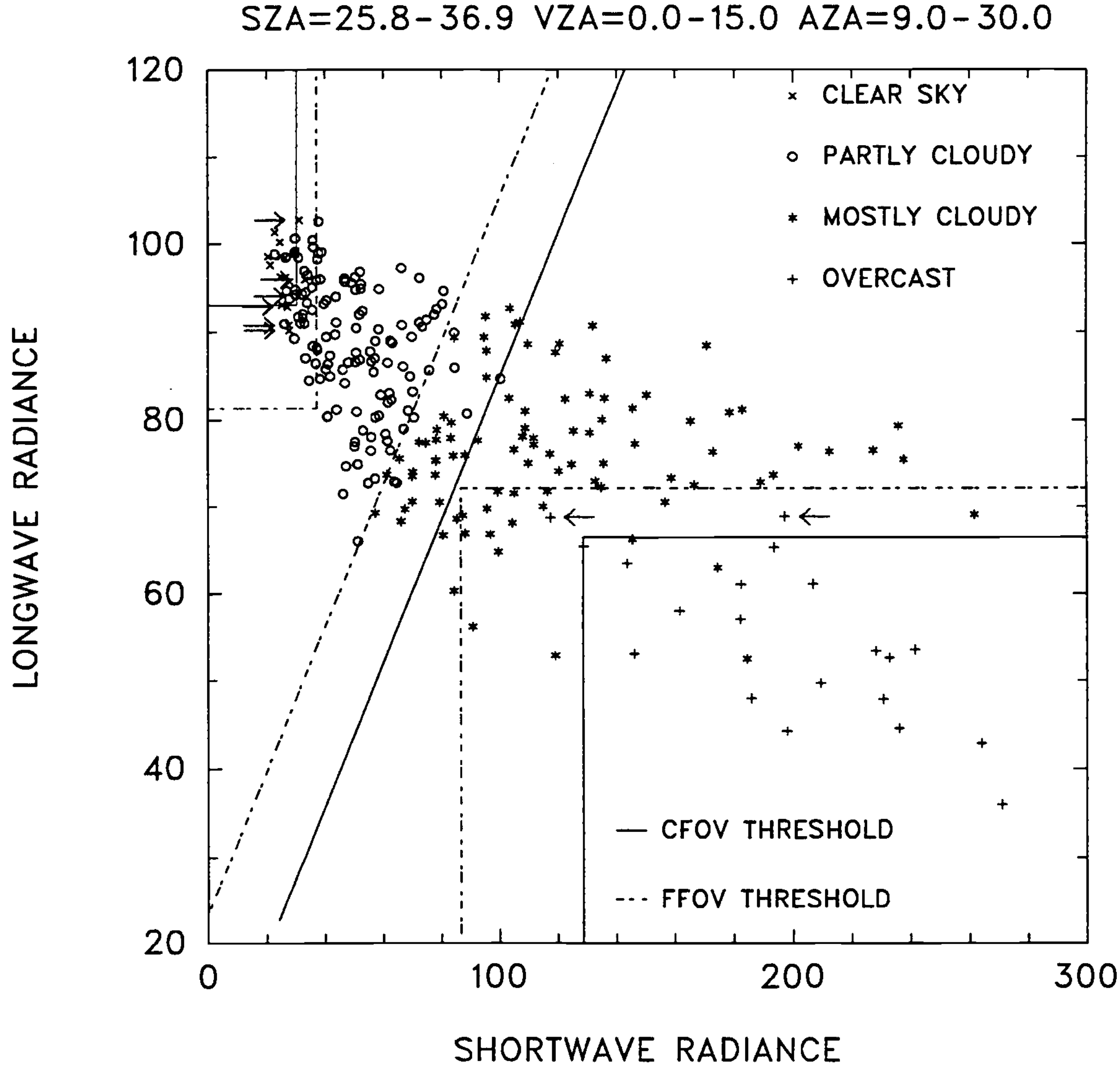

Figure 5.11 An example showing the effect of FFOV and CFOV thresholds on scene identification. The arrows in the figure point the pixels which are identified as either clear sky or overcast by the MLE but are reidentified by applying the FFOV and CFOV thresholds. Radiances are plotted in units of $Wm^{-2}sr^{-1}$.

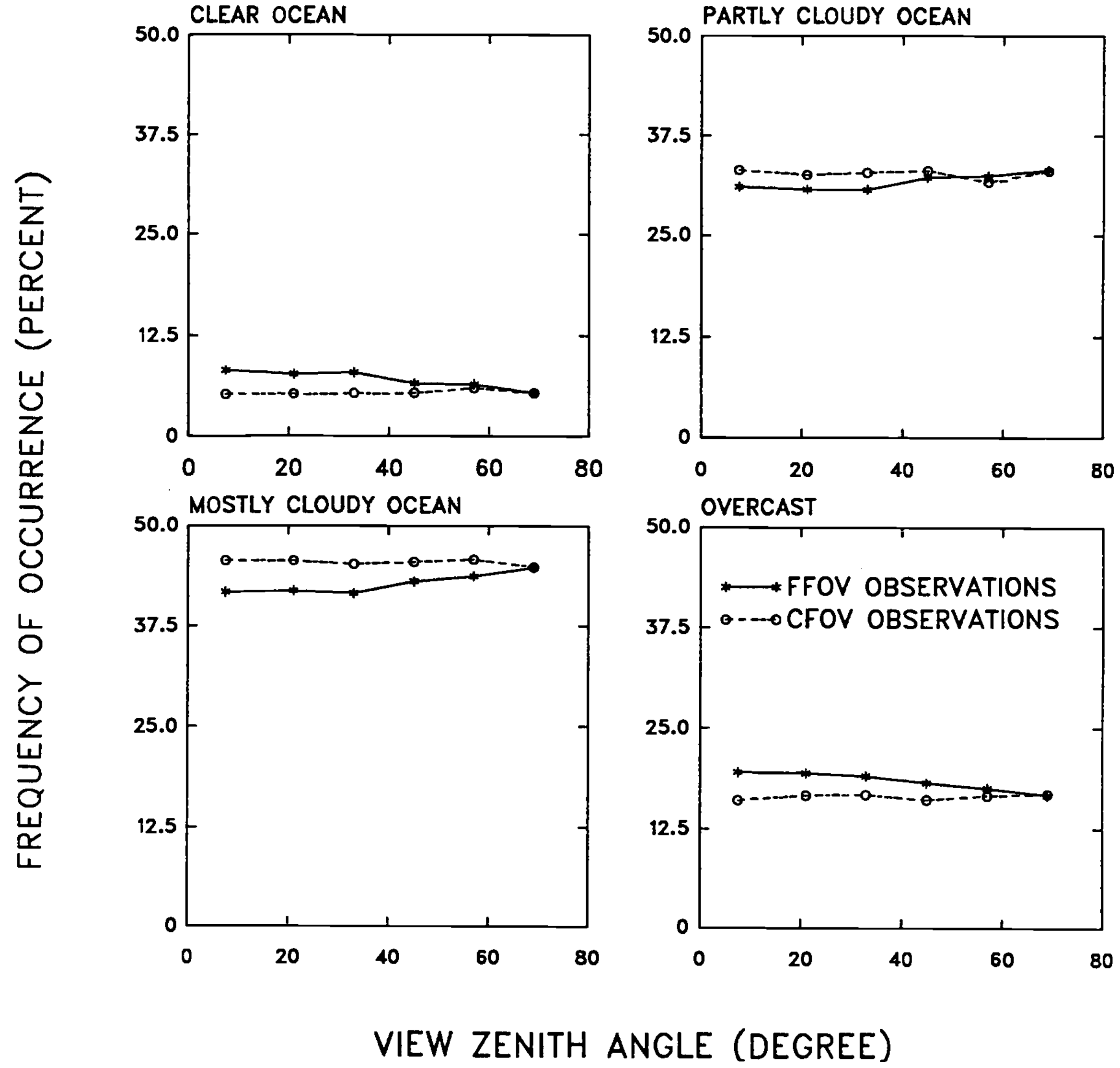

Figure 5.12 Frequencies of occurrence for the FFOV and CFOV observations identified using the CFOV thresholds. The results are based on ERBS observations for September, October, November, 1986.

5.5 Results

The FFOV and CFOV thresholds were applied to the ERBS observations. The fractional cloud cover derived from both thresholds remained nearly constant with increasing view zenith angle (Fig. 5.13). Using the procedures presented in chapter 4, FFOV and CFOV ADMs were constructed using the FFOV and CFOV thresholds.

5.5.1 Results For Shortwave Radiation Based On FFOV Threshold Scene Identification

Figs. 5.14 and 5.15 show the ADMs obtained by applying the FFOV threshold scene identification to the FFOV and CFOV observations. Fig. 5.14 gives the percent difference (FFOV ADMs — CFOV ADMs) for the solar zenith angle bins which had the largest domains for which the differences were significant at the 90% confidence level (shaded regions). Fig. 5.15 gives the same as Fig. 5.14 but for solar zenith angle bins which had the smallest domain of significant differences. Compared with Figs. 4.6 and 4.7, the differences between the FFOV and CFOV ADMs were significantly reduced both in magnitude and in the number of bins found to have significant differences. Furthermore, the differences shown in Figs 5.14 and 5.15 appeared to be more randomly distributed in viewing zenith and azimuth angle domains. Table 5.4 gives the percentage of angular bins which had significant differences at the 90% confidence level. Clearly, using the FFOV thresholds, these percentages were smaller than those obtained using the ERBE MLE, i.e., from 60.9%, 76.6%, 47.9% and 63.7% to 16.3%, 14.8,%, 17.4% and 22.5% for clear, partly cloudy, mostly cloudy ocean scenes and overcast scenes.

Fig. 5.16 shows the azimuthally averaged anisotropy (4.11) for the FFOV and CFOV observations obtained with the FFOV threshold scene identification. The azimuthally averaged anisotropic factors were averaged for all solar zenith angles. As was discussed in section 5.3, if the scene types were correctly identified, then because of the effects of cloud clustering, the CFOV observations would be expected to show a higher degree of anisotropy for clear sky conditions and a lower degree of anisotropy for overcast conditions than would the FFOV observations. Fig. 5.16 shows that for clear ocean scenes, the average anisotropic factors for the CFOV observations were smaller at nadir and larger at the largest view zenith angle than those for the FFOV observations. For overcast scenes, this trend was reversed. The CFOV observations appeared to be more anisotropic for clear sky scenes and more isotropic for overcast scenes than were the FFOV observations.

The degree of anisotropy for the CFOV observations was expected to be larger/smaller for clear/overcast scenes than was that for the FFOV observations. Fig. 5.17 shows the degree of anisotropy defined by (3.18) for the four cloud conditions. For most of the solar zenith angles, the CFOV observations gave a higher/lower degree of anisotropy for clear ocean/overcast conditions than did the FFOV observations. Fig. 5.17 shows the percent differences of the degree of anisotropy between the FFOV and CFOV ADMs. The differences were reduced from about 2 – 10% in Fig. 4.11 to about 0.5% overall. Since there were different field of view sizes for the FFOV and CFOV observations, the ADMs derived using the FFOV threshold scene identification method showed less spatial-scale dependence than those obtained using the ERBE MLE scene identification method. Thus, compared with the ERBE MLE scene identification, the FFOV threshold scene identification developed in this thesis performed more consistently with view zenith angle.

5.5.2 Results For Shortwave Radiation Based On CFOV Threshold Scene Identification

Because of cloud clustering and because of a growth of field of view size from nadir to limb, a varying degree of cloud or clear contamination was expected in the FFOV threshold scene identification. This varying degree of cloud or clear contamination could not be removed from FFOV observations. As shown above, even though the FFOV threshold method did reasonably well in reducing what was termed the effect of cloud sides compared with the ERBE MLE (Fig. 5.13), the derived anisotropy still appeared to be a function of spatial scale due to cloud clustering. CFOV observations had a constant size field of view from nadir to limb. The degree of cloud and clear contamination in the CFOV observations was expected to be the same from nadir to limb. Therefore, the CFOV thresholds, which were obtained from the CFOV observations, were expected to reduce the spatial-scale dependence of the ADMs.

The FFOV and CFOV ADMs were constructed using the CFOV threshold scene identification. Fig. 5.19 shows the percent differences (FFOV ADMs— CFOV ADMs) for the solar zenith angle bins which had the largest domain of significant differences at the 90% confidence level (shaded regions). Fig. 5.20 gives similar results for the solar zenith angle bins which had the smallest domain of significant differences. Compared with Figs. 5.14 and 5.15, the shaded areas in Figs. 5.19 and 5.20 appeared to be smaller. The azimuthally averaged anisotropic factors for the FFOV and CFOV observations identified by the CFOV thresholds are shown in Fig. 5.21. The azimuthally averaged anisotropic factors were averaged for all solar zenith angles. As was expected, for overcast scenes, the CFOV observations are more isotropic than the FFOV observations. The differences, however, are smaller compared with those shown in Fig. 5.16.

Fig. 5.22 shows the degree of anisotropy for the FFOV and CFOV observations identified by the CFOV threshold method as a function of solar zenith angle. Fig. 5.23 shows the percent differences of the degree of anisotropy for the FFOV and CFOV observations. Compared with Fig. 5.17, small improvements were observed for the four cloud categories. Table 5.4 lists the percentages of angular bins which had significant differences between the FFOV and CFOV ADMs at the 90% of confidence level. The percentages decreased from those obtained using the FFOV thresholds. For example, for clear oceans, this percentage was 13.1% for the FFOV thresholds but 2.9% for the CFOV thresholds. Decreases were also seen for mostly cloudy oceans and overcast, i.e., from 15.2% and 19.4% for the FFOV thresholds to 12.3% and 13.9% for the CFOV thresholds. For partly cloudy oceans, however, the CFOV thresholds gave a slight increase of about 1.7%.

5.5.3 Results For Longwave Radiation

The threshold methods also improved the longwave angular dependence models (limb-darkening models) by reducing the spatial-scale dependence of limb darkening. Fig. 5.24 shows differences in the degree of anisotropy between the FFOV and CFOV models based on the FFOV thresholds. Fig. 5.25 shows the same comparison but based on the CFOV thresholds. Compared with the results shown in Fig. 4.14, both threshold methods removed the spatial scale dependence for all view zenith angles except for view zenith angles greater than 60°. Table 5.4 lists the percentage of angular bins for which there were significant differences at the 90% confidence level. This percentage was down from 59%, 72%, 61% and 57% using the ERBE MLE to 25.6%, 35.4%, 29.2%, and 31.3% using the FFOV thresholds for clear, partly cloudy, mostly cloudy, and overcast scenes. The corresponding percentages were 22.2%, 25.0%, 27.1% and 22.9% using the CFOV thresholds.

Results obtained in this chapter can be summarized as follows. The view zenith angle dependence of the frequencies of occurrence for the four cloud categories was shown to be consistent with the dependence expected due to the effect of cloud sides. The effect of cloud clustering was also shown to be another contributing factor to scene identification errors. A bispectral threshold method was developed to identify scenes consistently from nadir to limb. The thresholds were based on the assumptions that the ERBE MLE correctly identified scenes at nadir and that the population of the four cloud categories for CFOV observations should have been constant from nadir to limb. The frequencies of occurrence for the four cloud categories identified by the threshold method were consistent with expectations. Using the CFOV threshold scene identification, the differences in the FFOV and CFOV ADMs were significantly reduced. Evidently, angular dependence models which are independent of instrument spatial resolution could be developed using a scene identification method which identifies consistent scene types from nadir to limb.

Table 5.4 Percentage of angular bins which had differences in the CFOV and FFOV anisotropic factors that were significant at the 90% confidence level. Percentages are given for the ERBE MLE, the FFOV and CFOV threshold methods applied to ERBS observations for September, October, November, 1986.

	Clear ocean	Partly cloudy ocean	Mostly cloudy ocean	Overcast
ERBE MLE Method	60.9%	76.6%	47.9%	63.7%
FFOV Thresholds	13.1%	12.9%	15.2%	19.4%
CFOV Thresholds	2.9%	14.6%	12.3%	13.9%

Table 5.5 Percentage of angular bins which had differences in the CFOV and FFOV limb-darkening models that were significant at the 90% confidence level. Percentages are given for the ERBE MLE, the FFOV and CFOV threshold methods applied to ERBS observations for September, October, November, 1986.

	Clear ocean	Partly cloudy ocean	Mostly cloudy ocean	Overcast
ERBE MLE Method	59.0%	72.0%	61.0%	57.0%
FFOV Thresholds	25.6%	35.4%	29.2%	31.3%
CFOV Thresholds	22.2%	25.0%	27.1%	22.9%

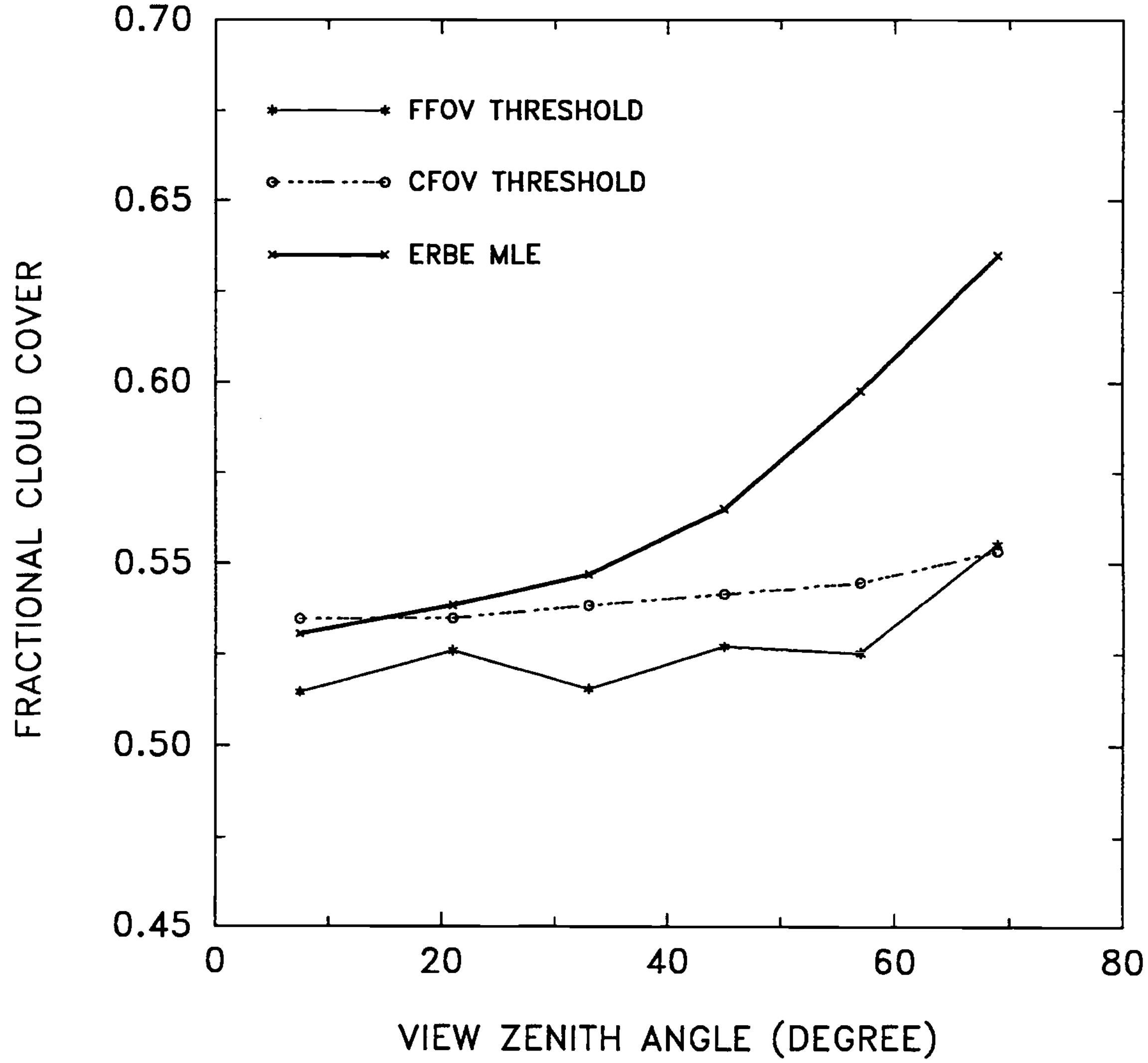

Figure 5.13 Fractional cloud cover derived using the ERBE MLE method (heavy solid line), the FFOV thresholds (solid line), and the CFOV thresholds (dashed line) applied to ERBS scanner observations for September, October, November, 1986.

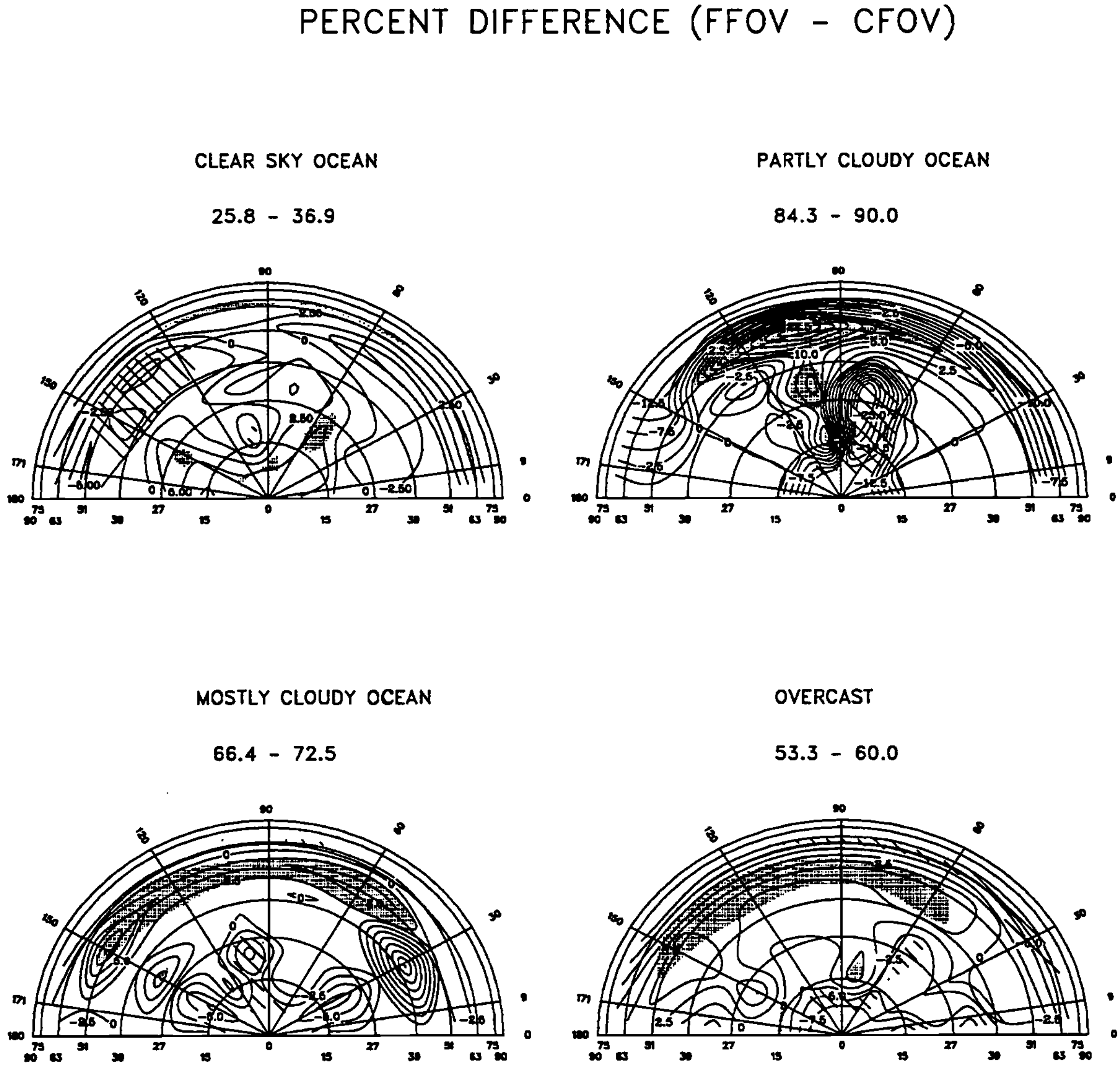

Figure 5.14 Percent differences between the FFOV and CFOV pseudo-ADMs for the solar zenith angle bins which had the largest domains for which the differences were significant. The solar zenith angles for each scene type are given in the figure. The radial axis is for view zenith angle, and the polar axis is for the relative azimuth angle. The increment of the contours is 2.5%. Regions in which the differences were positive and significant at the 90% confidence level are shaded, and those that were negative and significant are hatched.

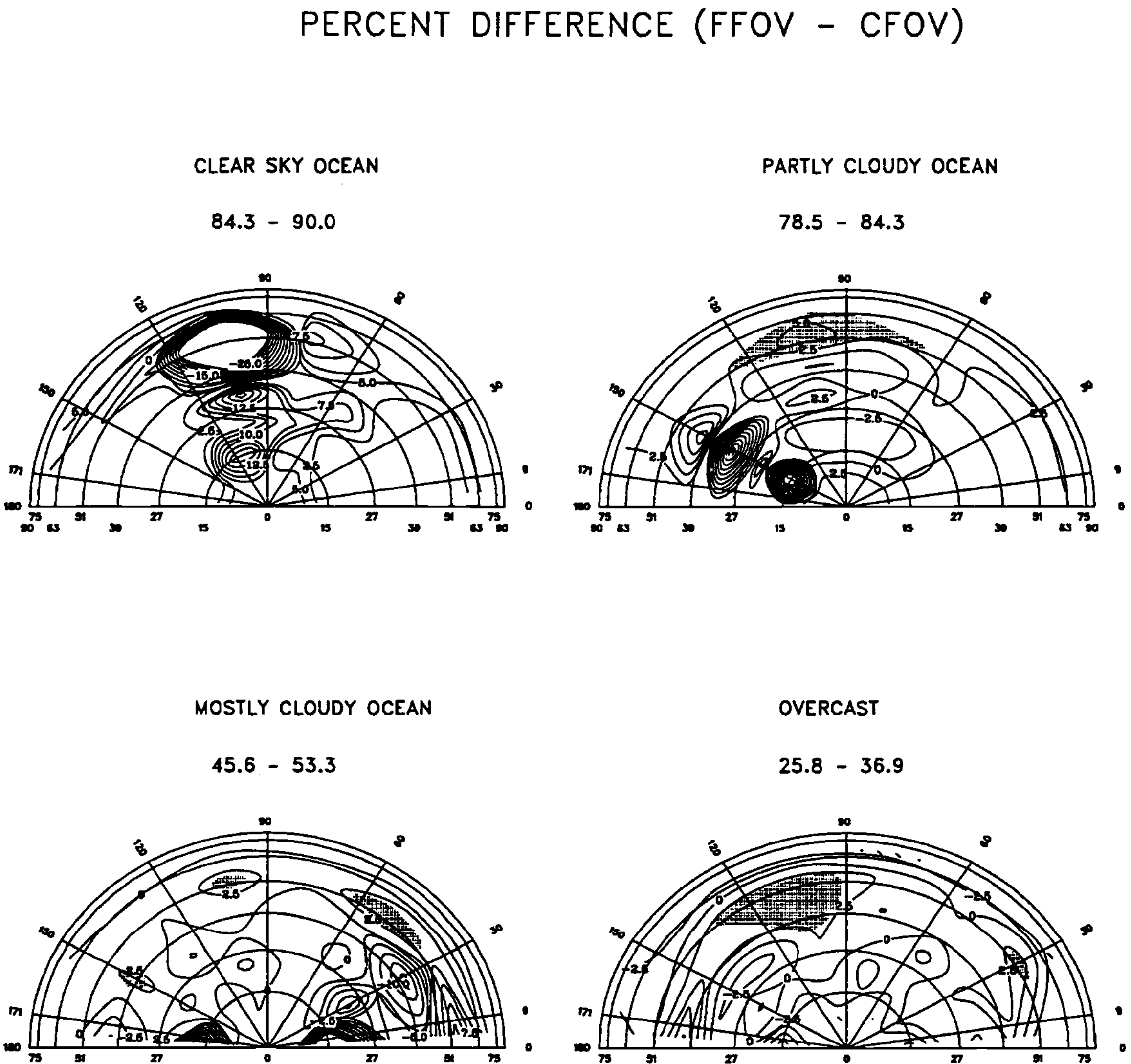

Figure 5.15 Same as Fig. 5.14 but for the solar zenith angle bins which had the smallest domains for which the differences were significant at the 90% confidence level.

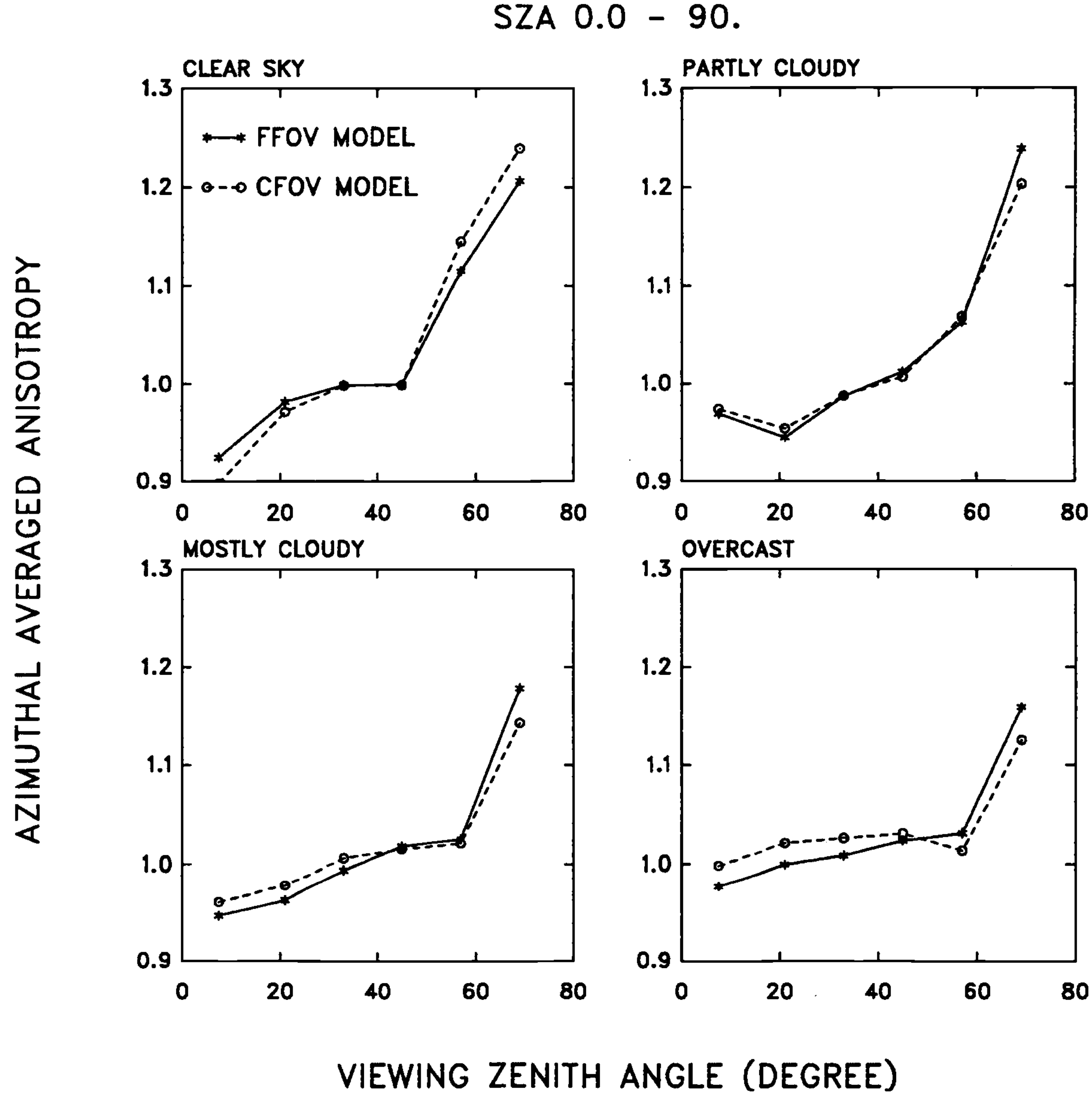

Figure 5.16 Azimuthally averaged shortwave anisotropic factors for the FFOV and CFOV observations obtained with the FFOV thresholds. The azimuthally averaged anisotropic factors were averaged for all solar zenith angle bins.

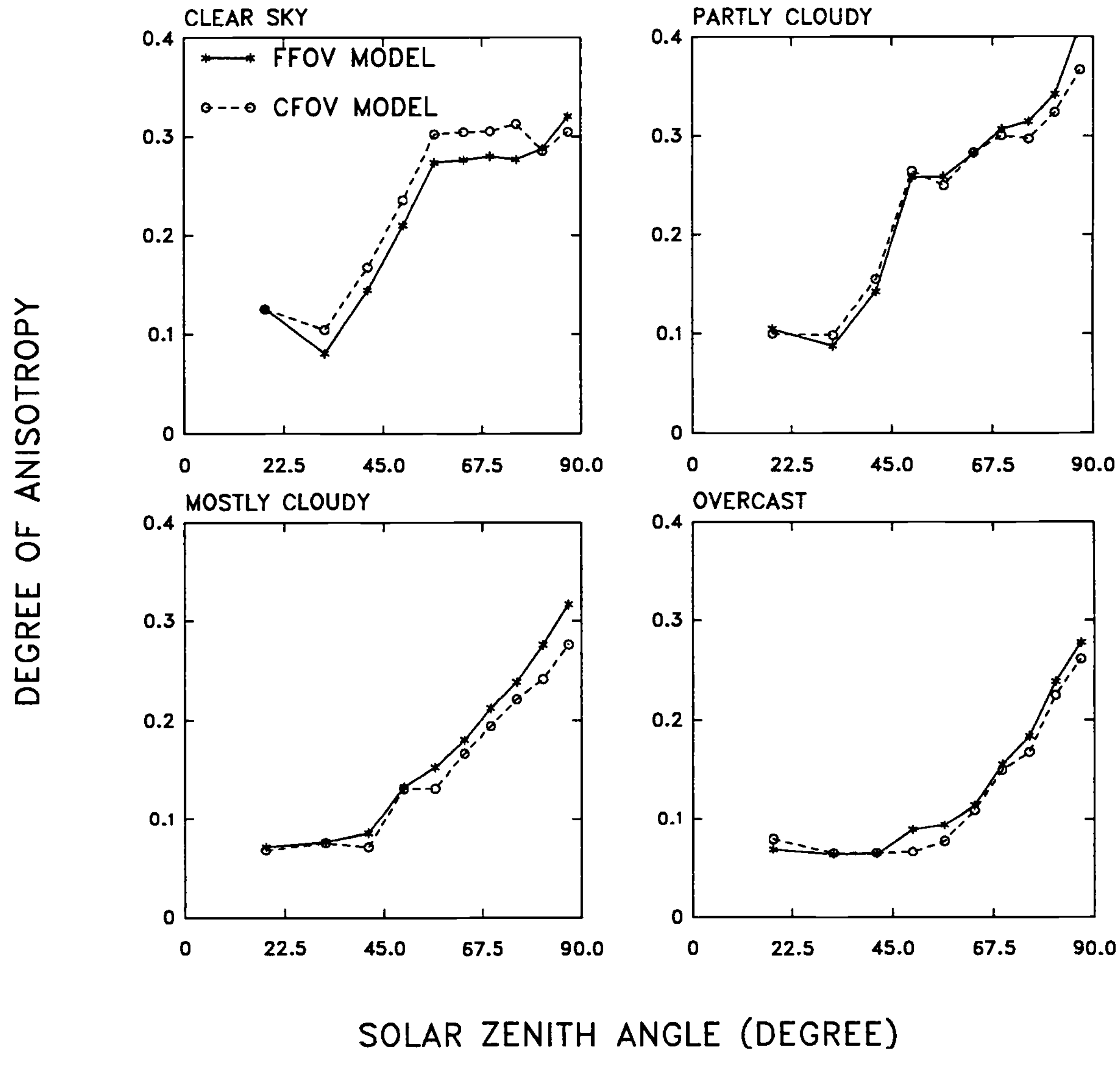

Figure 5.17 Degree of shortwave anisotropy for the FFOV (solid line) and CFOV (dashed line) observations obtained using the FFOV thresholds.

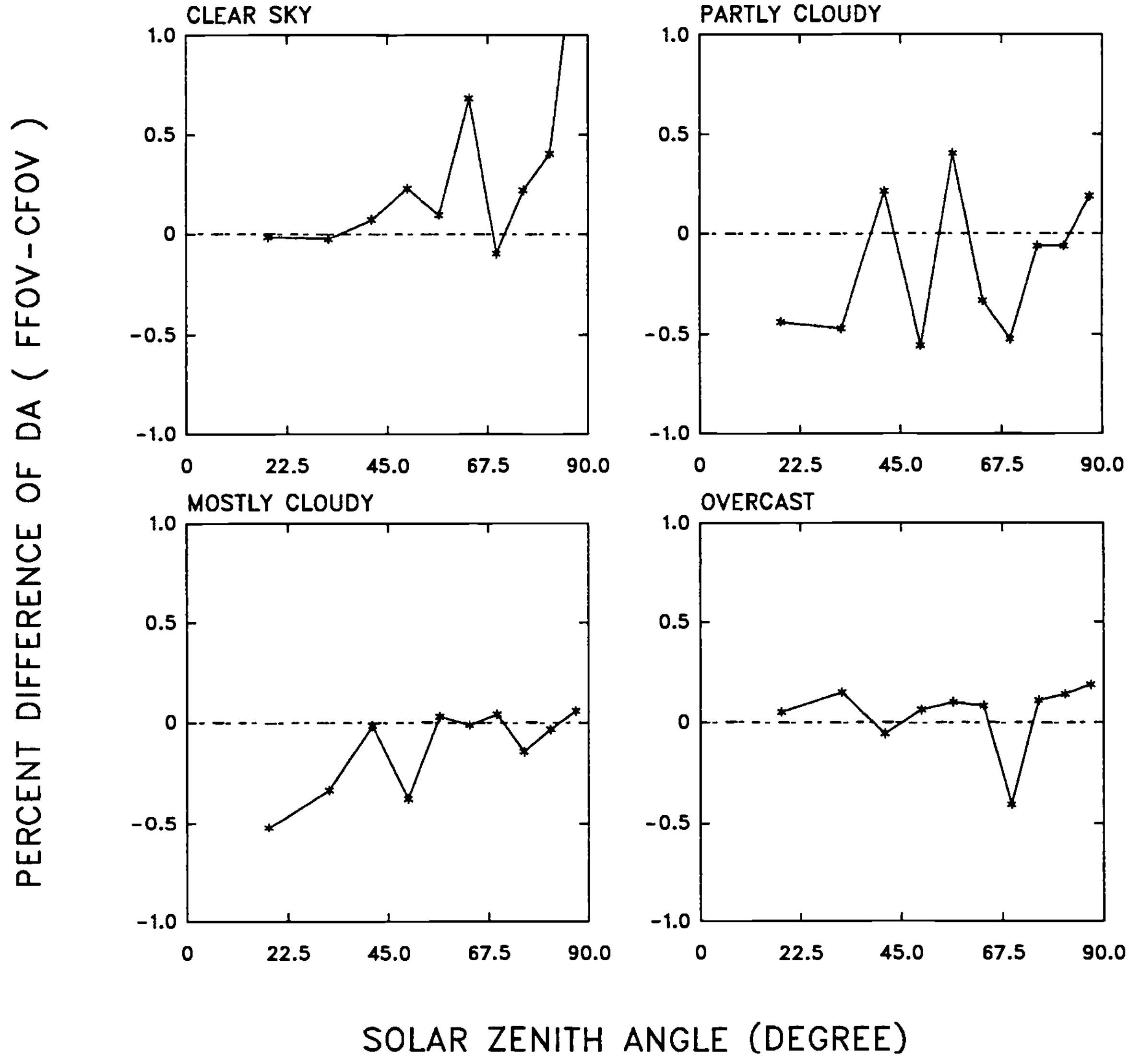

Figure 5.18 Percent difference in the degree of shortwave anisotropy for the FFOV and CFOV observations using the FFOV thresholds.

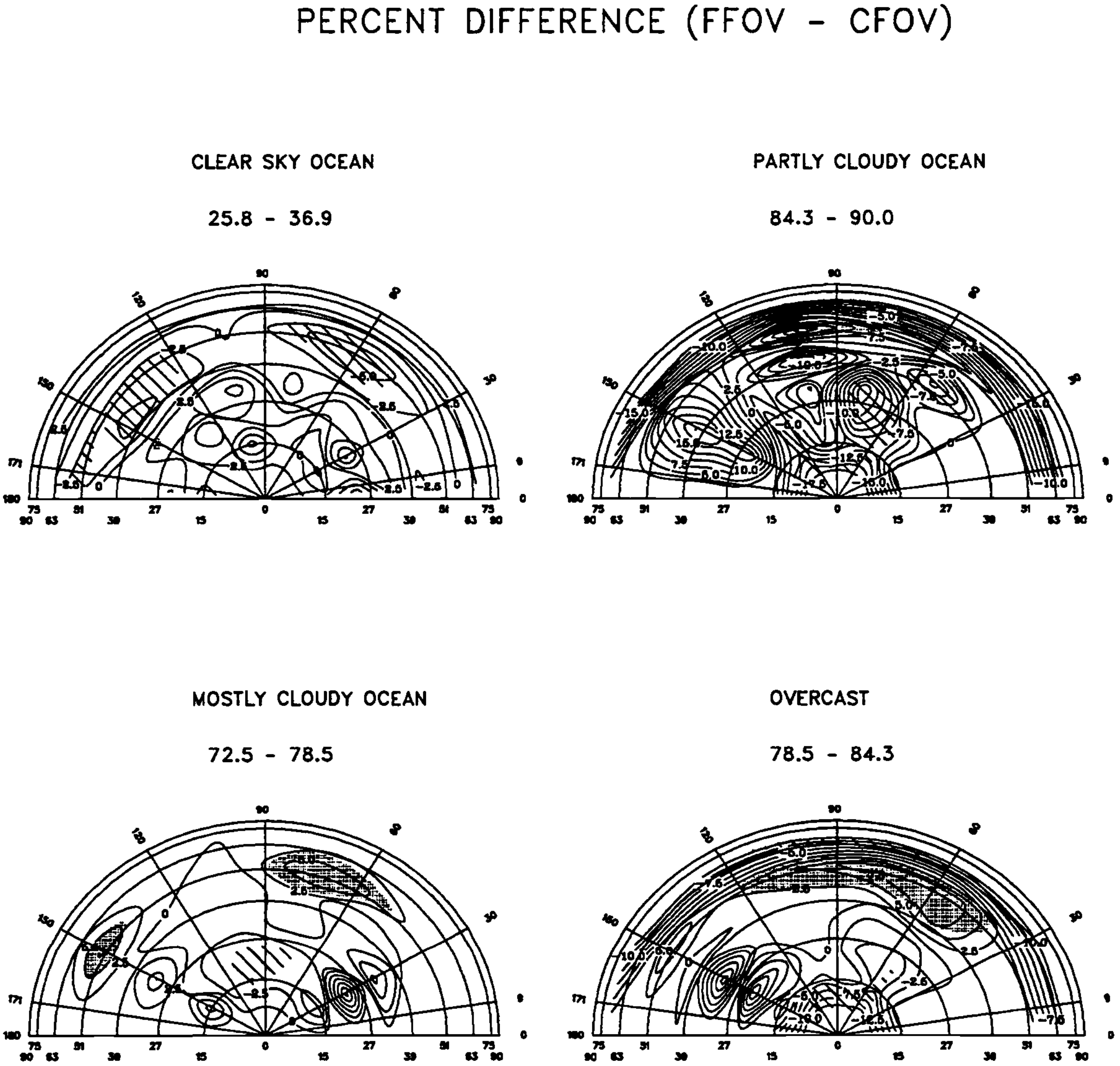

Figure 5.19 Same as Fig. 5.14 but the FFOV and CFOV pseudo-ADMs were constructed using the CFOV thresholds.

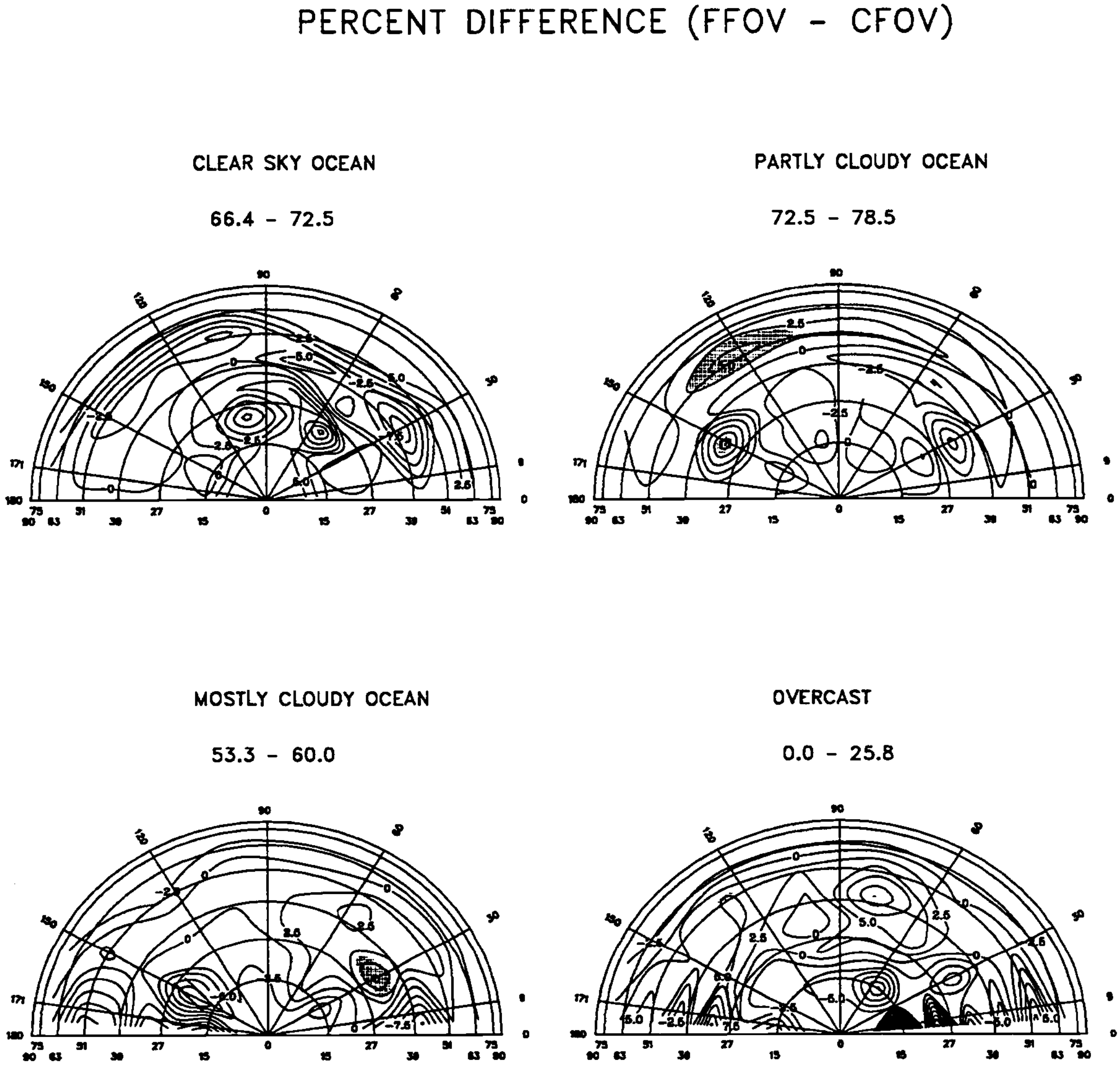

PERCENT DIFFERENCE (FFOV - CFOV)

CLEAR SKY OCEAN

66.4 - 72.5

PARTLY CLOUDY OCEAN

72.5 - 78.5

MOSTLY CLOUDY OCEAN

53.3 - 60.0

OVERCAST

0.0 - 25.8

Figure 5.20 Same as Fig. 5.15 but the FFOV and CFOV pseudo-ADMs were constructed using the CFOV thresholds.

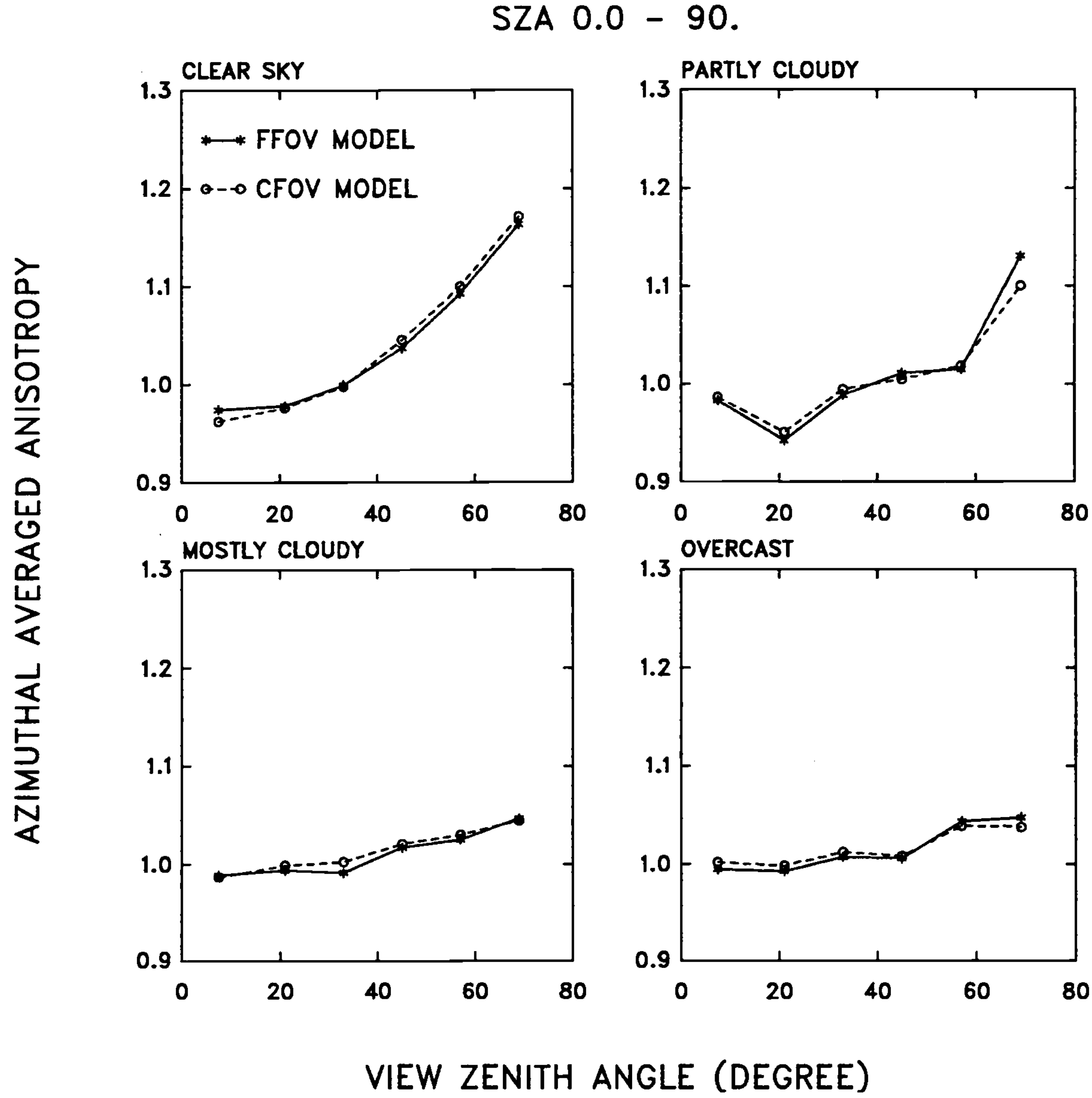

Figure 5.21 Azimuthally averaged shortwave anisotropic factors for the FFOV and CFOV observations obtained with the CFOV thresholds. The azimuthally averaged anisotropic factors were averaged for all solar zenith angle bins.

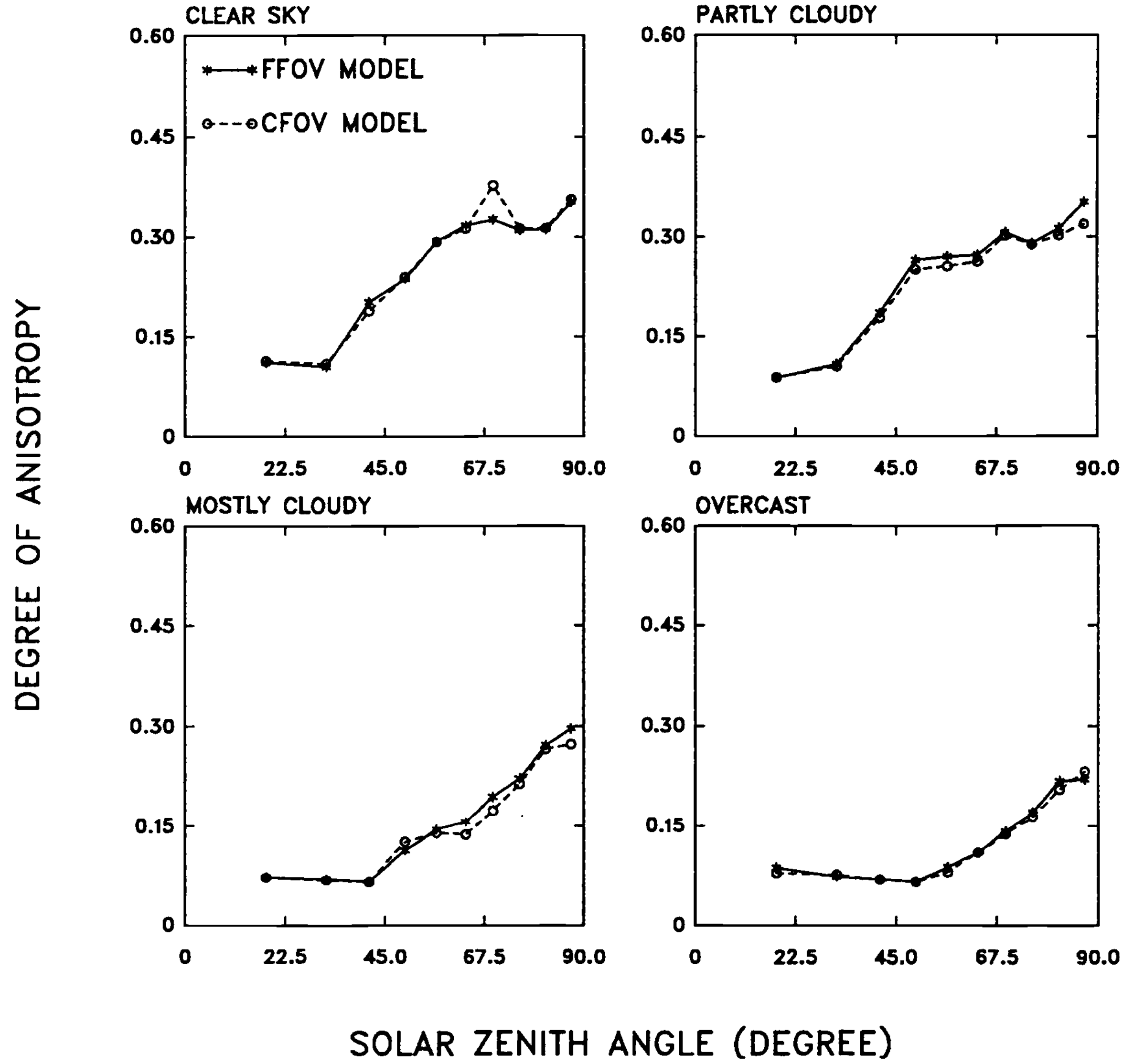

Figure 5.22 Degree of shortwave anisotropy for the FFOV (solid line) and CFOV (dashed line) observations obtained using the CFOV thresholds.

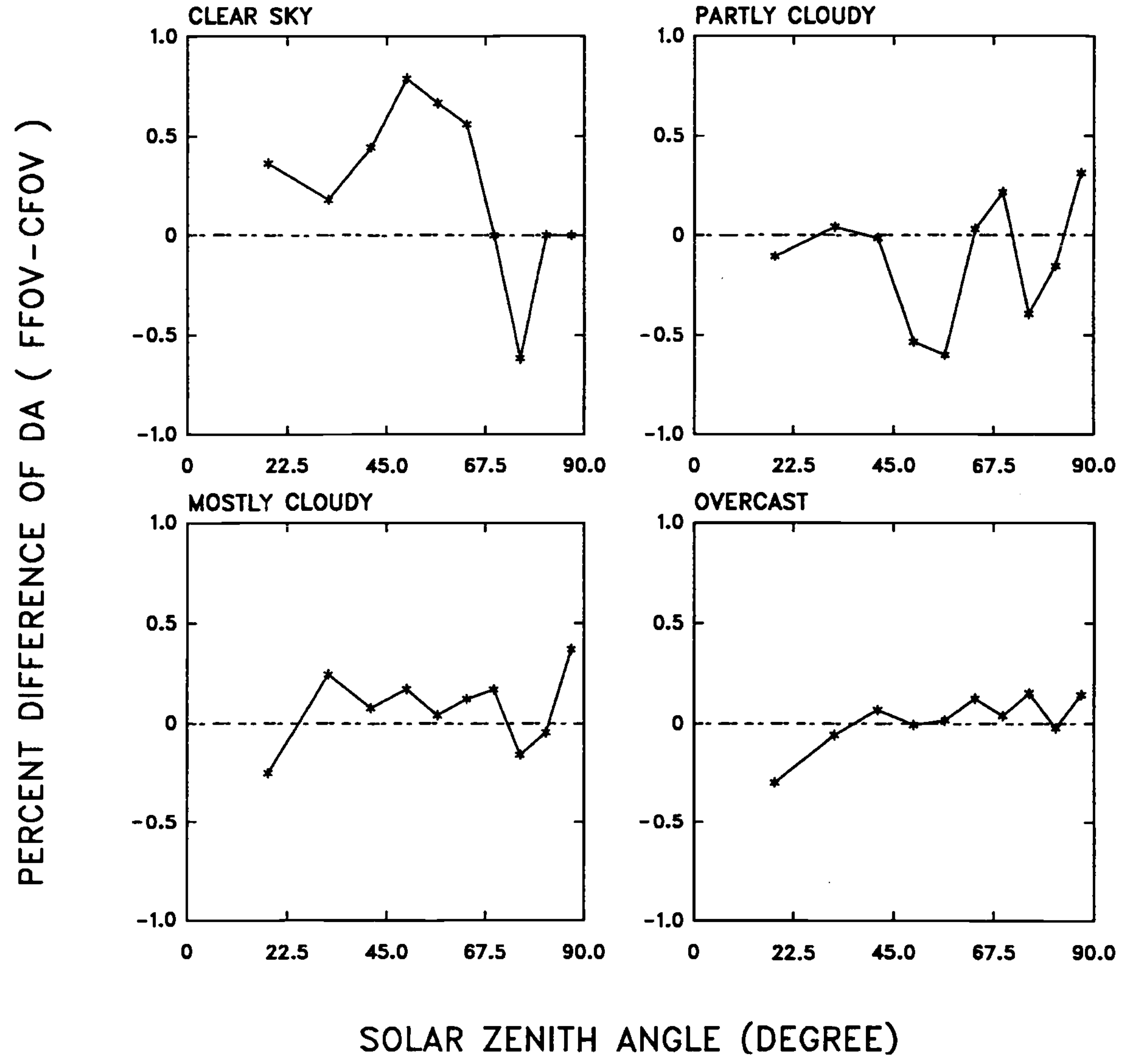

Figure 5.23 Percent difference in the degree of shortwave anisotropy for the FFOV and CFOV observations using the CFOV thresholds.

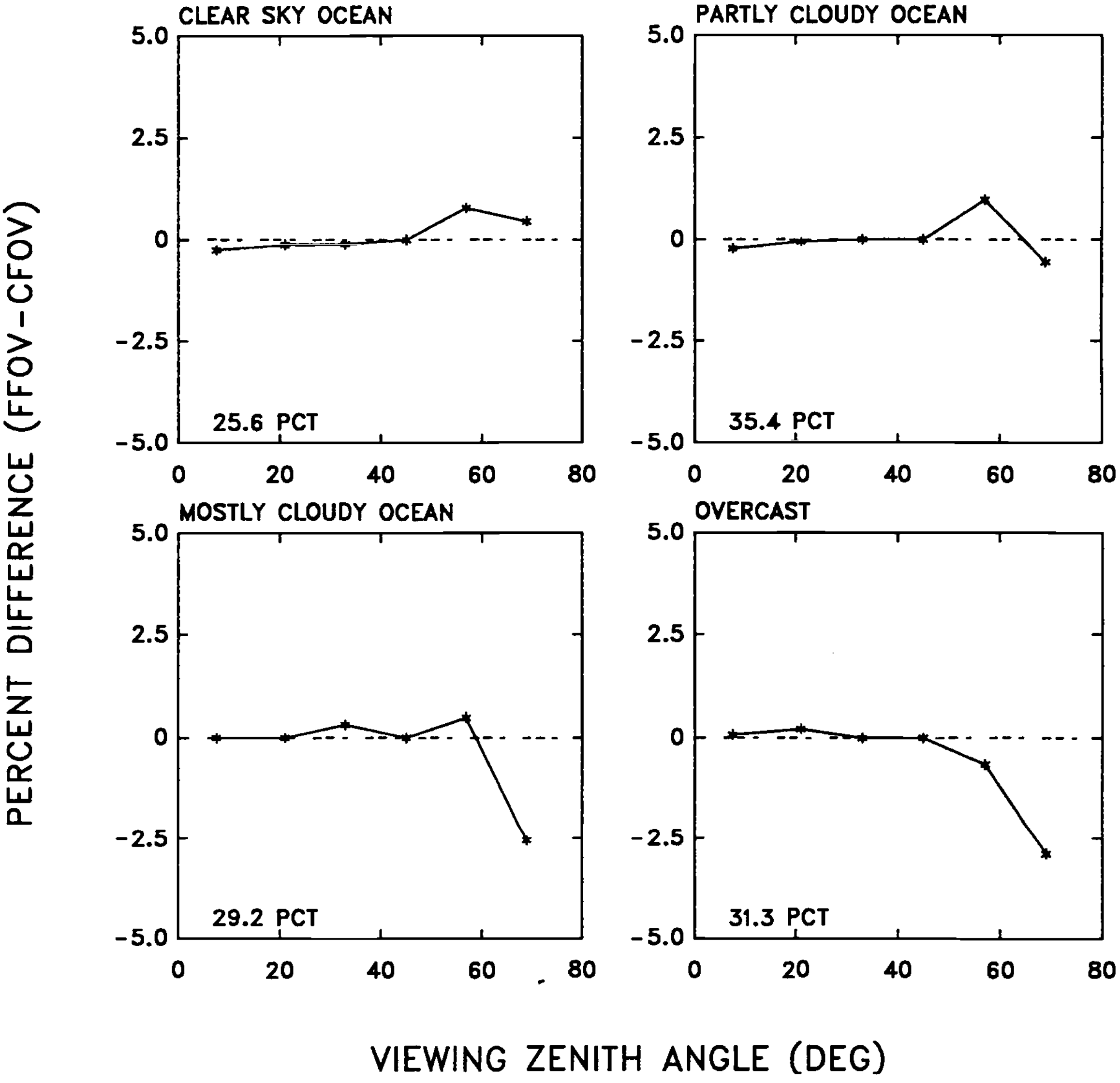

Figure 5.24 Percent difference in the degree of longwave anisotropy for the FFOV and CFOV observations using the FFOV threshold.

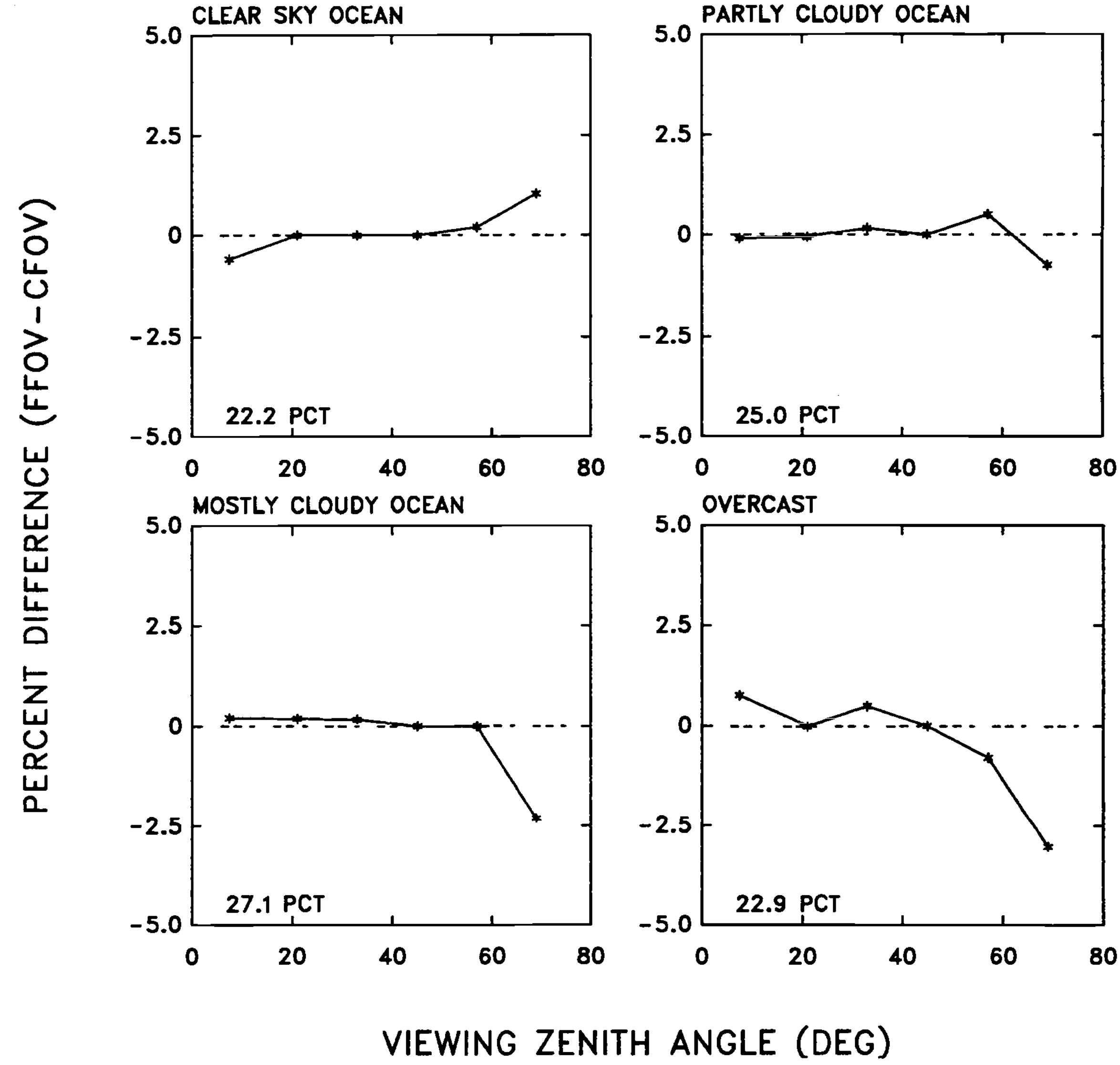

Figure 5.25 Percent difference in the degree of longwave anisotropy for the FFOV and CFOV observations using the CFOV threshold.

6. ANGULAR DEPENDENCE MODELS BASED ON THRESHOLD SCENE IDENTIFICATION METHODS

6.1 Introduction

The ERBE inversion process, which includes the ERBE ADMs and the MLE cloud scene identification method, is a primary source of error in the estimation of radiative fluxes (Wielicki and Green, 1989; Baldwin and Coakley, 1991; Suttles et al., 1992). Davies (1984) pointed out that because of the difficulty of distinguishing between broken and continuous cloud cover from coarse spatial resolution scanner measurements, estimates of fluxes were likely to be in error. Using Monte Carlo simulations of radiative transfer for simple models of broken clouds, he found that for nadir and limb scanner measurements, misidentification of the scene could cause as much as a factor of 2 error in the estimated radiative flux for certain types of scenes. In ERBE, fields of view were identified by the ERBE MLE scene identification. Then, ADMs associated with particular scene types were applied to convert the observed radiance to a total flux. Davies (1988) calculated the global average albedo by averaging radiative fluxes, which were estimated using the ERBE algorithm, at a particular view zenith angle for a sufficient length of time ($\sim$ 3 months). He found that the global average albedo depended on view zenith angle. This finding was confirmed by Suttles et al. (1992) who estimated the global average albedo and longwave fluxes based on Nimbus-7 ERB scanning radiometer measurements using the ERBE inversion algorithm. Growths of the global average albedo and longwave fluxes with increasing satellite zenith angle were obtained. The global albedo estimated on the basis of nadir observations was about 0.26 and it was about 0.29 for limb observations as was shown in Fig. 1.4.

In the previous chapters, the ERBE MLE method was shown to have view zenith angle dependent errors in scene identification. Part of the errors may have been caused by effects due to cloud sides. Part of the errors were evidently caused by the effect of cloud clustering combined with increasing field of view size from nadir to limb. ERBS scanning radiometer measurements and the ERBE MLE scene identification were used to construct angular dependence models (ADMs). The ADMs exhibited a significant spatial-scale dependence. This spatial scale dependence was attributed to errors in the scene identification. Threshold scene identification methods were developed to remove the apparent view angle dependence of the scene identification errors. The threshold methods were based on the assumption that the ERBE MLE scene identification was correct at nadir. A bispectral threshold method was developed based on the nadir identification so that CFOV observations had frequencies of occurrence which were constant with view zenith angle for the four cloud cover categories. ADMs constructed using the threshold scene identification were found to be nearly invariant to spatial scale. These ADMs are hereafter referred to as threshold-ADMs.

Requiring the ADMs to be independent of spatial scale is a necessary but not a sufficient condition by which to assess the adequacy of the models. Wielicki and Green (personal communication, 1993) suggest that for ADMs to be judged as being better than the ERBE ADMs, they must have the following properties: 1) they must be less sensitive to instrument spatial resolution; 2) they must obey reciprocity more closely; 3) they must produce a global average albedo that is less dependent on the view zenith angle used to obtain the estimate and 4) they must produce smaller standard deviations between ERBE scanner/non-scanner observations at satellite altitude. In chapter 5, the threshold-ADMs were shown to have less spatial scale dependence than those constructed using the ERBE MLE scene identification. In the following, the results of the reciprocity and global average albedo tests will be presented for the threshold-ADMs. In this investigation, observations for only three months were used. Due to the restriction in viewing geometry imposed by the satellite orbit, there are substantial numbers of angular bins with no observations. Since the ADMs with a full range of angular bins are required for scanner/non-scanner comparisons, the comparisons will be left for future work.

6.2 Reciprocity

The Helmholtz Principle of Reciprocity for a plane-parallel atmosphere is discussed by Chandrasekhar (1960). This principle states that the product of the cosine of the angle of reflection and the reflected radiance is unaltered if the angles and radiances of the incident and reflected light are interchanged, i.e.,

$$\mu_0 I(0, \mu_0, \mu, \phi) = \mu I(0, \mu, \mu_0, \phi) \ . \tag{6.1}$$

In terms of the albedo α and anisotropic factor R, reciprocity is given by

$$R(\mu_0, \mu, \phi)\alpha(\mu) = R(\mu, \mu_0, \phi)\alpha(\mu_0) \tag{6.2}$$

where α is defined in (3.7) and R is defined in (3.13). (6.2) states that the product of anisotropy and albedo must be the same when the solar zenith angle and the view zenith angle are interchanged (Suttles et al., 1988).

Due to restrictions imposed by the satellite orbit, there are always angles at which there are few or even no observations. The reciprocity principle can be used to obtain anisotropic factors for such angles. Reciprocity was used to complete some of the ERBE ADMs (Suttles et al., 1988, 1989). The reciprocity test used in this thesis follows Green et al. (1990). The distance, *d*, between the anisotropic factor and its value obtained from the application of reciprocity, $R^*(\mu_0, \mu, \phi)$, is given by

$$d^2(R, R^*) = \sum_{i=1}^{10} \sum_{j=1}^{7} \sum_{k=1}^{8} C_{j,k}(R(\mu_{0i}, \mu_j, \phi_k) - R^*(\mu_{0i}, \mu_j, \phi_k))^2 \tag{6.3}$$

where $d \geq 0$, and $C_{j,k}$ is the weighting factor used in the normalization condition. $C_{j,k}$ is given by

$$C_{j,k} = \pi^{-1}(\phi_{k+1} - \phi_k)(\sin^2\theta_{j+1} - \sin^2\theta_j) \ . \tag{6.4}$$

Table 6.1 Distance between the original ADMs and the reciprocal ADMs for the ERBE ADMs, the FFOV threshold-ADMs, and CFOV threshold-ADMs for clear, partly cloudy, mostly cloudy oceans and overcast scenes.

Scene type	ERBE ADMs	FFOV ADMs	CFOV ADMs
Clear ocean	0.540	0.515	0.479
Partly cloudy ocean	0.415	0.364	0.266
Mostly cloudy ocean	0.103	0.087	0.067
Overcast	0.058	0.067	0.040

Index i (= 1, ..., 10) refers to the solar zenith angle bin, index j (= 1, ..., 7) refers to the view zenith angle bin, and index k (= 1, ..., 8) refers to the azimuth angle bin. By definition, if the models are reciprocal, then the distance $d(R, R^*) = 0$. Large distances mean that the models tend to violate reciprocity. Using this measure of distance, Green et al. (1990) showed that the ERBE ADMs had substantial violations of reciprocity.

The distances between the original ADMs and the reciprocal ADMs were calculated for the ERBE ADMs, the FFOV threshold-ADMs and the CFOV threshold-ADMs for the three cloud cover categories over ocean and overcast scenes. The results are listed in Table 6.1. Table 6.1 shows that all of the models violate reciprocity to some degree. These violations generally decreased with increasing cloudiness from clear sky to overcast. Both the FFOV and CFOV ADMs gave improvements in reciprocity for all but one of the cloud categories. The FFOV ADMs showed a larger distance (0.067) for overcast scenes than that for the ERBE ADMs (0.058). The CFOV threshold-ADMs for overcast scenes were the closest to fulfilling reciprocity. The ERBE ADMs for clear oceans were the furthest from fulfilling reciprocity.

6.3 Viewing Geometry Dependence Of The Global Average Albedo

The planetary albedo is defined as the ratio of the radiative flux reflected by the earth to the incident solar flux at a given solar zenith angle. It is given by

$$\alpha(\theta_0) = \frac{\pi F(\theta_0)}{\cos\theta_0 S_0} \tag{6.5}$$

where $\pi F(\theta_0)$ is the total reflected shortwave flux at the top of the atmosphere, S_0(= 1365 Wm^{-2}, Suttles et al., 1988) is the solar constant corrected for the Earth-Sun distance and θ_0 is the solar zenith angle.

The global average albedo was obtained as follows: Each field of view was identified as containing a particular scene type and the associated ADM was applied to convert the observed radiance to a total flux. If the scene identification and the associated ADMs were correct, then the global average albedo obtained by averaging observations at a particular view zenith angle for a sufficient length of time ($\sim$ 3 months) should have been independent of the view zenith angle. Davies (1988) and Payette (1989) reported that the global average albedo obtained in this fashion depended dramatically on view zenith angle. Suttles et al. (1992) confirmed the earlier findings.

The global average albedo was calculated using the threshold identification methods. Because of the satellite orbit there were no observations for some viewing geometries. Consequently, pseudo-ADMs as described in chapter 4 were used. Before testing the ability of the threshold-ADMs to reduce the view zenith angle dependence of the global average albedo, the effect of allowing for bins with no observations was examined.

6.3.1 Effect Of ADM Normalization On The Estimated Albedo

The albedo given by (6.5) can be expressed in terms of the anisotropic factor as follows

$$\alpha(\theta_0) = \frac{\pi I(\theta_0, \theta, \phi)/R(\theta_0, \theta, \phi)}{\cos\theta_0 S_0} \tag{6.6}$$

where $I(\theta_0, \theta, \phi)$ is the radiance, and again, θ_0, θ, ϕ are the solar zenith, view zenith and relative azimuth angles. Using the finite angular bins described in chapter 3, the discrete form of (6.6) is given by

$$\alpha(\theta_{0i}) = \frac{\pi I(\theta_{0i}, \theta_j, \phi_k)/R(\theta_{0i}, \theta_j, \phi_k)}{\mu_{0i} S_0} \tag{6.7}$$

where i = 1, 2, ..., 10; j = 1, 2, ..., 7; k = 1, 2, ..., 8 and $\mu_{0i} = \cos\theta_{0i}$. The anisotropic factor $R(\theta_{0i}, \theta_j, \phi_k)$ is given by

$$R(\theta_{0i}, \theta_j, \phi_k) = \frac{\pi I(\theta_{0i}, \theta_j, \phi_k)}{\sum\limits_{m=1}^{8} (\phi_{m+1} - \phi_m) \sum\limits_{n=1}^{7} (\sin^2\theta_{n+1} - \sin^2\theta_n) I(\theta_{0i}, \theta_n, \phi_m)} \, . \tag{6.8}$$

It must satisfy the normalization condition

$$\pi^{-1} \sum_{k=1}^{8} (\phi_{k+1} - \phi_k) \sum_{j=1}^{7} (\sin^2\theta_{j+1} - \sin^2\theta_j) R(\theta_{0i}, \theta_j, \phi_k) = 1 \, . \tag{6.9}$$

The spherical albedo α_s was used to show the view zenith angle dependence of albedo. Here, α_s is a weighted average for the planetary albedo $\alpha(\theta_0)$ over all solar positions. It is given by

$$\alpha_s = \frac{\int_0^1 \alpha(\mu_0)\mu_0 d\mu_0}{\int_0^1 \mu_0 d\mu_0} \, . \tag{6.10}$$

In discrete form, (6.10) is given by

$$\alpha_s = \frac{\sum\limits_{i=1}^{10} \alpha_i \mu_{0i} \Delta\mu_0}{\sum\limits_{i=1}^{10} \mu_{0i} \Delta\mu_0} \tag{6.11}$$

where, again, μ_{0i} is the cosine of the solar zenith angle, i = 1, 2 ,..., 10 for ten solar zenith angle bins, $\Delta\mu_0 = 0.1$ and $\sum\limits_{i=1}^{10} \mu_{0i} \Delta\mu_0 = \frac{1}{2}$.

In the development of the threshold-ADMs, approximately 25% of the angular bins were missed due to the idiosyncracies of the ERBS satellite orbit and the view zenith angle cutoff used here in the analysis. Obviously, owing to the normalization condition, the values of the radiances used for the bins with no observations will affect all of the anisotropic factors. Fig. 6.1 shows the spherical albedo derived using the ERBE full ADMs and the ERBE pseudo-ADMs derived from ERBS scanner observations for September, 1986. Only ocean and overcast scenes as identified by the ERBE MLE were used in the calculation. Full ADMs were constructed by using the ERBE anisotropic factors for bins with no observations. Pseudo-ADMs were constructed by using only those angular bins for which there were sufficient observations in the CFOV data set. In this thesis, the minimum number of observations for each angular bins was set to be eight. The pseudo-ADM contained zeros in the angular bins with no observations. Both the full and pseudo-ADMs were normalized using the condition

$$\frac{1}{\pi}\int_0^{2\pi} d\phi \int_0^1 R(\mu_0, \mu, \phi)\mu d\mu = 1 \; . \tag{6.12}$$

As is shown in Fig. 6.1, both the ERBE pseudo-ADMs and the ERBE full ADMs lead to a growth in the estimated albedo from nadir to limb. The albedo derived using the pseudo-ADMs increased by about 0.055 (or 18.3%) from nadir to limb. The growth of albedo was much smaller for the ERBE full ADMs, about 0.023 (or 7.9%). These results were consistent with those obtained by Suttles et al. (1992). In their study, the albedo increased by about 10% from nadir to limb when the ERBE inversion algorithm was applied to Nimbus-7 ERB scanner measurements. Compared with the variability in albedo, about 0.005, there were no significant differences between the estimated albedos derived from the two sets of ADMs for viewing zenith angles less than 45°. The pseudo normalization seems to provide a satisfactory solution to the problem of bins with no observations.

For large viewing zenith angles, the albedos of full and pseudo ADMs differed significantly. The differences could be explained as follows: At larger view zenith angles the population of fields of view identified by the ERBE MLE as being overcast was higher than that identified as being clear (Fig. 5.2). Since radiances reflected from overcast scenes were much larger than those reflected from clear scenes, radiances from overcast scenes contributed more to the spherical albedo. As shown in Fig. 6.2, however, for overhead sun, limb-darkening occurs for radiation reflected by overcast scenes. Through normalization (6.12), this limb-darkening was amplified in the pseudo-ADMs. In the calculation of the spherical albedo α_s (6.10), the planetary albedo $\alpha(\theta_0)$ for overhead sun had the largest weight ($\mu_0 = 0.95$). As a result, the spherical albedo obtained using the pseudo-ADMs grew faster with increasing view zenith angle than that obtained using the ERBE full ADMs. In summary, with pseudo normalization, there were no significant differences in the estimated global average albedo.

The ERBE MLE was prone to scene identification errors, particularly at large view zenith angles. These scene identification errors caused the global average albedo to exhibit greater view zenith angle dependence at large view zenith angles when derived using pseudo ADMs than when using the ERBE full ADMs.

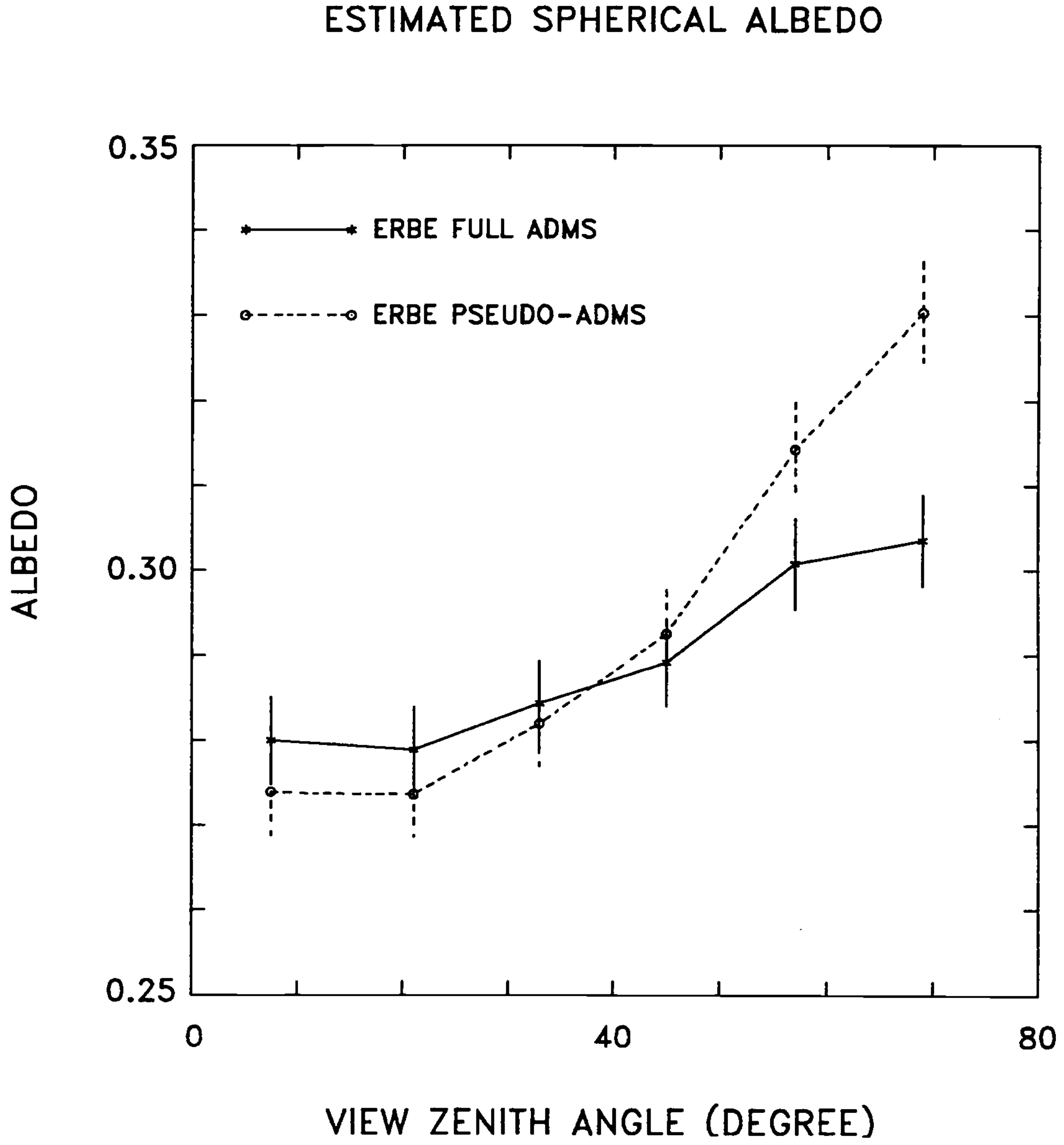

Figure 6.1 Effect of using different values of the mean radiance for angular bins with no observations. See the text for the definitions of the full ADMs and pseudo-ADMs. The results were calculated using ERBS observations for September, 1986. The vertical bars represent one standard deviation of the mean on each side of the curves.

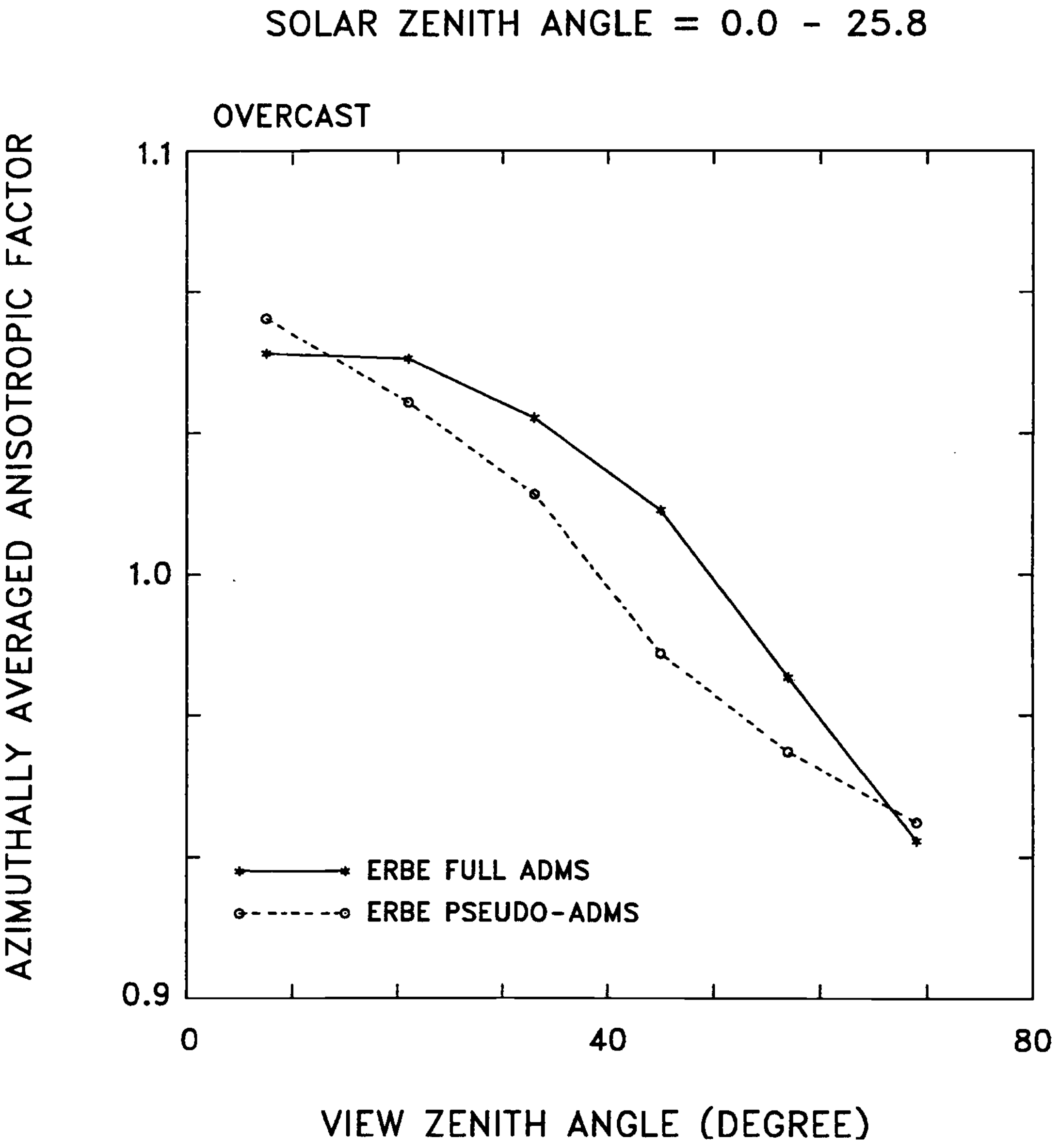

Figure 6.2 Azimuthally averaged anisotropic factors for overhead sun obtained using the ERBE full ADMs (solid line) and ERBE pseudo-ADMs (dashed line) for scenes identified by the ERBE MLE as being overcast.

6.3.2 Angular Dependence Of Estimated Albedos

The FFOV and CFOV ADMs and associated threshold scene identification methods were used to estimate the global average albedo following the procedures described by Payette (1989). Again, ADMs are denoted as full ADMs when the angular bins with no observations in the FFOV and/or the CFOV data sets were filled using the radiances from which the original ERBE ADMs were derived. The pseudo-ADMs represent the ADMs which were developed simply by setting the values in the angular bins with no observations to zero. The results presented in this section were calculated using ERBS scanner measurements for September, 1986. For the purpose of studying the view zenith angle dependence of the albedo, diurnal corrections which are necessary for obtaining unbiased estimates of the average albedo (Smith et al., 1986) are not considered. Also, due to the ERBS orbit, observations from polar regions are not included. Moreover, only ocean scenes are used for calculating the global average albedo. Consequently, the albedo derived here is not directly comparable to that obtained by ERBE (Barkstrom et al., 1989; Gibson et al., 1990).

The ERBS observations were identified by the ERBE MLE method, the FFOV and the CFOV bispectral threshold methods. The spherical albedos were then calculated using (6.10) for both the full ADMs and pseudo-ADMs of the ERBE, the FFOV and the CFOV models. Fig. 6.3 shows the estimated spherical albedos as a function of view zenith angle. The vertical bars on the curves represent one standard deviation of the mean on each side of the curves. The ERBE spherical albedos (solid lines) increased markedly with increasing viewing zenith angle. The growths were about 0.023 (or 7.9%) for the full ADMs, and about 0.055 (or 18.3%) for the pseudo–ADMs. With the variability in albedo of the order $\Delta\alpha_s = 0.005$, the two-sided t test is about 0.0082 at the 90% confidence level. Thus, the view angle dependence of the ERBE spherical albedos is clearly statistically significant.

The figure shows weaker dependence on viewing angle for the albedos derived using the FFOV and the CFOV algorithms. For the FFOV models, the corresponding results were 0.017 (or 5.6%) for the full ADMs and 0.023 (or 7.7%) for the pseudo-ADMs. Using the CFOV algorithm, the differences between the albedos at nadir and those at the limb were about 0.008 (or 2.8%) for the full ADMs and about 0.0012 (or 0.4%) for the pseudo-ADMs. The CFOV albedos do not exhibit a view zenith angle dependence for both the full and pseudo-ADMs based on a two-sided *t* test at the 90% confidence level. For the same criteria, the FFOV albedos exhibit a dependence. Omitting the value of albedo for the largest view zenith angle bin, however, the FFOV albedos also appear to be independent of viewing angle. With the albedo for the largest view zenith angle bin omitted, the difference between the FFOV albedos at nadir and those at the limb is reduced to 0.001 for the full ADMs and 0.008 for the pseudo-ADMs. These differences were statistically insignificant.

In summary, using the FFOV and the CFOV threshold-ADMs and associated threshold scene identification methods, the view angle dependence of the global average albedo was significantly reduced compared with that for the ERBE ADMs. Using the CFOV algorithm, which included the CFOV threshold scene identification and the CFOV ADMs, a factor of 3 improvement in the reduction of view angle dependence was obtained for the estimated albedo. The FFOV algorithm, which included the FFOV threshold scene identification and the FFOV ADMs, gave a factor of 2 improvement.

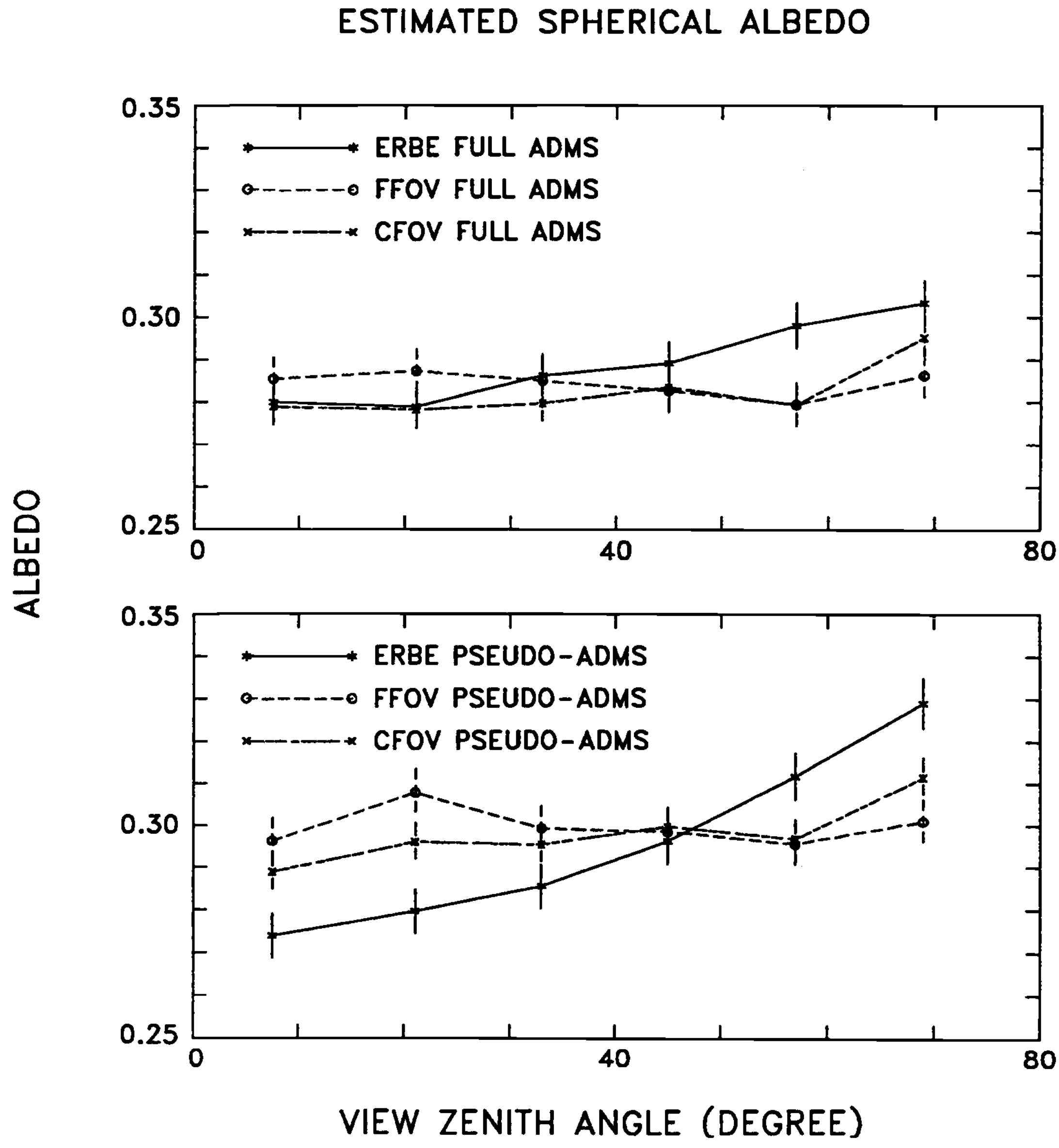

Figure 6.3 Global average spherical albedos derived using the ERBE, the FFOV and CFOV ADMs and associated scene identification methods. The calculations were made for the full ADMs (upper diagram) and the pseudo-ADMs (lower diagram) using ERBS scanner observations for September, 1986.

6.4 Discussion

A mean value of the global average albedo was calculated as follows

$$\alpha_{\text{global}} = \frac{1}{6}\sum_{i}^{6} \alpha_s(\mu_i) \tag{6.13}$$

where the index i is for six view zenith angles and μ_i is the cosine of the ith view zenith angle. Table 6.2 gives the global average albedos derived using the ERBE, the FFOV and CFOV algorithms using global ERBS scanner data for September, October, November, 1986. Clearly, using the CFOV algorithm, there is a significant increase of about 0.010 (or 3.4%) in the estimated global albedo compared with that derived using the ERBE algorithm. Using a time-average solar insolation of 1365/4 = 341 Wm^{-2} (Suttles et al., 1988), the 3.4% increase in albedo is equivalent to a shortwave flux of (0.010)×(341) = 3.41 Wm^{-2}. In other words, there is about 3.41 Wm^{-2} more solar radiation reflected back to space simply due to the change in the inversion algorithm. The estimates of average longwave fluxes obtained using different algorithms are almost equal. Differences are less than 1.6 Wm^{-2}(or 0.7%). Table 6.2 also shows the net radiations obtained based on the estimated global average albedo and longwave fluxes. Results show that the imbalance in the estimated net radiation budget found by ERBE may be significantly smaller using the threshold ADMs.

Table 6.2 Global average spherical albedos and longwave fluxes derived using the ERBE, the FFOV and CFOV algorithms. The results are derived from ERBS scanner data for September, October, November, 1986.

	ERBE	CFOV	FFOV
Albedo	0.289	0.299	0.296
Longwave Fluxes (Wm^{-2})	239.331	240.071	240.906
Net Radiation (Wm^{-2})	3.298	-0.855	-0.666

Fig. 6.4 shows the frequencies of occurrence and the differences between mean reflected radiances obtained using the ERBE MLE and the FFOV threshold scene identification methods for the four cloud categories. For the FFOV observations at off nadir angles, there were significant differences in the frequencies of occurrence for cloud scene types identified using the FFOV threshold scene identification method compared with those identified using the ERBE MLE method. Using the FFOV threshold method, the frequencies of occurrence for overcast scenes decreased with increasing view zenith angle while those for partly cloudy and mostly cloudy scenes increased with view zenith angle. This indicates that a large portion of overcast scenes at off nadir angles identified by the ERBE MLE were identified as mostly cloudy or partly cloudy scenes by the FFOV threshold method. The transfer of overcast scenes to partly or mostly cloudy scenes led to increases in the average reflected radiances for partly cloudy, mostly cloudy and overcast scenes at off nadir angles. These increases were shown in the right column of Fig. 6.4. The increase in the reflected radiances for cloudy scenes was about 5%, which, in turn, gave a 5% increase in the reflected radiative flux. Combining (6.5) and (6.10), a relationship between the global average albedo and the reflected radiative flux could be obtained

$$\alpha_s = \frac{\int_0^1 \frac{\pi F(\mu_0)}{\mu_0 S_0} \mu_0 d\mu_0}{\int_0^1 \mu_0 d\mu_0} . \tag{6.14}$$

It was clear that a 5% increase in the reflected radiative flux would lead to a 5% increase for global average albedo.

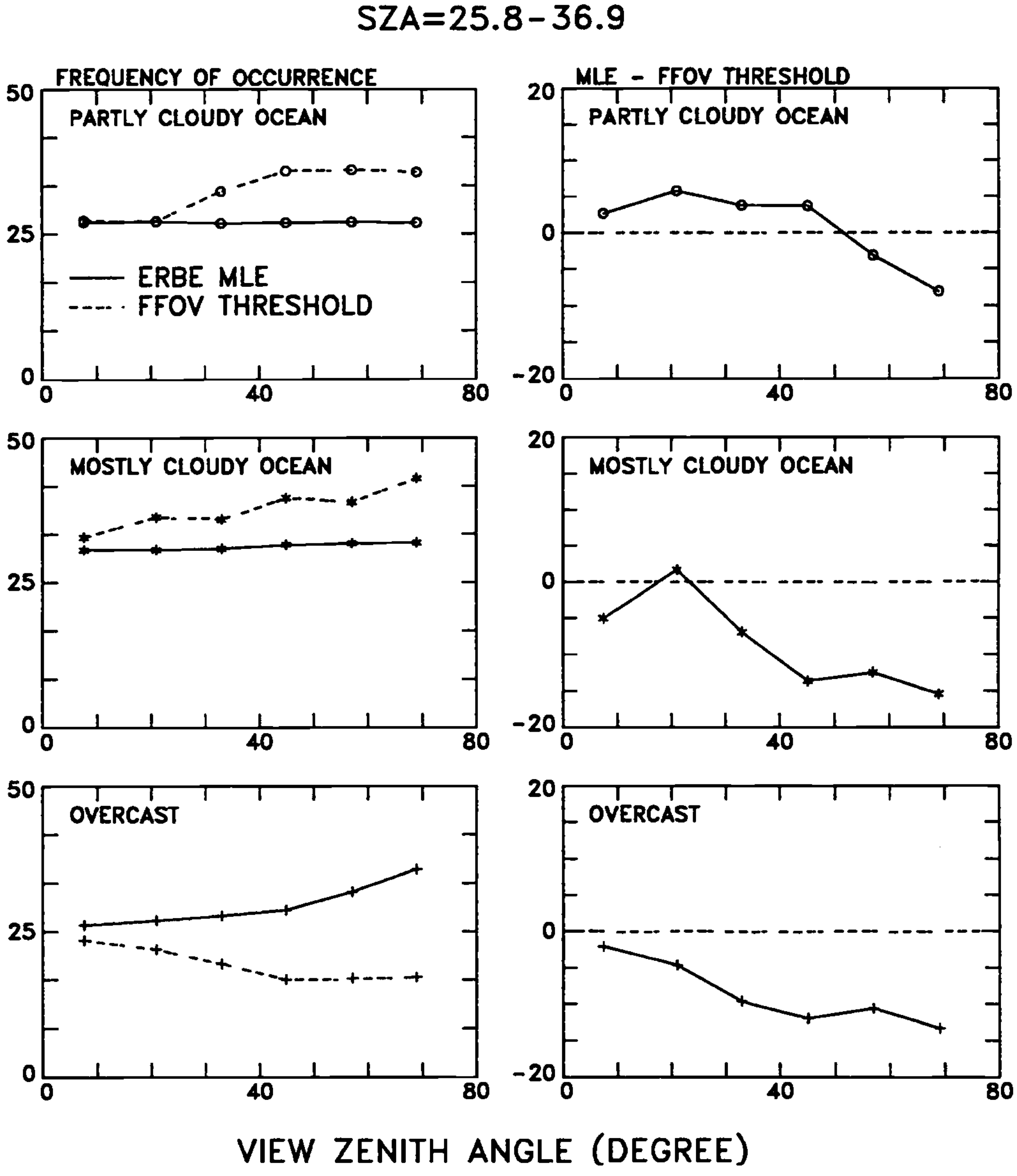

Figure 6.4 Frequencies of occurrence and mean reflected radiance differences between cloud scenes identified using the ERBE MLE and FFOV threshold methods. The diagrams in the left column are frequencies of occurrence expressed in percent. The diagrams in the right column are the percent differences in mean reflected fluxes obtained using the ERBE MLE and FFOV threshold methods (MLE — FFOV threshold). The results were calculated using ERBS scanner observations at solar zenith angles 25.8°— 36.9° for September, October, November, 1986.

7. SUMMARY AND CONCLUSIONS

Knowledge of the global radiation budget is needed to understand the present climate and future climate change. Scanning radiometers with high spatial resolution have been used to obtain the earth radiation budget. Scanning instruments measure radiances only at a particular angle for a given area of the earth at a given time. In order to convert the satellite scanning measurements to radiative fluxes, information on the angular distribution of the radiation is required.

In the Earth Radiation Budget Experiment (ERBE), there were two key steps in the process of allowing for the anisotropy of radiation. First, for each scanner field of view the scene type was identified using the ERBE maximum likelihood estimate (MLE) method which was specifically developed for cloud scene identification using Nimbus-7 ERB scanner observations. Then, an angular dependence model (ADM) for the particular scene type was applied. The ERBE ADMs were also constructed using the Nimbus-7 ERB scanning radiometer measurements.

The area covered by the field of view grows from nadir to limb for scanners. For example, the spatial resolution of the ERBE scanner was about 40 km at nadir but about 300 km at the limb. The ERBE MLE cloud scene identification method identified cloud scene types using shortwave and longwave radiance pairs observed for each field of view. Because of the large variation of cloud optical properties over relatively small spatial and temporal scales, scene identification using coarse spatial resolution bispectral radiance pairs was prone to error. Furthermore, shortwave and longwave radiance pairs follow nonlinear relationships which force area averages of the radiance pairs to follow relationships that differ from those obtained by averaging the relationships for the clear and overcast components that contribute to the scene. Consequently, the scene identification errors were a function of satellite zenith angle.

High resolution satellite observations show that about half the scenes at the 4 – 8 km scale contain broken clouds. The frequency of broken clouds is even greater for larger scales. Furthermore, uniform cloud layers and cloud-free regions cluster together so that the distribution of cloud cover depends on spatial scale. Near nadir, because of the relatively small field of view size, cloud-free scenes are frequently extracted from the midst of a broken cloud system and thus have a high probability of being cloud contaminated. By comparison, cloud-free scenes near the limb, where the field of view is relatively large, are likely to be extracted from vast regions that are also cloud-free and consequently subject to less cloud contamination. The complimentary situation occurs for overcast with clear sky contamination. As a result, the spatial scale dependence of cloud clustering and scene identification errors coupled with the growth of scanner field of view size from nadir to limb leads to a varying degree of cloud contamination from nadir to limb. Because the anisotropy of reflected and emitted radiation depends on the degree of cloud cover, this varying degree of cloud contamination affects the anisotropy of the observed radiances. For example, cloud-free regions with less cloud contamination should reflect and emit radiation that is more anisotropic than that which is contaminated.

If the scanner had a constant size field of view, then barring systematic scene identification errors, the degree of cloud contamination should be constant from nadir to limb. A sensitive test was conducted to examine the effect of instrument spatial resolution on the observed anisotropy. The test was made by comparing the anisotropy obtained from observations which had constant size fields of view with that obtained from observations with full spatial resolution (FFOV). The constant size field of view (CFOV) data were constructed from ERBS scanner observations by averaging observations for a certain number of neighboring pixels at nadir, the size of which matched the size of the field of view at the limb. Then, the cloud amount in the CFOV field of view was taken to be the weighted average of the amounts for the pixels used to form the simulated observations. The cloud scene type of the CFOV was determined by comparing the cloud amount with the conventional criteria used by ERBE, i.e., clear (0% – 5% cloud cover), partly cloudy (5% – 50% cloud cover), mostly cloudy (50% – 95% cloud cover), and overcast (95% – 100%). In this thesis, only observations which were either over oceans or identified as being overcast were used.

Angular dependence models were constructed for the CFOV and FFOV observations.

The statistical significance of differences between the FFOV and CFOV ADMs were obtained by dividing the observations into independent samples. Due to the nature of cloud spatial distributions, observed radiance fields are correlated on spatial scales of about 2000 km (or 40 scan lines for the case of ERBS). The Mean Square Successive Difference Test (MSSDT) was used to test the randomness of sample estimates that were taken to be independent. The results showed that constructing estimates for every set of 40 scan lines in the observations as Baldwin and Coakley (1991) suggested, the samples were still highly correlated. In this thesis, samples were obtained by averaging the ERBS scanner observations for every other set of 40 scan lines. Applying the MSSDT for these samples, the number of angular bins in which the neighboring observations were correlated at the 90% confidence level was significantly reduced.

Due to the idiosyncracies of the ERBS satellite orbit and the view zenith angle cutoff used here in the analysis, approximately 25% of the angular bins had no observations. A pseudo angular dependence model was used to deal with the effect of angular bins with no observations. In the pseudo ADM, mean radiances were simply set equal to zero for the angular bins in which there were insufficient observations. The minimum number of observations was eight in this thesis.

Comparisons between the FFOV and CFOV pseudo ADMs were made. A spatial-scale dependence was found in the observed anisotropy obtained using the ERBE MLE scene identification. The analysis showed

1. the percent differences between the FFOV and CFOV pseudo ADMs were as high as 10% for some viewing geometries for clear and partly cloudy ocean scenes. For mostly cloudy ocean and overcast scenes, the percent differences increased to about 5% for some angular bins. The differences for the longwave limb-darkening models were less than 1% for view zenith angles less than 60° but increased to about 2.5% for larger view zenith angles.
2. for the majority of angular bins (70%) there were significant differences between the FFOV and the CFOV pseudo ADMs at the 90% confidence level.

3. if the effect of cloud clustering was the major cause for the spatial-scale dependence, then for cloud-free scenes the CFOV observations would be more anisotropic than the FFOV observations. For overcast scenes, the CFOV observations were expected to be more isotropic. The results for clear sky scenes followed expectations. Those for overcast scenes, however, countered expectations.

The frequencies of occurrence for three ocean cloud cover and overcast scene types were calculated for both the FFOV and CFOV observations using the ERBE MLE scene identification. Because of the spatial dependence of the cloud cover distribution and because of the growth of the field of view size from nadir to limb, for the FFOV observations, the frequencies of occurrence for clear ocean and overcast scenes should have decreased and those for partly cloudy and mostly cloudy scenes should have increased. The frequencies of occurrence for clear scenes agreed with expectations. Constant frequencies of occurrence were obtained for partly and mostly cloudy scenes. The frequencies of occurrence increased with increasing view zenith angle for overcast scenes. The ERBE MLE cloud scene identification method clearly misidentified some of the scenes.

Clouds can extend vertically. Broken convective clouds have vertical dimensions which are comparable to their horizontal dimensions. Theoretical studies have shown that for cubes, biases in estimates of fractional cloud cover due to the effect of cloud sides increase with increasing view zenith angle when scanning radiometer measurements are used to measure cloud amount. The results obtained using ERBS observations for overcast scenes were consistent with theoretical predictions for cubic clouds.

A bispectral threshold scene identification method was developed for the purpose of reducing the spatial-scale dependence of scene identification errors. The ERBE MLE method was assumed to correctly identify scenes at nadir. ERBS nadir observations were averaged to simulate observations for fields of view at off nadir angles. The frequencies of occurrence that should have been observed at the off nadir angles for the three ocean and overcast scenes were obtained using these simulated observations.

Frequencies of occurrence decreased as expected for clear ocean and overcast scenes with increasing view zenith angle and increased for partly and mostly cloudy scenes. Bispectral thresholds were adjusted so that the populations of scene types as functions of view zenith angle equaled the simulated populations. Similar procedures were followed to develop bispectral observations for the CFOV observations. CFOV observations had a larger field of view at nadir than that for FFOV observations. Due to the effect of cloud clustering, as was expected, the frequencies of occurrence for clear and overcast scenes at nadir obtained with the CFOV thresholds applied to FFOV observations were less than those obtained using the FFOV thresholds. The CFOV fractional cloud cover obtained using the CFOV thresholds applied to CFOV observations was almost constant from nadir to limb.

The FFOV and CFOV ADMs were constructed based on the FFOV and CFOV threshold scene identification methods. Comparisons between the FFOV and CFOV ADMs showed

1. differences between the CFOV and FFOV threshold ADMs were significantly reduced compared with those obtained using the ERBE MLE ADMs. For the shortwave FFOV threshold ADMs, the differences were generally less than 0.5% for the three cloudy ocean and overcast scenes. For the longwave limb-darkening models, the differences almost vanished for view zenith angles less than 60° and were less than 2.5% for larger view zenith angles. Since the field of view sizes differed for the FFOV and CFOV observations, the ADMs derived using the FFOV threshold scene identification method showed less spatial-scale dependence than those obtained using the ERBE MLE scene identification method.
2. with correct scene identification, the CFOV observations which had large field of view size were expected to be more anisotropic/isotropic for clear/overcast scenes than were the FFOV observations. For the FFOV threshold method, the expected shifts were obtained.
3. compared with the results obtained using the FFOV thresholds, using the CFOV thresholds, the differences between the FFOV and CFOV threshold ADMs were

further reduced. Moreover, the number of angular bins which had significant differences were reduced by about a factor of 4 for clear scenes by replacing the FFOV thresholds with the CFOV thresholds. The number of angular bins were reduced about 3% for mostly cloudy and 6% for overcast scenes, but increased about 2% for partly cloudy scenes.

4. For the limb-darkening models, using the CFOV thresholds also gave better results. The number of angular bins which had significant differences was reduced about 2 – 3% for clear and mostly cloudy scenes and about 10% for partly cloudy and overcast scenes.

The FFOV and CFOV threshold-ADMs were evaluated to determine the degree to which they satisfied reciprocity and the degree to which they produced a global average spherical albedo that was independent of the satellite zenith angle used to obtain it. Compared with the ERBE ADMs,

1. the threshold-ADMs satisfied reciprocity more closely than did the ERBE ADMs.
2. the global average spherical albedos were estimated based on the ERBE inversion algorithm, the FFOV threshold scene identification with the FFOV ADMs, and the CFOV threshold scene identification with the CFOV ADMs. The estimates were based on three months of ERBS scanner observations. The results showed that the view zenith angle dependence of the global average albedo was significantly reduced by using the threshold scene identification methods and the threshold ADMs.
3. The global average spherical albedo increased 6% using the FFOV and CFOV threshold ADMs with the associated threshold scene identification methods compared with that derived by the ERBE inversion algorithm based on three months ERBS scanner observations. For ERBE MLE and ADMs, the estimated global albedo was 0.289 ± 0.005. It increased to 0.299 ± 0.005 for CFOV threshold algorithm and 0.296 ± 0.005 for FFOV threshold algorithm.

Because there were few or no observations for certain viewing geometries, the ADMs constructed here were normalized by taking the mean radiances to be zero for all bins for which observations were missing. These ADMs were called pseudo ADMs. The results obtained using the pseudo ADMs were compared with those obtained by using the mean radiances that were used to construct the ERBE ADMs to fill the angular bins with no observations. Differences between the global average albedo estimated using ADMs constructed with a full range of angular bins and those obtained using pseudo ADMs were small.

In summary, by comparing the anisotropy obtained from observations with a constant size field of view with that obtained from observations for which the field of view size increased from nadir to limb, the observed anisotropy was found to depend on spatial scale. This spatial scale dependence was linked to scene identification errors. The effect of cloud clustering coupled with the growth of field of view size from nadir to limb for scanning radiometers coupled with the scene identification errors were thought to be the primary causes for this spatial-scale dependence. A bispectral threshold scene identification method was developed to reduce the effect of cloud clustering. Using the threshold scene identification, the spatial-scale dependence for the ADMs developed in this thesis were significantly reduced. Moreover, compared with the ERBE ADMs, the threshold ADMs satisfied reciprocity more closely. Using the threshold scene identification methods and associated ADMs, the estimated global albedo based on the ERBS observations used in this thesis was evidently higher than that estimated using the ERBE algorithm. This increase suggested that the imbalance in the estimated net radiation budget found by ERBE (Barkstrom et al., 1989) may be significantly smaller.

This study began with the goal of testing the hypothesis that the effect of cloud clustering combined with increasing field of view size from nadir to limb and scene identification errors might lead to the spatial-scale dependence of the ADMs. The results obtained in the thesis were consistent with expectations. Unfortunately, only ERBS scanner observations over oceans were used in this investigation. Because of possible errors in the ERBE MLE scene identification, the magnitude of the effect of cloud clustering on the ADMs remains unknown. Using high resolution observations, like those from AVHRR, more accurate scene identification could be obtained and the effect of cloud clustering might be evaluated quantitatively.

It would appear that a logical next step in the development of ADMs would be to develop a complete set of ADMs for the twelve scene types based on the approach used in this thesis. The comparisons between the ERBE scanner/non-scanner at satellite altitude, suggested by Wielicki and Green (personal communication, 1993), could then be conducted to test the "goodness" of these ADMs. In the forthcoming CERES (Cloud and the Earth's Radiant Energy System) experiment, the scanning instruments will have higher spatial resolution and achieve better angular coverage. But, the effect of cloud clustering combined with increasing scanner field of view size with view zenith angle will remain and must be dealt with.

REFERENCES

Arking, A. and J. S. Levine, 1967: Earth albedo measurements: July 1963 to June 1964. *J. Atmos. Sci.*, **24**, 721–724.

Arking, A., 1964: The angular distribution of scattered solar radiation and the earth albedo as observed from TIROS. *Symposium on Atmospheric Radiation*, International Association of Meteorology and Atmospheric Physics (IUGG), Liningrad, USSR, August, 1964.

Ashburn, E. V. and R. G. Weldonn, 1956: Spectral diffuse reflectance of desert surfaces. *J. Opt. Soc. Amer.*, **8**, 583–586.

Baldwin, D. G. and Coakley, J. A., Jr., 1991: Consistency of Earth Radiation Budget Experiment bidirectional models and the observed anisotropy of reflected sunlight. *J. Geophys. Res.*, **96**, 5195–5207.

Barkstrom, B. R., E. Harrison, G. Smith, R. Green, J. Kibler, R. Cess and the ERBE Science Team, 1989: Earth Radiation Budget Experiment (ERBE) archival and April 1985 results. *Bull. Amer. Meteor. Soc.*, **70**, 1254–1262.

Barkstrom, B. R. and G. L. Smith, 1986: The earth radiation budget experiment: Science and implementation. *Rev. Geophys.*, **24**, 379–390.

Becker, F. P. Ramanantsizehena and M. Stoll, 1985: Angular variation of the bidirectional reflectance of bare soils in the thermal infrared band. *Appl. Opt.*, **24**, 365–375.

Bohren, C. and D. R. Huffman, 1983: Absorption and scattering of light by small particles. A Wiley-Interscience Publication, John Wiley & Sons, New York.

Brennan, B. and W, R. Bandeen, 1969: Anisotropic reflectance characteristics of natural earth surfaces. *Appl. Opt.*, **9**, 405–412.

Breon, F., 1992: Reflectance of broken cloud fields simulation and parameterization. *J. Atmos. Sci.*, **49**, 1221–1232.

Brownlee, K. A., 1965: Statistical theory and methodology in science and engineering. John Wiley & Sons, Inc., New York, 1965.

Cahalan, R. F., D. A. Short and G. R. North, 1982: Cloud fluctuation statistics. *Mon. Wea. Rev.*, **110**, 26–34.

Carlson, T. N., J. K. Dodd, S. G. Benjamin and J. M. Cooper, 1981: Satellite estimation of surface energy balance, moisture availability and thermal inertia. *J. Appl. Meteor.*, **20**, 67–87.

Cess, R. D., S. Nemesure, E. G. Dutton, J. J. Deluisi, G. L. Potter and J. Morcrette, 1992: The impact of clouds on the shortwave radiation budget of the surface-atmosphere system: interfacing measurements and models. *J. Climate*, **6**, 308–316.

Cess, R. D., B. P. Briegleb and M. S. Lian, 1982: Low-latitude cloudiness and climate feedback: Comparative estimates from satellite data. *J. Atmos. Sci.*, **39**, 53–59.

Chandraskehar, 1960: Radiative transfer. Dover Publisher, Inc., New York.

Chang, F. and J. A. Coakley, Jr., 1993: Estimating of errors in fractional cloud cover obtained with infrared threshold methods. *J. Geophys. Res.*, **98**, 8825–8840

Coakley, J. A., Jr., 1991: Reflectivities of uniform and broken layer clouds. *Tellus B*, **43**, 420–433.

Coakley, J. A., Jr. and T. Kobayashi, 1989: Broken cloud biases in albedo and surface insolation derived from satellite imagery data. *J. Climate*, **2**, 721–730.

Coakley, J. A., Jr. and R. Davies, 1986: The effect of cloud sides on reflected solar radiation as deduced from satellite observations. *J. Atmos. Sci.*, **43**, 1025–1035.

Coakley, J. A., Jr. and D. G. Baldwin, 1984: Towards the objective analysis of clouds from satellite imagery data. *J. Climate and Appl. Meteor.*, **23**, 1065–1099.

Coakley, J. A., Jr., R. D. Cess and F. B. Yurevich, 1983: The effect of tropospheric aerosols on the earth's radiation budget: a parameterization for climate models. *J. Atmos. Sci.*, **40**, 116–138.

Coulson, K. L., E. L. Gray and G. M. Bouricius, 1966: Optical reflection properties of natural surfaces. *ICARUS*, **5**, 139–148.

Coulson, K. L., 1956: Characteristics of solar radiation reflected from desert soil. *Technical report*, University of California, Los Angeles, Sci. Rept. 2 Contract

AF 19(604)-1303.

Cramer, H., 1946: Mathematical methods of statistics. Princeton University Press, Princeton.

Davies, R., 1988: Minutes of the twenty-fourth Earth Radiation Budget Experiment (ERBE) science team meeting held at NASA Langley research center, Hampton, VA. NASA Langley research center, February, 1988.

Davies, R., 1984: Reflected solar radiances from broken cloud scenes and the interpretation of scanner measurements. *J. Geophys. Rev.*, **89**, 1259–1266

Davies, R., 1978: The effect of finite geometry on the three-dimensional transfer of solar irradiance in clouds. *J. Atmos. Sci.*, **35**, 1712–1725.

Davis, J. M. and S. K. Cox, 1982: Reflected solar radiances from regional scale scenes. *J. Appli. Meteoro.*, **21**, 1698–1712.

Davis, J. M., S. K. Cox and T. B. McKee, 1979: Total shortwave radiative characteristics of absorbing finite clouds. *J. Atmos. Sci.*, **36**, 508–518.

Dlhopolshy, R. and R. D. Cess, 1993: Improved angular directional models for clear sky ocean derived from earth radiation budget satellite shortwave radiances. Institute for Terrestrial and Planetary Atmospheres, State University of New York, Stony Brook, New York.

Eaton, F. D. and I. Dirmhim, 1979: Reflected irradiance indicatrices of natural surfaces and their effect on albedo. *Appl. Opt.*, **18**, 994–1008.

Fitch, B. W., 1981: Effects of reflection by natural surfaces on the radiation emerging from the top of the earth's atmosphere. *J. Atmos. Sci.*, **38**, 2717–2729.

Fritz, S., P. K. Rao and M. Weinstein, 1964: Satellite measurements of reflected solar energy and the energy received at the ground. *J. Atmos. Sci.*, **21**, 141–151.

Gibson, G. G., F. M. Denn, D. F. Young, E. F. Harrison, P. Minnis, B. R. Barkstrom, O. C. Smith and D. J. Travers, 1990: Characteristics of the earth's radiation budget derived from the first year of data from the Earth Radiation Budget Experiment.

Long-term monitoring of the Earth's radiation budget, B. R. Barkstrom, Editor, Proc. SPIE, **1299**, 253–263

Green, R. N., J. T. Suttles and B. A. Wielicki, 1990: Angular dependence models for radiance to flux conversion. *Long-term monitoring of the Earth's radiation budget*, B. R. Barkstrom, Editor, Proc. SPIE, **1299**, 102–111.

Goody, R. M. and Y. L Yung, 1989: Atmospheric radiation: Theoretical basis. 2nd edition. Oxford University Press, New York.

Gupta, S. K., P. W. Heck, P. Minnis and E. F. Harrison, 1988: ERBE scene identification validation comparison with AVHRR/HBTM. Minutes of the twenty-fourth Earth Radiation Budget Experiment (ERBE) science team meeting held at NASA Langley research center, Hampton, VA. NASA Langley research center, August, 1988.

Hartman, D. L. and D. A. Short, 1980: Use of earth radiation budget statistics for studies of clouds and climate. *J. Atmos. Sci.*, **37**, 1233–1250.

Henderson-Sellers, A., N. A. Hughes and M. Wilson, 1981: Cloud cover archiving on a global scale: a discussion of principles. *Bull. Amer. Meteoro. Soc.*, **62**, 1300–1307.

House, F. B., G. E. Hunt, A. Gruber and A. T. Mecherikunnel, 1986: History of satellite missions and measurements of the earth radiation budget (1957–1985). *Rev. Geophys.*, **24**, 357–377.

Jacobowitz, H., R. J. Tighe and the Nimbus-7 ERB experiment team, 1984: The Earth radiation budget derived from the Nimbus-7 ERB experiment. *J. Geophys. Res.*, **89**, 4997–5010.

Kendall, M. G. and A. Stuart, 1961: The advanced theory of statistics. Vol. 2: Inference and relationship. Hafner Publisher Co. New York.

Kopia, L. P., 1986: Earth Radiation budget experiment scanner instrument. *Rev. Geophys.*, **24**, 400–406.

Kriebel, K. T., 1978: Measured spectral bidirectional reflection properties of four vegetated surfaces. *Appl. Opt.*, **17**, 253–258.

Kobayashi, T, 1993: Effects due to cloud geometry on biases in the albedo derived from radiance measurements. *J. Climate*, **6**, 120–128.

Lorenz, E. N., 1967: The nature and theory of the general circulation of the atmosphere. *Technical note*, **218**, World Meteorology Organization, Geneva.

Manalo et al., 1991: Validation of earth radiation budget experiment scanning radiometer data inversion procedures. Minutes of the twenty-eighth Earth Radiation Budget Experiment (ERBE) science team meeting held at University of California, San Diego, Scripps institution of oceanography, La Jolla, CA. NASA Langley research center, April, 1991.

McKee, T. B. and S. K. Cox, 1974: Scattering of visible radiation by finite clouds. *J. Atmos. Sci.*, **31**, 1885–1892.

Meerkoetter, R., 1990: Reflection functions for inhomogeneous land surfaces. *Appl. Opt.*, **29**, 4192–4198.

Naber, P. S. and J. A. Weinman, 1984: The angular distribution of infrared radiances emerging from broken fields of cumulus clouds. *J. Geophys. Res.*, **89**, 1249–1257.

Payette, F., 1989: Application of a sampling strategy for the ERBE scanner data. M.S. thesis, McGill University.

Pinty, B. and M. M. Verstraete, 1991: Extracting information on surface properties from bidirectional reflectance measurements. *J. Geophys. Res.*, **96**, 2865–2874.

Ramanathan, V., R. D. Cess, E. F. Harrison, P. Minnis, B. R. Barkstrom, E. Ahmad and D. Hartmann, 1989: Cloud-radiative forcing and climate: Results from the Earth Radiation Budget Experiment. *Sciences*, **243**, 918–930.

Ramanathan, V., 1981: The role of ocean-atmosphere interactions in the CO_2 climate problem. *J. Atmos. Sci.*, **38**, 57–63.

Raschke, E. and K. Y. Kondratyev, 1983: Radiation budget of the earth and its atmosphere. *Technical report*, WCP-40.

Raschke, E., T. H. Vonder Haar, W. R. Bandeen and M. Pasternak, 1973: The annual radiation balance of the earth-atmosphere system during 1969–1970 from Nimbus 3 measurements. *J. Atmos. Sci.*, **30**, 341–364.

Raschke, E. and W. R. Bandeen, 1970: The radiation balance of the planet earth from radiation measurements of the satellite Nimbus II. *J. Appl. Meteor.*, **9**, 215–237.

Reynolds, D. W., T. B. McKee and K. S. Danielson, 1978: Effects of cloud size and cloud particles on satellite-observed reflected brightness. *J. Atmos. Sci.*, **35**, 160–166.

Rossow, W. B., C. L. Brest and L. C. Garder, 1989: Global, seasonal surface variations from satellite radiance measurements. *J. Climate*, **2**, 214–246.

Ruff, I., R. Koffer, S. Fritz, J. S. Winston and P. K. Rao, 1968: Angular distribution of solar radiation reflected from clouds as determined from TIROS IV radiometer measurements. *J. Atmos. Sci.*, **25**, 323–332.

Smith, L. and N. Manalo, 1988: Along-track scanning results for limb-darkening functions and flux errors. Minutes of the twenty-third Earth Radiation Budget Experiment (ERBE) science team meeting held at NASA Langley research center, Hampton, VA. NASA Langley research center.

Smith, G., R. N. Green, E. Raschke, L. M. Avis, J. T. Suttles, B. A. Wielicki and R. Davies, 1986: Inversion methods for satellite studies of the earth's radiation budget development of algorithms for the ERBE mission. *Rev. Geophys.*, **24**, 407–421.

Staylor, W. F. and J. T. Suttles, 1986: Reflection and emission models for deserts derived from Nimbus-7 ERB scanner measurements. *J. Climate and Appl. Meteoro.*, **25**, 196–202.

Stephens, G. L., C. G. Campbell and T. H. Vonder Haar, 1981: Earth radiation budgets measurements from satellites and their interpretation for climate modeling and studies: *J. Geophys, Res.*, **86**, 9739–9760.

Stowe, L. L., C. G. Wellemeyer, T. F. Eck, H. Y. M. Yeh and Nimbus-7 Cloud Data Processing Team, 1988: Nimbus-7 global cloud climatology. Part I: Algorithm and validation. *J. Climate*, **1**, 445–470.

Stowe, L. L., H. Jacobowitz and V. R. Taylor, 1980: Reflectance characteristics of earth and cloud surfaces as measured by the ERB scanning channels on the Nimbus-7 satellite. *Proc. International Radiation Symposium*, Ft. Collins, CO.

Suttles, J. T., B. A. Wielicki and S. Vemury, 1992: Top-of-atmosphere radiative fluxes: validation of ERBE scanner inversion algorithm using Nimbus-7 ERB data. *J. Appl. Meteoro.*, **31**, 784–796.

Suttles, J. T., G. L. Smith, B. A. Wielicki, I. J. Walker, D. F. Young, V. R. Taylor and L. L. Stowe, 1989: Angular radiation models for the earth-atmosphere systerm. Vol. II: Longwave radiation. NASA Ref. Publ. RP-1184, pp 87.

Suttles, J. T., R. N. Green, P. Minnis, G. L. Smith, W. F. Staylor, B. A. Wielicki, I. J. Walker, D. F. Young, V. R. Taylor and L. L. Stowe, 1988: Angular radiation models for the earth-atmosphere systerm. Vol. I: Shortwave radiation. NASA Ref. Publ. RP-1184, pp 147.

Taylor, V. R. and L. L. Stowe, 1984: Reflectance characteristics of uniform earth and cloud surfaces derived from Nimbus-7 ERB. *J. Geophys. Res.*, **89**, 4987–4996.

Taylor, V. R., J. M. Vilardo, L. L. Stowe and S. K. Vemury, 1983: Nimbus—7 ERB emission models for ERBE processing. *AMS Fifth Conference on Atmospheric Radiation*, Baltimore, Maryland.

Vemury, S. K., 1987: Evaluation of the ERBE scene identification algorithm. *Technical report,* NASA contractor report 178243.

Vemury, S. K., L. Stowe and H. Jacobowitz, 1984: Sample size and scene identification (cloud): Effect on albedo. *J. Geophys. Res.*, **89**, 5345–5353

Welch, R. M. and B. A. Wielicki, 1986: Stratocumulus cloud field reflected fluxes: the effect of cloud shape. *J. Atmos. Sci.*, **41**, 3085–3104.

Wielicki, B. A. and L. Parker, 1992: On the determination of cloud cover from satellite sensors: the effect of sensor spatial resolution. *J. Geophys. Res.*, **97**, 12799–12823.

Wielicki, B. A. and R. N. Green, 1989: Cloud identification for ERBE radiative flux retrieval. *J. Appl. Meteoro.*, **28**, 1133–1146.